National Technical University of Athens
School of Mechanical Engineering
Fluids Department
Parallel CFD & Optimization Unit

Parameterization of Two-Element Airfoils, Implemented in Aerodynamic Shape Optimization

Diploma Thesis

Georgios Grigorios Klavdianos

Advisors:

Kyriakos C. Giannakoglou, Professor NTUA

Dr. V. Asouti, Adjunct Lecturer NTUA

Athens, 2025

Acknowledgements

Firstly, I would like to express my sincere gratitude to the supervisor of my diploma thesis, Professor Kyriakos C. Giannakoglou. His guidance, knowledge, expertise in the subjects I studied, and his support have been invaluable over the last years, not only for my thesis but also during his many undergraduate courses I attended.

Moreover, I am grateful for the insightful contributions, advice and assistance of Dr. Varvara Asouti, Adjunct Lecturer NTUA, who also oversaw the realization of my thesis. I extend my thanks to every member of the PCOpt/NTUA for their help. I would also like to thank all the professors of the School of Mechanical Engineering of the National Technical University of Athens for the valuable knowledge that they shared during my five years of study.

Finally, my deepest thanks and appreciation are extended to my family and partner for their unconditional love and support, and to my close circle of friends for the encouragement in their own way. I dedicate this thesis to them and to my late father and grandparents, who are forever by my side.

National Technical University of Athens
School of Mechanical Engineering
Fluids Department
Parallel CFD & Optimization Unit

Parameterization of Two-Element Airfoils, Implemented in Aerodynamic Shape Optimization

Diploma Thesis

Georgios Grigorios Klavdianos

Advisors:
Kyriakos C. Giannakoglou, Professor NTUA
Dr. V. Asouti, Adjunct Lecturer NTUA

Athens, 2025

Abstract

In aerospace engineering design problems, aerodynamic shape optimization (ShpO) proves invaluable, as it enhances performance metrics and achieves potential targeted distributions. This diploma thesis develops a systematic process of optimizing the geometry of an airfoil in two distinct configurations, a normal and a deployed flap one. Computational fluid dynamics (CFD) methods are utilized for the solution of the governing (flow) equations. The two-element airfoil geometry is implemented in ShpO cases that aim to improve its main aerodynamic performance metrics, namely the drag at cruise and the lift at takeoff. With the purpose of addressing the challenges of aerodynamic ShpO, such as the computationally demanding CFD simulations, the nonlinear fluid physics and the mesh sensitivities, two different optimization methods are applied, specifically Metamodel Assisted Evolutionary Algorithms (MAEAs) and the adjoint method.

An automatic process of generating the geometry of a two-element airfoil, in particular a main body and Fowler flap, is formulated. Using any airfoil's nodal coordinates as input, this process separates the airfoil into main body and flap, creates the flap's leading edge region and shapes the slot region of the main body so that it perfectly matches the flap. This is achieved by maintaining most of the airfoil nodes and designing Bézier curves, so that a realistic geometry with slope and curvature continuity is generated. The flap contour is then translated and rotated, as happens when

aircraft deploy their flaps. The airfoil is parameterized by the PARSEC method, so that its contour can be defined by a few parameters-design variables. Moreover, some of the parameters affecting the generated flap's contour and chord length serve as design variables.

The MAEA optimization method is applied in several test cases with varying sets of objectives, design variables, constraints and conditions. This method explores the design space very effectively, does not get trapped in local extrema (given a sufficient amount of evaluations) and does not depend on gradient information. However, even with the metamodel assisting the algorithm's search, it is an expensive method in this research field where many CFD simulations are required. Therefore, deterministic optimization, specifically adjoint-based, is also utilized. It greatly reduces the cost of the optimization since it demands two solver calls per optimization cycle and only a handful of cycles until convergence. Nonetheless, this method entails significant implementation effort, gradient information and may get stuck in local extrema or overshoot better solutions, especially in highly nonlinear problems.

Through the multiple test cases that are examined in this thesis, valuable conclusions are drawn about the behaviour of both stochastic and gradient-based methods in the aerodynamic ShpO of a two-element airfoil geometry. The ability of the proposed geometry creation and parameterization process to be included in an optimization loop is validated. Insights are obtained about the effect of the airfoil's shape and flap on its performance.

Εθνικό Μετσόβιο Πολυτεχνείο
Σχολή Μηχανολόγων Μηχανικών
Τομέας Ρευστών
Μονάδα Παράλληλης Υπολογιστικής Ρευστοδυναμικής
& Βελτιστοποίησης

Παραμετροποίηση Αεροτομών δύο Στοιχείων και Ένταξη στην Αεροδυναμική Βελτιστοποίηση Μορφής

Διπλωματική Εργασία

Γεώργιος Γρηγόριος Κλαυδιανός

Επιβλέποντες:
Κυριάκος Χ. Γιαννάκογλου, Καθηγητής ΕΜΠ
Δρ. Β. Ασούτη, Εντεταλμένη Διδάσκουσα ΕΜΠ

Αθήνα, 2025

Περίληψη

Σε προβλήματα σχεδιασμού στην αεροναυπηγική, η αεροδυναμική βελτιστοποίηση μορφής (ΒΜ) αποδεικνύεται πολύτιμη, καθώς βελτιώνει τους δείκτες απόδοσης και επιτυγχάνει ενδεχόμενες στοχευμένες κατανομές. Η διπλωματική εργασία αναπτύσσει μια συστηματική διαδικασία βελτιστοποίησης της γεωμετρίας μίας αεροτομής σε δύο διακριτές διαμορφώσεις, μία τυπική και μία με εκτεταμένη υπεραντωτική διάταξη στην ακμή εκφυγής (flap). Για την επίλυση των εξισώσεων που διέπουν τη ροή χρησιμοποιούνται μέθοδοι υπολογιστικής ρευστοδυναμικής (ΥΡΔ). Η γεωμετρία της αεροτομής δύο στοιχείων συμπεριλαμβάνεται σε εφαρμογές ΒΜ, οι οποίες στοχεύουν στη βελτίωση των βασικών αεροδυναμικών δεικτών απόδοσης της, συγκεκριμένα της αντίστασης κατά την οριζόντια πτήση και της άνωσης κατά την απογείωση. Προκειμένου να αντιμετωπιστούν οι προκλήσεις της αεροδυναμικής ΒΜ, όπως οι υπολογιστικά απαιτητικές προσομοιώσεις ΥΡΔ, η μη γραμμική φύση της ροής του αέρα και η ευαισθησία του πλέγματος στις μεταβολές, εφαρμόζονται δύο διαφορετικές μέθοδοι βελτιστοποίησης, συγκεκριμένα οι εξελικτικοί αλγόριθμοι υποβοηθούμενοι από μεταμοντέλα (ΜΑΕΑ) και η συνεχής συζυγής (continuous adjoint) μέθοδος.

Αναπτύχθηκε μία αυτοματοποιημένη διαδικασία δημιουργίας της γεωμετρίας αεροτομής δύο στοιχείων, και συγκεκριμένα του κυρίου σώματος (main body) και ενός flap τύπου Fowler. Χρησιμοποιώντας τις κομβικές συντεταγμένες οποιασδήποτε αεροτομής ως εί-

σοδο, η διαδικασία αυτή διαχωρίζει την αεροτομή σε κύριο σώμα και flap, δημιουργεί την περιοχή της ακμής πρόσπτωσης του flap και διαμορφώνει την περιοχή της σχισμής στο κύριο σώμα ώστε να εφάπτεται με το flap όταν αυτό δεν είναι εκτεταμένο. Αυτό επιτυγχάνεται διατηρώντας τους περισσότερους κόμβους της αεροτομής και σχεδιάζοντας καμπύλες Bézier, έτσι ώστε να προκύπτει μια ρεαλιστική γεωμετρία με συνέχεια στην κλίση και στην καμπυλότητα. Στη συνέχεια, το περίγραμμα του flap μετατοπίζεται και περιστρέφεται, όπως συμβαίνει όταν ένα αεροσκάφος αναπτύσσει τα flap. Η παραμετροποίηση της αεροτομής πραγματοποιείται με τη μέθοδο PARSEC, ώστε το περίγραμμα της να ορίζεται πλήρως από μερικές παραμέτρους-μεταβλητές σχεδιασμού. Επιπλέον, ορισμένες παράμετροι που επηρεάζουν τη μορφή και το μήκος χορδής του παραγόμενου flap χρησιμοποιούνται και αυτές ως μεταβλητές σχεδιασμού.

Η μέθοδος βελτιστοποίησης MAEA εφαρμόζεται σε δοκιμαστικές μελέτες με διαφορετικά σύνολα συναρτήσεων στόχου, μεταβλητών σχεδιασμού, περιορισμών και συνθηκών. Η μέθοδος αυτή εξερευνά αποτελεσματικά τον χώρο σχεδιασμού (design space), δεν παγιδεύεται σε τοπικά ακρότατα (εφόσον πραγματοποιηθεί επαρκής αριθμός αξιολογήσεων) και δεν εξαρτάται από παραγώγους. Ωστόσο, ακόμη και με την υποβοήθηση του μεταμοντέλου κατά την αναζήτηση, πρόκειται για μια υπολογιστικά απαιτητική μέθοδο στο ερευνητικό αυτό πεδίο όπου είναι αναγκαίες πολλές προσομοιώσεις ΥΡΔ. Για τον λόγο αυτό, χρησιμοποιείται επίσης και ντετερμινιστική βελτιστοποίηση υποστηριζόμενη από τη συζυγή μέθοδο. Η μέθοδος αυτή μειώνει σημαντικά το υπολογιστικό κόστος, καθώς απαιτεί μόνο δύο κλήσεις του επιλυτή ανά κύκλο βελτιστοποίησης και λίγους κύκλους έως τη σύγκλιση. Παρόλα αυτά, προϋποθέτει σημαντική προσπάθεια για να υλοποιηθεί, παραγώγιση του προβλήματος και ενδέχεται να παγιδευτεί σε τοπικά ακρότατα ή να "προσπεράσει" καλύτερες λύσεις, ιδίως σε εντόνως μη-γραμμικά προβλήματα.

Μέσα από τις πολλαπλές δοκιμαστικές μελέτες που εξετάζονται στην εργασία, εξάγονται πολύτιμα συμπεράσματα για τη συμπεριφορά τόσο των στοχαστικών όσο και των αιτιοκρατικών μεθόδων στη διαδικασία αεροδυναμικής ΒΜ της γεωμετρίας μιας αεροτομής δύο στοιχείων. Επιβεβαιώνεται η δυνατότητα ένταξης της προτεινόμενης διαδικασίας δημιουργίας και παραμετροποίησης της γεωμετρίας σε βρόχο βελτιστοποίησης. Αποκομίζονται, επίσης, σημαντικά πορίσματα για την επίδραση της μορφής της αεροτομής και του flap στην απόδοσή της.

Abbreviations

ABC	Adjoint Boundary Conditions
AoA	Angle of Attack
CFD	Computational Fluid Dynamics
CP	Control Point
EA	Evolutionary Algorithm
EASY	Evolutionary Algorithms SYstem
FAE	Field Adjoint Equations
GUI	Graphical User Interface
LE	Leading Edge
LU	Lower-Upper
MAEA	Metamodel Assisted EA
MOO	Multi-Objective Optimization
NTUA	National Technical University of Athens
OP	Operating Point
PARSEC	Parametric Airfoils for Rational Shape Expression and Construction
PCOpt	Parallel CFD & Optimization Unit
PS	Pressure Side
PUMA	Parallel Unstructured Adjoint Multi-row
ShpO	Shape Optimization
SOO	Single-Objective Optimization
SS	Suction Side
TE	Trailing Edge
w.r.t.	with respect to

Contents

Chapter 1

Introduction

1.1 Aerodynamic Shape Optimization

Aerodynamic shape optimization (ShpO) refers to the process of altering an aerodynamic body's geometry with the aim of improving aerodynamic performance metrics, such as lift, drag, or moment coefficients and pressure distribution. This is usually achieved by combining computational fluid dynamics (CFD) with optimization algorithms in order to calculate the most suitable solution for a specific problem. Through the optimization process, a problem which may implement a large number of design variables and predetermined objectives and constraints is solved with the purpose of finding a solution sufficiently better, aerodynamic metrics-wise, than the baseline. This field of research concerns a broad range of applications, which include aerospace, automotive, wind turbines, etc. [18, 23].

Technological advances in high-performance computing have aided aerodynamic ShpO, since CFD simulations are computationally demanding, often requiring a significant amount of time for completion even when utilizing parallelization on state-of-the-art processing units. Other challenges in this area of study include mesh sensitivity and nonlinear flow physics. The iterative change of the geometry in CFD-based optimization demands remeshing or deforming the mesh, which may lead to lower solution accuracy, inconsistent gradients, etc. Furthermore, the nonlinear nature of fluids (boundary layers, shock waves, etc.) poses a considerable challenge in aerodynamic ShpO, as small changes in the geometry can lead to disproportionately large or abrupt variations in aerodynamic performance. It introduces local optima and a generally challenging design space to study [21, 16].

1.1.1 Two-Element Airfoils

This diploma thesis examines the aerodynamic ShpO of an airfoil in both its normal configuration and a deployed flap one, where a flap is deployed in the trailing edge area of the airfoil. Aircraft deploy trailing edge flaps mainly during takeoff or landing as lift-enhancing devices. When flaps are deployed, the effective angle of attack of the wing increases, thus enhancing the lift at lower speeds. Conventional flaps can create excess drag, which may be desired to decrease speed during landing.

Out of several flap types, the most popular in real-life applications are the slotted flaps, as they increase the lift coefficient significantly more than other flap types. When these flaps are deployed, a gap, which is called a slot, forms between the main body and the flap. High pressure air from the pressure side of the airfoil flows through the slot to the suction side, delaying flow separation and enhancing the lift more efficiently.

The two-element airfoil geometry studied in this diploma thesis consists of an airfoil's main body and a Fowler flap. The Fowler flap is a variation of the slotted flap, with the difference being that the flap is deployed by combined translation and rotation, not just rotation. Consequently, the airfoil's area is increased, leading to higher lift enhancement. The Fowler flap usually shows a smaller increase in drag than normal slotted flaps [8].

1.1.2 Parameterization and Geometry Creation

With the aim of evaluating the aerodynamic performance of an airfoil in both of the aforementioned configurations with the use of CFD, a systematic process of parameterizing the airfoil boundary and generating the two-element geometry must be developed. For the parameterization of the airfoil, the chosen method should be effective in creating realistic airfoil contours with the implementation of a few parameters. Therefore, the PARSEC method is utilized, which is an explicit numerical method that uses 11 parameters to calculate the y coordinates of the nodes on each side of the airfoil as a polynomial function of the x coordinates [24, 19]. The airfoil geometry derived from the PARSEC method serves as the normal (or undeployed flap) configuration that is studied in this thesis' optimization cases.

Moreover, for the deployed flap configuration, the geometry of a two-element airfoil must be generated. An automated process that creates the required geometry using airfoil nodal coordinates (in this case computed by the PARSEC method) is developed. It separates the airfoil into main body and flap, creates the flap's leading edge region and shapes the slot region of the main body so that it perfectly matches the flap. This is done by retaining most of the airfoil nodes and connecting them appropriately with Bézier curves, while ensuring slope and curvature continuity. The generated flap contour is then translated and rotated, as happens during the de-

ployment of an aircraft's Fowler flap. The resulting geometry effectively models a two-element airfoil, namely an airfoil with a deployed TE flap, and constitutes the second configuration examined in this thesis.

1.1.3 Optimization Methodology

For the purpose of optimizing the shape of the airfoil geometries being examined, both stochastic and gradient-based methods are implemented. Specifically, Metamodel-Assisted Evolutionary Algorithms (MAEAs) and adjoint-based optimization are the two methods utilized in the cases of chapters 5 and 6. MAEAs and the adjoint method differ greatly in methodology, computational efficiency, and problems they're suitable for.

EAs are versatile, as they can even handle objective functions that are not differentiable, discontinuous, or include noise, with or without constraints. They excel at global exploration of the design space. Since they do not depend on gradient information and cannot be trapped in local extrema, they prove especially beneficial when the design space is complex or poorly understood. Conversely, they are computationally demanding, as they may require thousands of evaluations, and their convergence rate is usually slower than that of gradient-based methods. However, with the assistance of surrogate modelling, the computational cost is greatly reduced, since many expensive evaluations are approximated by the metamodel, enabling more efficient exploration of the design space. Thus, MAEAs prove to be a highly effective aerodynamic ShpO method, as they efficiently explore all possible solutions while meeting any constraints without requiring gradient information [20, 26].

Adjoint-based optimization, in contrast, is highly efficient for problems with a large number of design variables. When gradients can be computed analytically or semi-analytically via the adjoint method, the optimization demands a much lower computational cost per iteration, making it well-suited for fine-tuning designs in high-dimensional, continuous, and smooth design spaces. However, adjoint methods are sensitive to the initial design and may converge to local extrema. Additionally, they require significant implementation effort, including derivation and coding of the adjoint equations, which may not be feasible for every problem or codebase [9].

It is, therefore, very interesting to validate the ability of the proposed parameterization and geometry creation process to be implemented in aerodynamic ShpO problems, such as those studied in this diploma thesis, utilizing each of the aforementioned methods. Nowadays, it is common practice to combine stochastic with gradient-based optimization methods to leverage their respective strengths. A heuristic method is first applied to explore a possibly complex design space and find quality solutions, and then a deterministic method is implemented to refine and improve these solutions. Conversely, a gradient-based method could be utilized first to quickly converge towards a "good" solution, and if it is believed that the opti-

mization is trapped in a local extremum, a stochastic method could be applied to further explore the design space. Nevertheless, this thesis examines each of the two aforementioned optimization methods separately. The following test cases provide insights on the behaviour of the two optimization methods, since multiple different variations of design variables, objectives, conditions and constraints are applied.

1.2 Objectives and Layout

This diploma thesis is primarily focused on developing a systematic process of optimizing an airfoil geometry in both its initial and deployed flap configurations. The optimization cases studied aim to improve the main aerodynamic performance metrics of an airfoil, namely the drag coefficient at cruise and the lift coefficient at takeoff. Although the proposed process is tested in several cases concerning a specific airfoil, it can easily be applied to any airfoil geometry at hand. The systematic approach of parameterization, geometry creation, CFD implementation and, finally, optimization is described in this thesis' chapters, as explained below.

Firstly, in chapter 2 the process of creating a two-element airfoil geometry is explained. In order to implement the geometry creation process in an optimization loop, the input airfoil geometry must be parameterized in an explicit manner by a handful of design variables. The airfoil and flap parameterization methods are described in section 3.1.

As is stated before, CFD is utilized in combination with optimization methods, with the purpose of solving the problem's governing equations and calculating all the necessary aerodynamic metrics. Hence, meshes must be created around the geometries that are being examined, as described in section 3.2.

Chapter 4 elaborates on the optimization methods utilized for the cases studied in this thesis. Furthermore, regarding the adjoint method, the process of calculating the sensitivity derivatives for each problem's parameterization is presented in sections 4.3 and 4.4.

Finally, in chapters 5 and 6 the optimization cases for each method, respectively, are presented, the results are discussed and observations are made about the behaviour of the optimization process in each case. Chapter 7 concludes this diploma thesis and assesses the effectiveness of the proposed aerodynamic ShpO process and its findings.

Chapter 2

Generation of a Two-Element Airfoil

This chapter describes the process by which the geometry of a two-element airfoil (main body and flap) is created using the software developed during this diploma thesis. The software implements as input the nodal coordinates of the airfoil contour to be studied. In this case, the airfoil is derived from an application of the PCOpt/NTUA and can be seen in Figure 2.1.

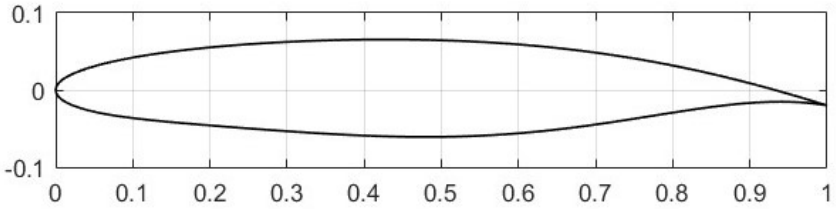

Figure 2.1: *Airfoil to be studied.*

The process of generating the desired geometry of a two-element airfoil can be summarized as follows:

1. The flap geometry is created by retaining some of the nodes of the initial airfoil near the trailing edge and using a Bézier curve for the leading edge region of the flap.
2. The airfoil's main body is generated using some of the remaining original nodes, certain points from the previously defined Bézier curve, and two additional Bézier curves to shape a trailing edge on the suction side and a fillet on the pressure side.

This process ensures that when the flap is not deployed, it perfectly matches the airfoil slot, as analyzed in the following sections. The resulting two-element airfoil geometry is displayed in figure 2.2.

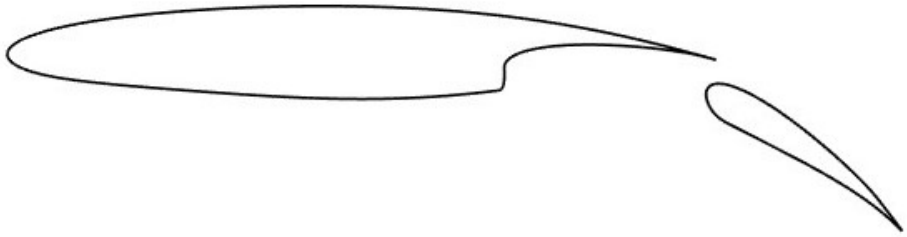

Figure 2.2: *Two-element airfoil geometry.*

2.1 Flap Geometry

The software begins by selecting the x coordinate of the points where the airfoil will be "cut" on the suction and pressure sides, respectively. This value, as the entire software, is nondimensionalized with respect to (w.r.t.) the airfoil chord and thus ranges from 0 to 1, while in practical cases, it typically falls within the range of 90-99% and 70-80% for the suction and pressure sides, respectively.

Afterwards, the nodes of the initial geometry closest to the selected x coordinate on each side of the airfoil are identified. These two nodes serve as endpoints for the Bézier curve that is constructed to define the leading-edge region of the flap, therefore ensuring that the resulting curve passes through them.

As mentioned earlier, the software additionally makes use of three Bézier curves. For this purpose, a process which takes the control point coordinates as input and generates a Bézier curve is implemented. In brief, a Bézier curve with known control point coordinates is described by the following equation [30]:

$$\vec{r}_0^N(t) = \sum_{i=0}^{N} \vec{r}_i B_i^N(t) \tag{2.1}$$

where $\vec{r}_0^N = (x, y)$ is the vector of the coordinates of each node of the Bézier curve, $\vec{r}_i = (\mathrm{x}_{CP,i}, \mathrm{y}_{CP,i})$ is the vector of the control point coordinates, t is a variable that ranges from 0 to 1, N+1 is the number of control points and B_i^N are the Bernstein polynomials which are calculated from the following expression:

$$B_i^N(t) = \frac{N!}{i!(N-i)!} t^i (1-t)^{N-i} \tag{2.2}$$

On the topic of designing the Bézier curve for the flap leading edge, so far the first and last control points' coordinates have been calculated (cut nodes). In total, 7 control points are used for the creation of this curve, the coordinates of which are calculated automatically as explained below. The resulting curve should be continuous in both slope and curvature with the airfoil boundary. For this reason, the first and second derivatives of the airfoil contour must be calculated at the two points where the airfoil is cut. This calculation is chosen to be performed using central finite differences, which are described by the following equations for non-uniformly spaced nodes using Taylor series expansion [25]:

$$\frac{dy}{dx} = \frac{y_{i-1} - y_{i+1}}{h_1 + h_2} \tag{2.3}$$

$$\frac{d^2y}{dx^2} = \frac{2}{h_1 + h_2}\left(\frac{h_2 y_{i-1} - (h_1 + h_2)y_i + h_1 y_{i+1}}{h_1 h_2}\right) \tag{2.4}$$

where i is the node that the airfoil is cut on the suction side. Similar expressions are applied for the pressure side. The h_1 and h_2 quantities are equal to:

$$h_1 = x_{i-1} - x_i \tag{2.5}$$

$$h_2 = x_i - x_{i+1} \tag{2.6}$$

Having calculated the first derivative at the cut point of each side of the airfoil, the second and sixth (second to last) control points are calculated as follows:

$$x_{CP,1} = x_{CP,0} - \varepsilon_1 \tag{2.7}$$

$$y_{CP,1} = \left.\frac{dy}{dx}\right|_{x=x_0} (x_{CP,1} - x_{CP,0}) + y_{CP,0} \tag{2.8}$$

$$x_{CP,N-1} = x_{CP,N} - \varepsilon_1 \tag{2.9}$$

$$y_{CP,N-1} = \left.\frac{dy}{dx}\right|_{x=x_N} (x_{CP,N-1} - x_{CP,N}) + y_{CP,N} \tag{2.10}$$

Therefore, the slope continuity between the generated Bézier curve and the original geometry is ensured, since the gradient of a Bézier curve at the start and end of it is equal to the gradient of the line connecting the first with the second and the last with the second to last control points, respectively. According to equations 2.7 and 2.9, the x coordinates of the second and second to last control points are calculated by subtracting $\varepsilon_1 = 0.03$ (chord percentage) from the x coordinate of the cutting point of the suction and pressure sides of the airfoil. The values of parameter ε_1 and of other similar parameters that are used in the developed software to compute

the control point coordinates described below, are not so important and affect the smoothness of the transition from the airfoil contour to the Bézier curve. These parameters are chosen in order to match the given two-element airfoil geometry from the PCOpt's application, as much as possible.

The third and fifth (third to last) control points are calculated for the resulting Bézier curve to have curvature continuity with the airfoil geometry. The curvature of a Bézier curve at the start and end points depends on the first three and last three control points respectively, and is calculated by [4]:

$$K_0 = \frac{(N-1)|(P_1 - P_0) \times (P_2 - 2P_1 + P_0)|}{N|P_1 - P_0|^3} \tag{2.11}$$

$$K_1 = \frac{(N-1)|(P_N - P_{N-1}) \times (P_N - 2P_{N-1} + P_{N-2})|}{N|P_N - P_{N-1}|^3} \tag{2.12}$$

where $K_{0,1}$ are the curvatures at the endpoints of the Bézier curve, N+1 the number of control points, $P_{0,1,2}$ the coordinate vector of the first, second and third control point and $P_{N,N-1,N-2}$ the equivalent for the last, second to last and third to last control point, respectively. After subtituting $P_{0,1,2}$ and $P_{N,N-1,N-2}$ with the x and y coordinates of each control point, expressions 2.11 and 2.12 take the following form:

$$K_0 = \frac{|x_0y_1 - x_1y_0 - x_0y_2 + x_2y_0 + x_1y_2 - x_2y_1|(N-1)}{N[(x_0 - x_1)^2 + (y_0 - y_1)^2]^{3/2}} \tag{2.13}$$

$$K_1 = \frac{|x_Ny_{N-1} - x_{N-1}y_N - x_Ny_{N-2} + x_{N-2}y_N + x_{N-1}y_{N-2} - x_{N-2}y_{N-1}|(N-1)}{N[(x_N - x_{N-1})^2 + (y_N - y_{N-1})^2]^{3/2}} \tag{2.14}$$

In equations 2.13 and 2.14 the x and y symbols denote control point coordinates which, in this thesis, are generally referred to as x_{CP} and y_{CP}. In order to ensure curvature continuity between the airfoil and the resulting Bézier curve, K_0 and K_1 need to be equal to the curvature of the airfoil at the cut points of the suction and pressure sides respectively. The first and last two control points have already been calculated, so the coordinates of only the third and fifth (third to last) control points are unknown, with regard to the control points that affect the curvature at the endpoints. The x coordinates of the aforementioned control points are calculated as follows:

$$x_{CP,2} = x_{CP,0} - \varepsilon_2 \tag{2.15}$$

$$x_{CP,N-2} = x_{CP,N} - \varepsilon_2 \tag{2.16}$$

where ε_2 is equal to 0.05. To calculate the y coordinates of the third and fifth control points, the curvature of the Bézier curve and the initial geometry are equated. The general formula for the curvature K of a curve is the following:

$$K = \frac{|\frac{d^2y}{dx^2}|}{\left(1 + (\frac{dy}{dx})^2\right)^{3/2}} \tag{2.17}$$

For the airfoil boundary, the first and second derivatives at the cut points are known from equations 2.3 and 2.4, so the curvature can be calculated at the endpoints of the Bézier curve. Thus, the y coordinates of the third and fifth control points are calculated by solving the following equations:

$$K_0\Big|_{y_2=y_{CP,2}} = K_{SS}\Big|_{x=x_0} \tag{2.18}$$

$$K_1\Big|_{y_{N-2}=y_{CP,N-2}} = K_{PS}\Big|_{x=x_N} \tag{2.19}$$

Lastly, there is an intermediate control point which is added to create an extra degree of freedom when shaping the resulting flap leading edge. The coordinates of the fourth control point are calculated as

$$x_{CP,3} = x_{CP,N-2} - \varepsilon_3 \tag{2.20}$$

$$y_{CP,3} = \frac{(y_{CP,2} + y_{CP,N-2})}{2} + \varepsilon_4 \tag{2.21}$$

According to equations 2.20 and 2.21, the y coordinate of the intermediate control point is set to the mean value of the third and fifth control point y coordinates with the summation of $\varepsilon_4 = 0.085$, while x is calculated by subtracting $\varepsilon_3 = 0.15$ from the fifth control point's x coordinate. The values of the ε parameters are determined as was previously explained. Once the coordinates of all the control points have been calculated, the Bézier curve for the flap leading edge is generated, using equation 2.1. The number of nodes for this curve is set to 50. Figure 2.3 illustrates the resulting Bézier curve for the flap and its control points having set x = 0.95 and x = 0.725 for the cut points of the suction and pressure sides of the airfoil respectively, in order to match the flap from the application. Overall, the flap contour comprises the nodes of the resulting Bézier curve and those of the initial geometry downstream of the cut points on each side of the airfoil. Figure 2.4 displays the generated flap geometry.

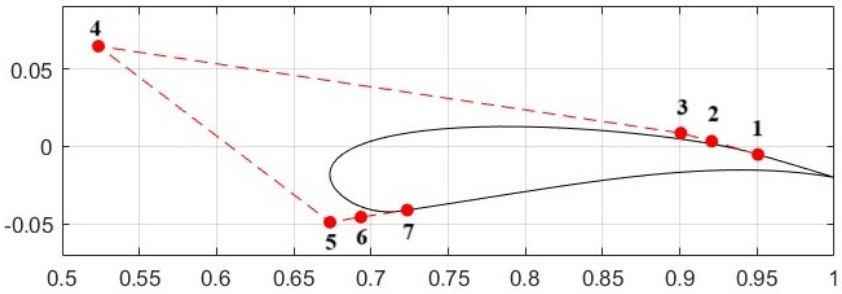

Figure 2.3: *Bézier curve for flap leading edge.*

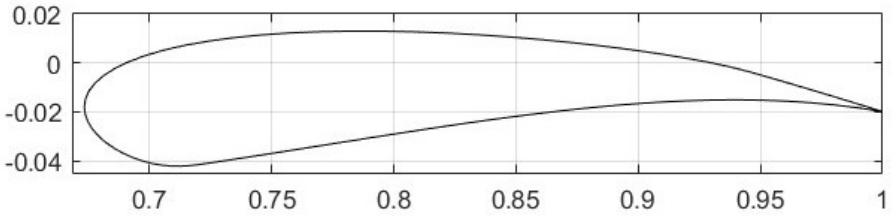

Figure 2.4: *Generated flap geometry.*

2.2 Slot Geometry

Having created the contour of the flap, the geometry of the so-called slot needs to be generated. The term slot is used to define the surface where the leading edge of the flap rests when it is not deployed [22]. One of the main goals during the development of the software that creates the two-element airfoil geometry was for the flap and the slot boundary curves to be tangent when the flap is undeployed, namely so that there is no gap in the wing during cruise. It is evident that this can only be achieved if some (in reality most) of the slot nodes are those computed for the Bézier curve of the flap leading edge. It would be ideal if the flap Bézier curve was used for the slot unaltered, however it is not possible because of the resulting corners (discontinuity) in the geometry if that were the case. For that reason, some of the flap's leading edge Bézier curve nodes are used (it is explained below how they are chosen) and they are connected to the suction and pressure sides of the remaining nodes of the initial airfoil (those that were not used for the flap) with two more Bézier curves. In this manner, the resulting main body geometry has slope and curvature continuity.

To begin with, the values of the minimum x coordinate of the previous Bézier curve $min(x_{flap})$ and the x coordinate of the first node of this Bézier curve $x_{flap}(1)$ which is the cutting point on the suction side, are calculated. Using these values, the x coordinates of the first control point of each of the two additional Bézier curves are

calculated as

$$x_{CP,0}^{SS} = x_{flap}(1) - \varepsilon_5 \tag{2.22}$$

$$x_{CP,0}^{PS} = \min(x_{\text{flap}}) - \varepsilon_6 \tag{2.23}$$

where $x_{CP,0}^{SS}$ refers to the x coordinate of the first control point of the new Bézier curve for the suction side of the airfoil and $x_{CP,0}^{PS}$ the equivalent for the pressure side. The chord percentages $\varepsilon_5 = 0.025$ and $\varepsilon_6 = 0.01$ that are subtracted in equations 2.22 and 2.23 are determined so that the two resulting Bézier curves don't have any intercepting points with the flap boundary (and for the other reasons that are explained in section 2.1). As in the flap geometry creation process, the nodes of the airfoil boundary closest to $x_{CP,0}^{SS}$ and $x_{CP,0}^{PS}$ are identified and chosen as the first control points for the two additional Bézier curves. Consequently, using formulas 2.3, 2.4 and 2.17 the first and second derivatives and the curvature of the airfoil boundary curve at the first control point are calculated, and with formulas 2.13 and 2.14 the curvature values of each Bézier curve at the endpoints are calculated as needed. Therefore, the coordinates of the second and third control points of each new Bézier curve are calculated, while ensuring slope and curvature continuity with the airfoil geometry. The coordinates are calculated by the following equations:

$$x_{CP,1}^{SS} = x_{CP,0}^{SS} + \varepsilon_7 \tag{2.24}$$

$$y_{CP,1}^{SS} = \left.\frac{dy}{dx}\right|_{x=x_{CP,0}^{SS}} (x_{CP,1}^{SS} - x_{CP,0}^{SS}) + y_{CP,0}^{SS} \tag{2.25}$$

$$x_{CP,2}^{SS} = x_{CP,0}^{SS} + \varepsilon_8 \tag{2.26}$$

$$K\Big|_{y_2=y_{CP,2}^{SS}} = K_{SS}\Big|_{x=x_{CP,0}^{SS}} \tag{2.27}$$

$$x_{CP,1}^{PS} = x_{CP,0}^{PS} + \varepsilon_9 \tag{2.28}$$

$$y_{CP,1}^{PS} = \left.\frac{dy}{dx}\right|_{x=x_{CP,0}^{PS}} (x_{CP,1}^{PS} - x_{CP,0}^{PS}) + y_{CP,0}^{PS} \tag{2.29}$$

$$x_{CP,2}^{PS} = x_{CP,0}^{PS} + \varepsilon_{10} \tag{2.30}$$

$$K\Big|_{y_2=y_{CP,2}^{PS}} = K_{PS}\Big|_{x=x_{CP,0}^{PS}} \tag{2.31}$$

where $\varepsilon_7 = 0.03$, $\varepsilon_8 = 0.045$, $\varepsilon_9 = 0.005$ and $\varepsilon_{10} = 0.01$. As was emphasized before, some of the flap Bézier nodes need to be implemented in the creation of the slot curve. To select these nodes, the node of the flap Bézier curve with the minimum value of x coordinate is identified and set as the final control point of the pressure

side Bézier curve, while the first node of the flap Bézier is the final control point of the suction side Bézier curve. By doing so, the slot boundary consists of the pressure side Bézier curve, the nodes of the flap Bézier until the node with $x = min(x_{flap})$ and the pressure side Bézier curve. This is carried out as follows:

$$x/y_{CP,5}^{SS} = x/y_{flap}(1) \tag{2.32}$$

$$x_{CP,5}^{PS} = min(x_{flap}) \tag{2.33}$$

where x/y_{flap} refers to the coordinate values of the flap Bézier curve nodes. In order to ensure that there is slope continuity between the flap Bézier curve and the two additional ones, the previous flap geometry node of the one with $y = y_{CP,5}^{SS}$ and the following node of the one with $x = x_{CP,5}^{PS}$ are chosen as second to last (fifth) control points of each new Bézier curve respectively. Hence, if i_{SS} is the first node of the flap boundary curve that is used for the slot boundary ($y = y_{CP,5}^{SS}$) and i_{PS} the last one ($x = x_{CP,5}^{PS}$), then the coordinates of the second to last control points of each additional Bézier curve are calculated as follows:

$$x_{CP,4}^{SS} = x_{flap,i_{SS}-1} \tag{2.34}$$

$$y_{CP,4}^{SS} = y_{flap,i_{SS}-1} \tag{2.35}$$

$$x_{CP,4}^{PS} = x_{flap,i_{PS}+1} \tag{2.36}$$

$$y_{CP,4}^{PS} = y_{flap,i_{PS}+1} \tag{2.37}$$

where x/y_{flap} denotes the coordinates of the flap boundary nodes. The control points of each of the additional Bézier curves are 6 (12 in total), because, as was applied for the flap, an intermediate control point is added for each curve. The coordinates of the intermediate (fourth) control point for each Bézier curve are calculated as follows:

$$x_{CP,3}^{SS} = x_{CP,4}^{SS} \tag{2.38}$$

$$y_{CP,3}^{SS} = \frac{y_{CP,2}^{SS} + y_{CP,4}^{SS}}{2} \tag{2.39}$$

$$x_{CP,3}^{PS} = \frac{x_{CP,2}^{PS} + x_{CP,4}^{PS}}{2} \tag{2.40}$$

$$y_{CP,3}^{PS} = \frac{y_{CP,2}^{PS} + y_{CP,4}^{PS}}{2} \tag{2.41}$$

The coordinates of all control points of the two Bézier curves that connect the selected nodes of the flap Bézier curve with the airfoil boundary are calculated as explained in the current section (2.2). In figure 2.5 the two additional Bézier

curves, their control points and the whole slot region of the main airfoil boundary are presented. The curve between the red and blue Bézier curves is the flap Bézier curve between the limits that were previously set. Figure 2.6 shows the main airfoil geometry without the flap and figure 2.7 is a detail of figure 2.6 showing the slot region.

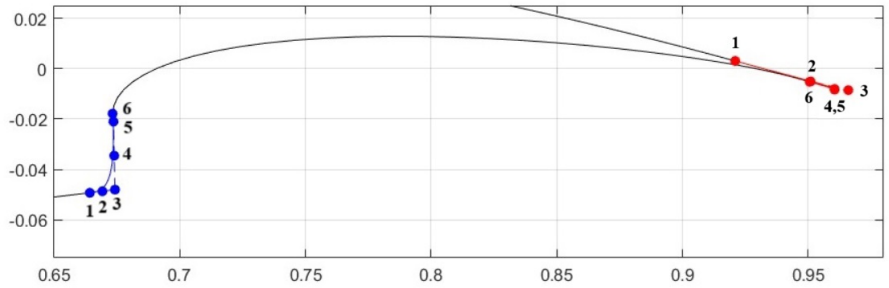

Figure 2.5: *Bézier curves for the slot geometry.*

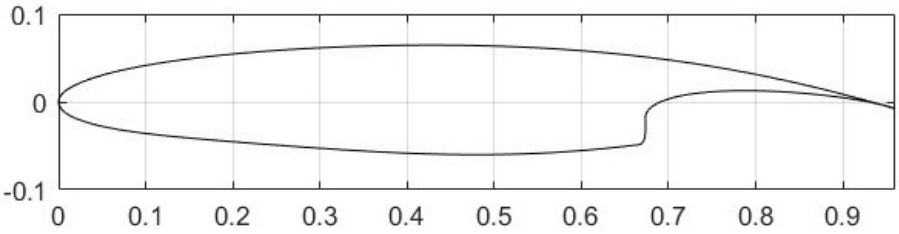

Figure 2.6: *Generated main body geometry.*

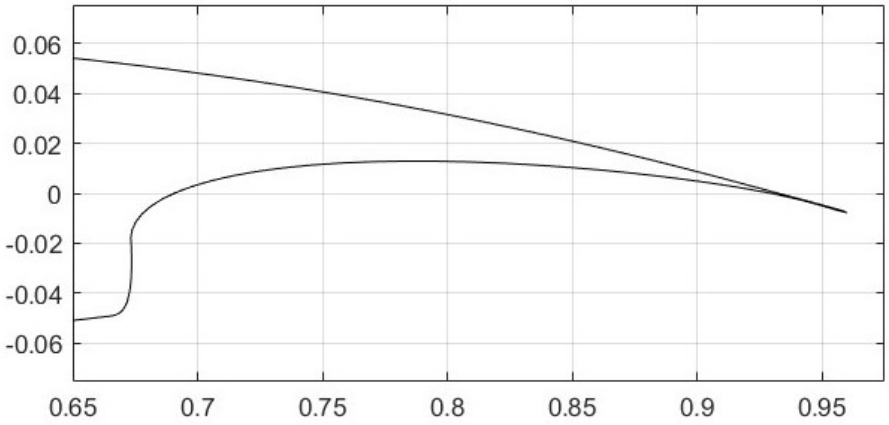

Figure 2.7: *Slot boundary.*

2.3 Two-Element Airfoil Geometry

As was previously stated, the way that the two-element airfoil geometry is created ensures that there are no intercepting points between the main body and flap boundaries when the flap isn't deployed. Figures 2.8 and 2.9 confirm that the flap can rest perfectly inside the slot, because the two boundaries coincide.

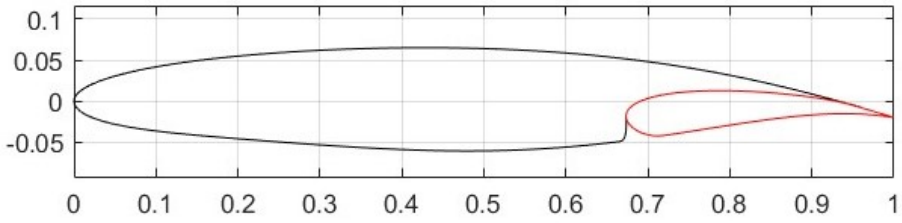

Figure 2.8: *Airfoil with flap not deployed.*

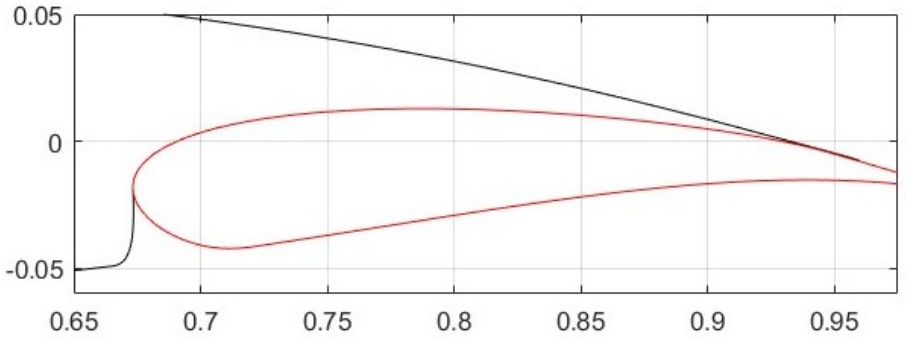

Figure 2.9: *Detail of figure 2.8 at the slot region.*

Two more figures are presented to make it clear that the software can create the necessary geometry at any position for the suction side cut point. Figure 2.10 shows the resulting geometry with the SS cut point set at x = 0.99 and figure 2.11 with x = 0.75.

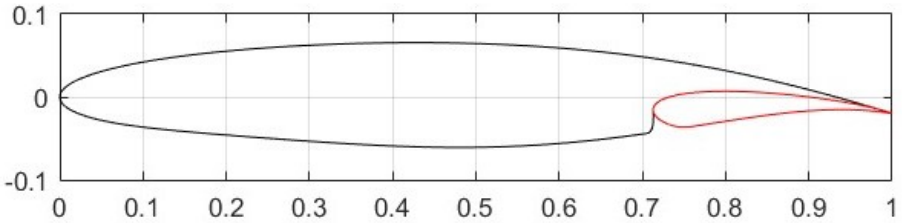

Figure 2.10: *Resulting geometry with the SS cut point at x = 0.99.*

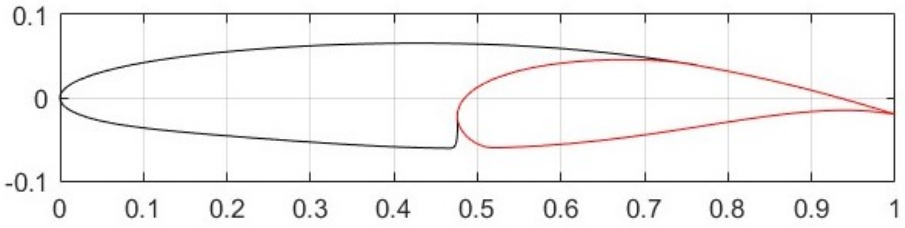

Figure 2.11: *Resulting geometry with the SS cut point at $x = 0.75$.*

Lastly, the developed software has the capability to change the chord length of the flap without changing the suction side cut point, but by altering the pressure side cut point. Figure 2.12 shows the resulting geometry with the flap chord length set at 20% of the airfoil chord and 2.13 shows the result for 60% flap chord length, while the suction side cut point is the same in both cases at x = 0.95.

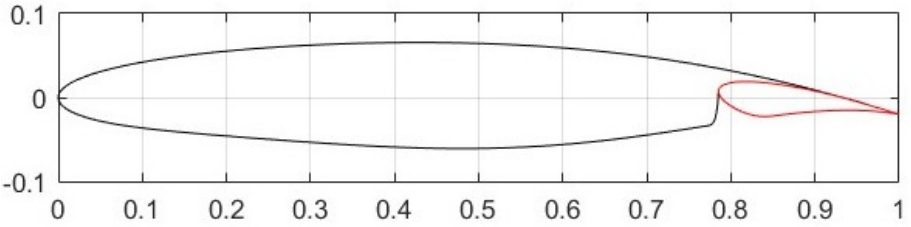

Figure 2.12: *Resulting geometry with the flap chord length 20% of the airfoil chord.*

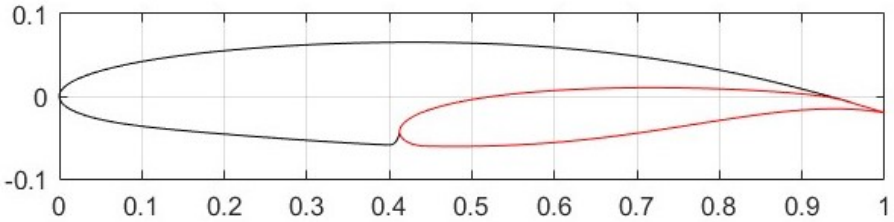

Figure 2.13: *Resulting geometry with the flap chord length 60% of the airfoil chord.*

2.4 Flap Deployment

Until this point two separate boundaries have been created for the main body of the airfoil and the flap. However, to completely define the two-element airfoil geometry, the flap boundary must be translated and rotated, as it happens when an aircraft deploys flaps during takeoff or landing. Thus, Δx and Δy are added to the x and y coordinates of the flap boundary nodes respectively, and then the coordinate vector is multiplied by a suitable rotation matrix. If X, Y are the flap coordinates and X',

Y' are the coordinates after the deployment, this is described as follows:

$$\begin{bmatrix} X' \\ Y' \end{bmatrix} = \begin{bmatrix} \cos\varphi & -\sin\varphi \\ \sin\varphi & \cos\varphi \end{bmatrix} \begin{bmatrix} X + \Delta x - x_0 \\ Y + \Delta y - y_0 \end{bmatrix} + \begin{bmatrix} x_0 \\ y_0 \end{bmatrix} \tag{2.42}$$

where φ is the angle of flap rotation and x_0, y_0 are the coordinates of the rotation axis. Figure 2.14 shows the generated geometry of the airfoil with the flap deployed at $\Delta x = 0.3, \Delta y = -0.02$ and $\varphi = -36°$ and the rotation axis being the cut point of the airfoil on the suction side.

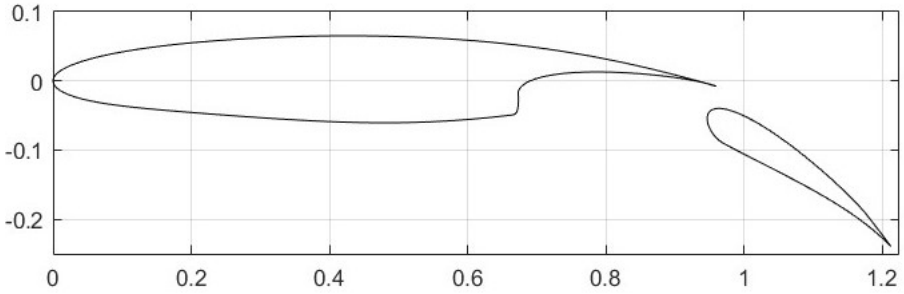

Figure 2.14: *Airfoil with deployed flap.*

Chapter 3

Airfoil Parameterization & Meshing

3.1 Parameterization

3.1.1 PARSEC Parameterization Method

In chapter 2 the process of creating the geometry of a two-element airfoil with a deployed flap is discussed. This process receives the coordinate vector of the airfoil in question as input. As the geometry creation process is intended to be used for shape optimization (ShpO) of the airfoil, there must be an explicit numerical method to update the airfoil boundary coordinates in every optimization cycle. Therefore, the airfoil must be parameterized by a method that uses a small number of parameters to define the airfoil boundary, but is also effective in controlling the important aerodynamic aspects and creates realistic airfoil shapes.

The parameterization method chosen is PARSEC (Parametric Airfoils for Rational Shape Expression and Construction), which implements 11 parameters of the airfoil boundary to completely define it [24, 19]. These parameters consist of: the leading edge radius (r_{LE}), the suction and pressure side crest locations ($x_{SS/PS}, y_{SS/PS}$) and curvatures ($y_{xxSS/PS}$), and the trailing edge location (y_{TE}), thickness (Δy_{TE}) , direction angle (a_{TE}) and wedge angle (β_{TE}). By definition, the leading edge of the airfoil is located at x = 0, y = 0 and the trailing edge at x = 1, y = y_{TE}. Figure 3.1 shows the 11 parameters of the PARSEC method and how they affect the airfoil shape.

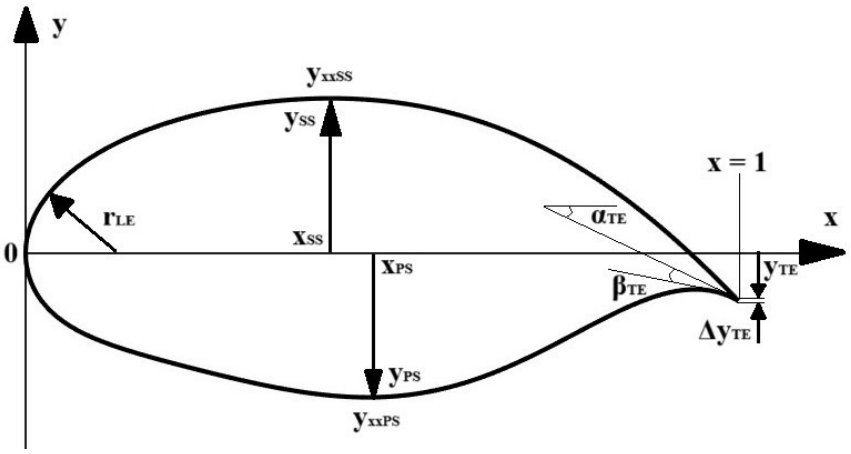

Figure 3.1: *PARSEC method for airfoil parameterization.*

Using the 11 parameters, the method defines a polynomial (one for each side of the airfoil) with 6 coefficients, in order to calculate the y coordinate of the airfoil contour at any given x. The PARSEC polynomial is given by

$$y = \sum_{n=1}^{6} a_n x^{n-1/2} \tag{3.1}$$

where a_n are the polynomial coefficients. The linear systems

$$\begin{bmatrix} 1 & 1 & 1 & 1 & 1 & 1 \\ {x_{SS}}^{0.5} & {x_{SS}}^{1.5} & {x_{SS}}^{2.5} & {x_{SS}}^{3.5} & {x_{SS}}^{4.5} & {x_{SS}}^{5.5} \\ 0.5 & 1.5 & 2.5 & 3.5 & 4.5 & 5.5 \\ 0.5{x_{SS}}^{-0.5} & 1.5{x_{SS}}^{0.5} & 2.5{x_{SS}}^{1.5} & 3.5{x_{SS}}^{2.5} & 4.5{x_{SS}}^{3.5} & 5.5{x_{SS}}^{4.5} \\ -0.25{x_{SS}}^{-1.5} & 0.75{x_{SS}}^{-0.5} & \frac{15}{4}{x_{SS}}^{0.5} & \frac{35}{4}{x_{SS}}^{1.5} & \frac{63}{4}{x_{SS}}^{2.5} & \frac{99}{4}{x_{SS}}^{3.5} \\ 1 & 0 & 0 & 0 & 0 & 0 \end{bmatrix} \begin{bmatrix} a_1^{SS} \\ a_2^{SS} \\ a_3^{SS} \\ a_4^{SS} \\ a_5^{SS} \\ a_6^{SS} \end{bmatrix} = \begin{bmatrix} y_{\mathrm{TE}} + 0.5\Delta y_{\mathrm{TE}} \\ y_{SS} \\ \tan\left(\frac{2\alpha_{\mathrm{TE}} - \beta_{\mathrm{TE}}}{2}\right) \\ 0 \\ y_{xx,SS} \\ \sqrt{2r_{\mathrm{LE}}} \end{bmatrix} \tag{3.2}$$

$$\begin{bmatrix} 1 & 1 & 1 & 1 & 1 & 1 \\ {x_{PS}}^{0.5} & {x_{PS}}^{1.5} & {x_{PS}}^{2.5} & {x_{PS}}^{3.5} & {x_{PS}}^{4.5} & {x_{PS}}^{5.5} \\ 0.5 & 1.5 & 2.5 & 3.5 & 4.5 & 5.5 \\ 0.5{x_{PS}}^{-0.5} & 1.5{x_{PS}}^{0.5} & 2.5{x_{PS}}^{1.5} & 3.5{x_{PS}}^{2.5} & 4.5{x_{PS}}^{3.5} & 5.5{x_{PS}}^{4.5} \\ -0.25{x_{PS}}^{-1.5} & 0.75{x_{PS}}^{-0.5} & \frac{15}{4}{x_{PS}}^{0.5} & \frac{35}{4}{x_{PS}}^{1.5} & \frac{63}{4}{x_{PS}}^{2.5} & \frac{99}{4}{x_{PS}}^{3.5} \\ 1 & 0 & 0 & 0 & 0 & 0 \end{bmatrix} \begin{bmatrix} a_1^{PS} \\ a_2^{PS} \\ a_3^{PS} \\ a_4^{PS} \\ a_5^{PS} \\ a_6^{PS} \end{bmatrix} = \begin{bmatrix} y_{\mathrm{TE}} - 0.5\Delta y_{\mathrm{TE}} \\ y_{PS} \\ \tan\left(\frac{2\alpha_{\mathrm{TE}} + \beta_{\mathrm{TE}}}{2}\right) \\ 0 \\ y_{xx,PS} \\ -\sqrt{2r_{\mathrm{LE}}} \end{bmatrix} \tag{3.3}$$

are solved using the 11 PARSEC parameter values to calculate the polynomial coefficients for the suction (α^{SS}) and pressure (α^{PS}) sides of the airfoil, respectively

[3]. Systems 3.2 and 3.3 are solved using LU factorization with partial pivoting whenever it is necessary to update the airfoil boundary, if the PARSEC parameter values have changed.

3.1.2 Flap Parameters

In this diploma thesis, the airfoil's aerodynamic performance is not only evaluated for the initial geometry, but also in the airfoil's deployed flap configuration, namely with main body and deployed flap boundaries. The two parameters with the highest importance during the flap's geometry creation process are the x coordinates of the cutting points on each side of the airfoil. As explained in section 2.1, the first and last control points of the flap's leading edge Bézier curve are referred to as the cutting points of the airfoil, because downstream of them the airfoil's original nodes are used for the trailing edge.

These two nodes' x coordinates are also incorporated in some of the following optimization cases as design variables. By doing so, the optimization process is given the ability to affect the flap's chord length and thus how effective it is in increasing the airfoil's lift. If $x_{suction,cut}$ and $x_{pressure,cut}$ denote the x coordinates of the cutting points on the suction and pressure sides of the airfoil, respectively, then the two flap design variables are

$$b_{flap,1} = x_{suction,cut} \tag{3.4}$$

$$b_{flap,2} = D = x_{suction,cut} - x_{pressure,cut} \tag{3.5}$$

3.2 Meshing

With the purpose of solving the flow with the use of CFD around the airfoil geometry, in both its initial and deployed flap configurations, an automatic process of mesh generation must be implemented. The mesh that is created is chosen to be a hybrid mesh, being structured near the airfoil or main body and flap boundaries and unstructured in the remaining computational space. This meshing method combines high solution accuracy and numerical stability, especially for boundary layer effects near the boundaries where gradients are high, with computational efficiency [1, 29]. Specifically, structured mesh layers are added on the mesh boundaries (excluding the farfield boundary) and then an unstructured mesh is generated around the layer region. Thus, there must be an automated way of calculating the boundary where the mesh switches from one type to the other.

In all the optimization cases studied herein, re-meshing was chosen, i.e. updating the mesh used for the CFD simulation in every cycle as the geometry changes. The re-meshing process, of course, needs to be applied automatically, hence, in every cycle a script must be written to create a mesh around the created geometry. As

explained in chapter 6, the geometric derivatives that are calculated make use of the chain rule to convert the derivative of the objective function w.r.t. the airfoil nodal coordinates to the derivative w.r.t. the design variables. Thus, the meshing process must "respect" the nodes of the contour; namely, the nodes on the boundary of the airfoil, main body and flap must not be altered, nor should there be any new ones added during meshing. Keeping the aforementioned in mind, meshing software "Gmsh" is chosen, mainly for the two reasons below:

- With certain commands, it can respect the nodes of the geometry around which it creates the mesh. No extra nodes on the boundary are added and the existing ones remain intact.
- The meshing process with "Gmsh" is easily added in an optimization loop, as every option in the GUI corresponds to commands that can be written in a script, to be executed in each cycle.

3.2.1 Layers' Creation

The process of generating the required two-element airfoil geometry that uses the PARSEC variables as input, as explained in chapter 2, also creates a listing of the boundary nodes, their connections and various other mesh settings. In order to create the structured layers around the boundary, line segments with a certain length perpendicular to the boundary are calculated for every node of the boundary, and new nodes are added on the other end of each segment. The length of the perpendicular line segments is equal to the total thickness of the structured mesh region, and logarithmic scaling is used to make the mesh denser near the boundary and less dense going outwards. The new nodes are calculated automatically as

$$\Delta x_i = x_{i+1} - x_{i-1} \tag{3.6}$$

$$\Delta y_i = y_{i+1} - y_{i-1} \tag{3.7}$$

$$\theta_i = atan2(\Delta y_i, \Delta x_i) \tag{3.8}$$

$$x_{perp,i} = x_i + \sin\theta_i \cdot d \tag{3.9}$$

$$y_{perp,i} = y_i - \cos\theta_i \cdot d \tag{3.10}$$

where x and y are the coordinates of the airfoil, main body or flap nodes and d is the total layers thickness. Moreover, an extra node is added downstream of the trailing edge, so as to create layers in the wake. The coordinates of the wake node are calculated as

$$slope_{TE} = \frac{y_5 - y_1}{x_5 - x_1} \tag{3.11}$$

$$x_{wake} = x_1 + \varepsilon \tag{3.12}$$

$$y_{wake} = y_1 + slope_{TE}(x_{wake} - x_1) \tag{3.13}$$

where $x_{1,5}$ and $y_{1,5}$ refer to the coordinates of the first and fifth nodes of the geometry that is being meshed, first node representing the trailing edge. Having calculated the wake node's coordinates, steps 3.6 through 3.10 are repeated twice for this node in order to add a line segment perpendicular to it in both directions (for the second direction the signs in equations 3.9 and 3.10 are switched). The interface where the mesh switches from structured-like to unstructured consists of the wake node and all the additional nodes that are calculated from the segments perpendicular to the boundary, connected one by one.

As optimization cases for the airfoil with the flap both deployed and undeployed are examined, the structured layer creation process is implemented three times for the airfoil, main body and flap, respectively. Figures 3.2, 3.3 and 3.4 show all the nodes that are calculated before meshing, both for the geometry and from the perpendicular to it line segments, and the boundary where the meshing method switches. Note that the long wake cells that are displayed in these figures are automatically split into smaller cells by the mesh generator with the use of suitable commands.

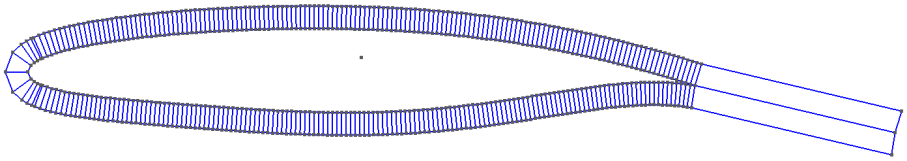

Figure 3.2: *Structured layers mesh region around airfoil.*

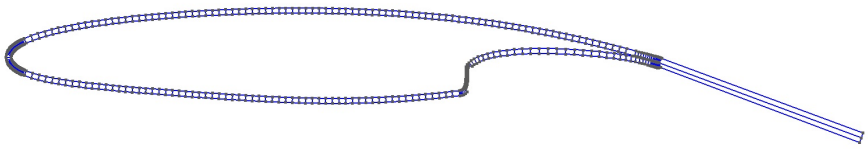

Figure 3.3: *Structured layers mesh region around airfoil's main body.*

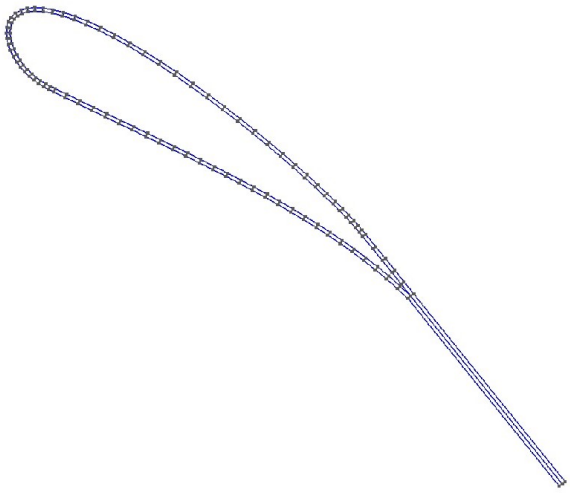

Figure 3.4: *Structured layers mesh region around flap.*

3.2.2 Resulting Meshes

As explained in section 3.2.1, a structured mesh is generated between the geometry's contour and the boundary calculated from the line segments perpendicular to it. At this point using the appropriate commands, it is ensured that the meshing does not affect the nodes of the geometry or add new ones. An ellipse is generated for the farfield boundary. Between the interface where the mesh type switches and the farfield boundary, an unstructured mesh is generated which, with the use of extra settings, becomes coarser towards the farfield boundary. The two resulting meshes for both cases are shown in figures 3.5 and 3.7, with some close-up views in figures 3.6 and 3.8.

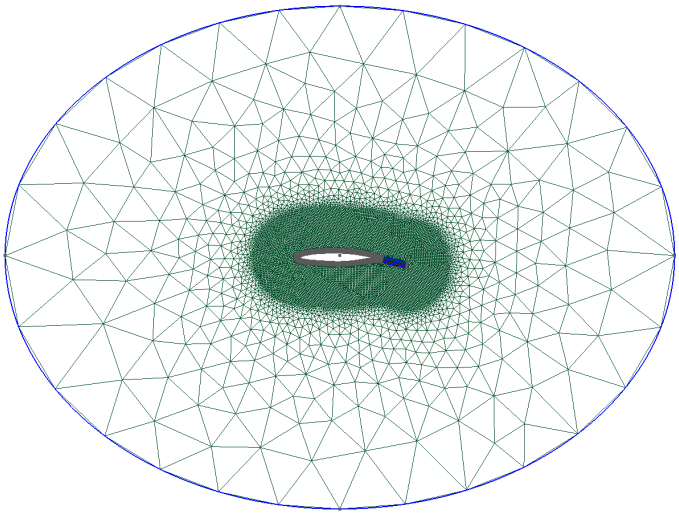

Figure 3.5: *Hybrid mesh around airfoil.*

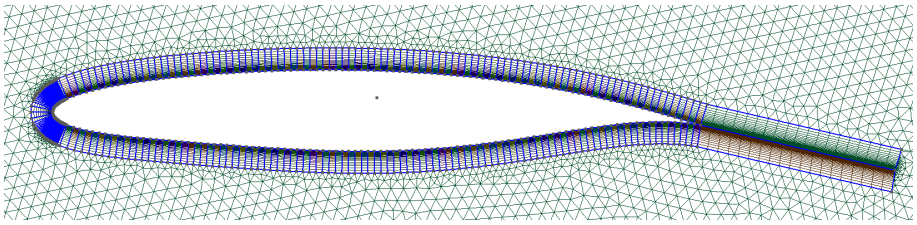

Figure 3.6: *Detail of figure 3.5.*

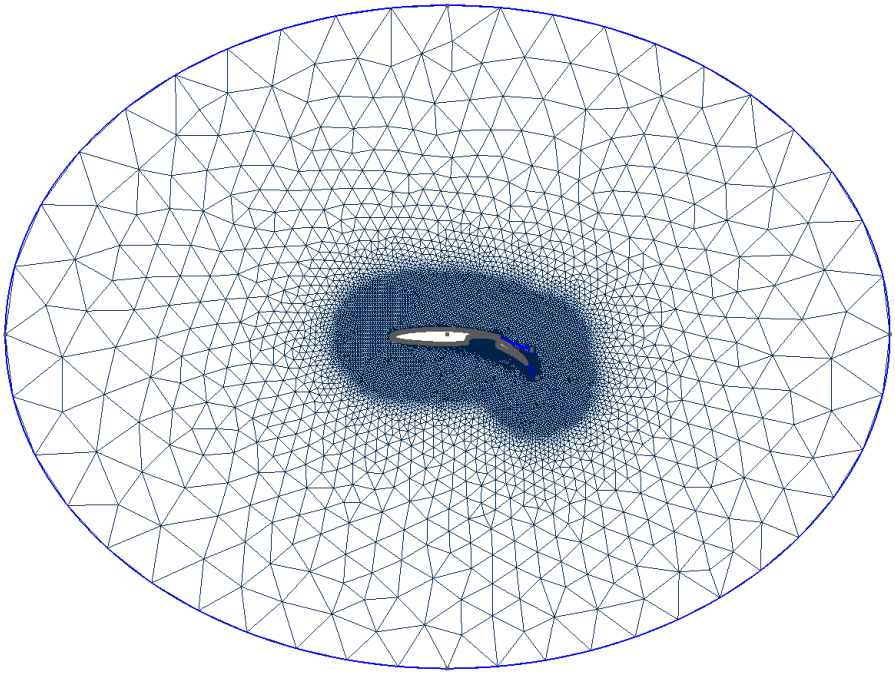

Figure 3.7: *Hybrid mesh around airfoil and deployed flap.*

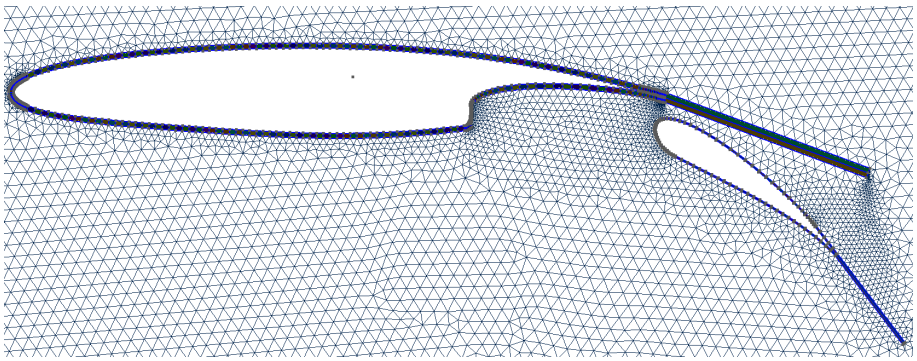

Figure 3.8: *Detail of figure 3.7.*

Chapter 4

Evolutionary and Gradient-based Optimization

4.1 Evolutionary Algorithms

This diploma thesis examines optimization cases with the use of both stochastic and deterministic methods. In chapter 5, the application of evolutionary algorithms is discussed, while in chapter 6 the adjoint (gradient-based) method is implemented. The PCOpt developed software EASY is utilized in all EA-based optimizations executed in the cases of chapter 5 [12, 11, 13].

EAs are a class of stochastic optimization methods inspired by the principles of natural selection and genetics. Their population-based structure allows them to efficiently explore complex, high dimension design spaces, making them particularly suitable for problems that are non linear, multi modal, or lack gradient information. Because EAs do not rely on derivatives, they can handle discontinuous or noisy objective functions, an important capability in many real world engineering contexts. Their mechanisms of selection, mutation, and crossover mimic natural evolutionary processes, promoting both exploration and exploitation of the design space [28, 2].

In ShpO, which is studied in this diploma thesis, EAs can prove invaluable, due to their ability to optimize objectives derived from expensive computational simulations, such as CFD. These simulations are often expensive and yield objective functions that are not analytically tractable, making gradient-based methods impractical. EAs can accommodate such black-box evaluations and are effective in aerodynamic applications, often finding "exotic" solutions in ShpO problems (if the parameterization allows it) [6, 17].

To address the high computational cost of CFD-based evaluations in ShpO, recent developments have focused on MAEAs. These incorporate surrogate models, namely mathematical approximations trained on a limited number of high fidelity simulations, to estimate objective functions. By using these models to guide the search, MAEAs can significantly reduce the number of expensive CFD evaluations required. Common surrogate techniques include kriging, radial basis functions, and polynomial regression, each offering a tradeoff between accuracy and computational efficiency. The optimization process alternates between exploring the design space using the surrogate and refining the model with new data points obtained from actual CFD runs. This balance allows MAEAs to retain the exploratory capabilities of evolutionary algorithms while improving efficiency, which is particularly beneficial in aerodynamic applications where simulation times are substantial [27].

Moreover, EAs are naturally suited to handling complex constraints by incorporating penalty functions, repair mechanisms, or constraint dominance principles into the selection process. This flexibility enables them to maintain feasible solutions throughout the optimization, even in the presence of highly nonlinear or discontinuous constraint boundaries [5]. In contrast, implementing constraints in adjoint-based optimization can be significantly more challenging, often requiring analytical derivation of adjoint equations for each constraint, which may not be practical or even feasible for complex engineering problems. Constraint handling is especially important for the following cases, since a number of constraints must be implemented. The most prominent one concerns the airfoil's area, as it must not differ more than slightly from the baseline value. Other constraints are imposed for the lift and moment coefficients at cruise.

4.1.1 Optimization using the EASY software

In the current subsection, the general process that the EASY software follows for the minimization of the objective function is described. EAs are population-based optimization methods, handling populations of possible solutions, or individuals, and the optimized solution is calculated through a process called evolution. In every generation (equivalent to an optimization cycle) of an EA, three discrete sets of individuals coexist. These sets are the parents with μ individuals, the offspring with λ and the elites, denoted with e.

At the start of every optimization cycle, the offspring of the current generation are evaluated. For an optimization case, such as those studied in this diploma thesis, the evaluation of the offspring corresponds to the solution of the flow for every individual (λ calls of PUMA), and naturally is the most costly part of the cycle. The elite archive is updated with offspring which are fitter than any of the current elites. The term fit refers to the objective function values of each individual that are calculated during the evaluation.

Afterwards, a random selection of elite individuals replaces some offspring (usually

the worst), in a process called elitism. As a result, it is ensured that the next generation always produces a solution at least as good as the one the previous generation had calculated. At this point, it is important to note that an elite archive is kept with the purpose of storing the best solutions, and utilizing elite genetic information for the offspring during elitism. A balance must be kept with elitism, as if too many elites are implemented in every generation, the exploration of the EA diminishes, as it exploits the already found elite individuals. This may cause the EA to get stuck at a local extremum for many generations.

The parents are chosen with an operator which usually uses both the parents and offspring of the previous generation. This operator is probability based and gives the best chances to individuals with the best relative objective function values. Lastly, the next generation's offspring are calculated from the parents through a series of operators, with the main ones being crossover and mutation. The crossover operator combines two parents to create two offspring with a high probability of its occurrence (around 90%). Conversely, the mutation operator aims to add new genetic information to the offspring, in many cases helping the EA out of a local extremum, but is typically applied with a very low probability (around 1%). In EAs with a high degree of elitism, elite individuals may also participate as parents to create offspring.

At the end of every generation, the convergence criterion of the optimization is applied, and if its requirements are not met, a new generation starts with the current offspring, as described in the current subsection. This whole process is easily utilized in MOO cases, as EAs can store all nondominated solutions in the elite archive (an individual is dominated if another one has better values for each objective function). Consequently, a front of non-dominated solutions can be created from the elites, containing the best solutions.

The EASY software developed by the PCOpt/NTUA, which makes extensive use of surrogate evaluation models or metamodels (trained on-line within the evolution), is utilized for the optimization. For each optimization run, a termination criterion of either 500 CFD evaluations for SOO cases or 1000 for MOO cases is set. A (μ,λ) = (20,40) MAEA is employed using real encoding of the design variables, with 95% crossover probability and 2% mutation probability, and an elite archive size of 15 for MOO cases. Metamodels (Radial Basis Function Networks) are activated once 70 evaluations respecting all constraints are archived in the database. Then, in each generation, 3 to 5 individuals are re-evaluated on the CFD tool.

4.2 Adjoint-Based Optimization

As is previously stated, in this diploma thesis, deterministic or gradient-based optimization methods are also implemented. The PCOpt's in-house flow solver PUMA is utilized in all following adjoint cases to solve both the primal and adjoint problems in every optimization cycle and compute the sensitivity derivatives of the objective function w.r.t. the geometry's nodes. These derivatives, after the transformations described in sections 4.3 and 4.4, are applied to update the design variables in every cycle with the aim of minimizing the objective function. The configurations in which the airfoil is examined are identical to the ones described in section 4.1, and the objectives of one or both are used in SOO or MOO runs, respectively.

The adjoint method is a powerful and cost-effective tool for engineering design in fluid dynamics. The greatest advantage of adjoint-based optimization is the ability to compute the gradients of an objective function w.r.t. a large number of design variables at a computational cost independent of the number of variables. Solving the adjoint problem produces the sensitivity information required for gradient-based optimization. Contrary to the finite difference methods that require separate evaluations for each design variable, adjoint-based optimization is particularly attractive for high-dimensional problems since it only requires one additional computation per objective or constraint function (per optimization cycle).

The adjoint method is, generally, formulated in two key stages: first, solving the primal problem that controls the physical behavior of the system, such as the Navier–Stokes equations for fluid flow, and second, solving the corresponding adjoint equations produced from the Lagrangian of the optimization problem. The adjoint variables that are computed from the solution of the adjoint equations are used to calculate the gradient of the objective function w.r.t. the design parameters. Essential for optimization algorithms like gradient descent or quasi-Newton methods employed in iterative design processes, this dual-solution technique allows very effective gradient computations [10, 9].

In CFD, adjoint is particularly well suited for aerodynamic ShpO, where performance metrics, such as drag, lift, or pressure coefficients, depend sensitively on the geometry of the domain. Because the number of geometric design variables can be extremely large when representing complex surfaces like airfoils, blades, or entire aircraft configurations, traditional sensitivity methods become computationally infeasible. The adjoint method overcomes this by providing gradient information w.r.t. all shape parameters in a single adjoint solve per objective or constraint. This efficiency makes high resolution ShpO not only feasible but also highly accurate, especially when using the discrete adjoint approach in conjunction with CFD solvers [7]. Furthermore, the method's compatibility with gradient-based optimization algorithms facilitates rapid convergence to optimal designs, and its extensibility to unsteady and multiphysics problems continues to expand its applicability in mod-

ern aerodynamic and turbomachinery design workflows [14].

Finally, a MOO problem with M objectives can be optimized using the adjoint method as a SOO problem. Each objective function is multiplied by a weight and the weighted sum constitutes the objective function

$$F_{SOO} = \sum_{i=1}^{M} w_i F_{MOO,i} \tag{4.1}$$

In this case, a front of non-dominated solutions cannot be computed by a single run as only one solution results per run, which is affected by the weight values. However, a front of non-dominated solutions can be computed by executing the optimization process for various weight values and storing the best solutions from each run.

4.2.1 The Continuous Adjoint Method

In this subsection, the general equations of the continuous adjoint optimization method are presented, by which the sensitivity derivatives of the objective function w.r.t. the design variables are calculated in each optimization cycle [15]. The method is examined in the context of aerodynamic ShpO with the use of CFD, as in this diploma thesis' optimization cases. If the primal or governing equations of the problem are denoted by $\vec{f}$ then the following expression applies:

$$\vec{f} = 0 \tag{4.2}$$

Therefore, the objective function F, which generally is an integral function, can be augmented as

$$F_{aug} = F + \int_{\Omega} \vec{\Psi}^T \vec{f} d\Omega \tag{4.3}$$

where $\vec{\Psi}^T$ refers to the adjoint variables and $d\Omega$ to the differential volume element. F_{aug} is differentiated w.r.t. the design variables as follows:

$$\delta F_{aug} = \delta F + \int_{\Omega} \vec{\Psi}^T \delta \vec{f} d\Omega \tag{4.4}$$

where δ represents the derivative w.r.t. the design variables $\vec{b}$. The derivatives of the adjoint variables and the volume element are equal to zero, as they are multiplied by the primal equations. Both the objective function and the primal equations may contain the flow variables $\vec{U}$ and the design variables. The terms of equation 4.4 which contain $\delta\vec{U}$ are grouped and set to zero. Of these terms, the integrands in the volume integrals form the field adjoint equations (FAE) from which the adjoint vari-

ables are calculated and the surface integrals form the adjoint boundary conditions (ABC). The remaining terms of equation 4.4 give derivatives only of the design variables (δb_n) and they are equal to the sensitivity derivatives of the objective function w.r.t. the design variables.

As is previously stated in section 4.2, the greatest benefit of the adjoint optimization method is that it only solves the primal and adjoint problems once per cycle. In the adjoint-based optimization cases studied in this thesis (chapter 6), the PCOpt/NTUA in-house CFD solver PUMA solves both problems in each optimization cycle, and calculates the sensitivity derivatives of each case's objective function w.r.t. the airfoil nodal coordinates. However, in order to compute the sensitivity derivatives w.r.t. the actual design variables, the output derivatives of the solver must be appropriately transformed. For each configuration that the airfoil is examined in, these transformations are described in sections 4.3 and 4.4, respectively.

4.3 Cruise Geometric Derivatives

The cruise configuration of the airfoil that is examined in the current diploma thesis involves the airfoil with the flap undeployed, as is discussed also in section 4.1. This configuration simulates the operation of the wing at cruise conditions. Using the PCOpt/NTUA in-house CFD solver PUMA, adjoint-based ShpO can be applied for this case. The solver in every optimization cycle solves the primal and adjoint problems, as described in subsection 4.2.1, and computes the partial derivative of the objective function w.r.t. the coordinates of the geometry's nodes $\partial F/\partial X$, where F represents the objective function and $X = \{\vec{x}, \vec{y}\}$ the matrix containing the coordinates of the airfoil's nodes. However, in order to update the values of the design variables, the total derivatives of F w.r.t. the design variables, or sensitivity derivatives $dF/d\vec{b}$ need to be computed, where $\vec{b}$ is the vector containing the design variables. Thus, the following chain rule is used to transform $\partial F/\partial X$ into $dF/d\vec{b}$

$$\frac{dF}{d\vec{b}} = \frac{\partial F}{\partial X}\frac{dX}{d\vec{b}} \tag{4.5}$$

Considering that matrix X consists of the x and y coordinates of the airfoil's nodes, expression 4.5 is written as follows:

$$\frac{dF}{d\vec{b}} = \frac{\partial F}{\partial \vec{x}}\frac{d\vec{x}}{d\vec{b}} + \frac{\partial F}{\partial \vec{y}}\frac{d\vec{y}}{d\vec{b}} \tag{4.6}$$

In every optimization cycle, $\partial F/\partial \vec{x}$ and $\partial F/\partial \vec{y}$ are written in the output file of PUMA. The geometric derivatives of the nodes of the airfoil w.r.t. the design variables $d\vec{x}/d\vec{b}$ and $d\vec{y}/d\vec{b}$ must be calculated in every cycle. For this configuration

of the airfoil, the design variables consist of the PARSEC parameters (subsection 3.1.1), as the flap is not deployed. Therefore, the derivatives of the coordinates of the resulting airfoil w.r.t. the PARSEC parameters are to be computed. The computation is done analytically. As can be observed from equation 3.1, the x coordinate of each airfoil node is handled as input when using the PARSEC method, and only the y coordinate is calculated using the parameters. That being the case, $d\vec{x}/d\vec{b}$ is equal to zero and $d\vec{y}/d\vec{b}$ is computed as:

$$\frac{d\vec{y}}{d\vec{b}} = \sum_{n=1}^{6} \frac{da_n}{d\vec{b}} x^{n-1/2} \tag{4.7}$$

The term $da_n/d\vec{b}$ is a 6x11 matrix containing the derivatives of each PARSEC polynomial coefficient w.r.t. each design variable. As explained in section 3.1.1, two sets of polynomial coefficients are calculated ${a_n}^{SS}$ and ${a_n}^{PS}$, one for each side of the airfoil. Each one has the below dependencies to the design variables, as can be observed from the linear systems 3.2 and 3.3:

$${a_n}^{SS} = {a_n}^{SS}(b_1, b_2, b_3, b_4, b_5, b_6, b_7, b_8) \tag{4.8}$$

$${a_n}^{PS} = {a_n}^{PS}(b_1, b_2, b_3, b_4, b_5, b_9, b_{10}, b_{11}) \tag{4.9}$$

By solving the 3.2 and 3.3 linear systems, analytical expressions for the two sets of polynomial coefficients can be derived. These expressions are then differentiated w.r.t. each design variable to derive analytical expressions for each element of the $d{a_n}^{SS}/d\vec{b}$ and $d{a_n}^{PS}/d\vec{b}$ matrices. These two matrices are calculated in every optimization cycle from the aforementioned analytical expressions as the design variables update, and then are implemented in equation 4.7 to calculate $d\vec{y}/d\vec{b}$.

Having calculated $d\vec{x}/d\vec{b}$ and $d\vec{y}/d\vec{b}$, and knowing the values of $\partial F/\partial\vec{x}$ and $\partial F/\partial\vec{y}$ from the adjoint solver, the chain rule from equation 4.6 can be applied to calculate $dF/d\vec{b}$. In order to update the design variables in every optimization cycle, the steepest descent method is used, which is described below:

$$\vec{b}^{k+1} = \vec{b}^{k} - \eta \frac{dF}{d\vec{b}}\bigg|_k \tag{4.10}$$

where η is the step size of the method and k is the optimization cycle counter. Applying expression 4.10 with the sensitivity derivatives calculated from expressions 4.6 and 4.7, the design variables of the cruise configuration are updated in every cycle and the problem is being optimized with the adjoint-based method.

4.4 Takeoff Geometric Derivatives

This diploma thesis studies also the deployed flap configuration of the airfoil in the following optimization cases. It simulates the conditions of the aircraft during takeoff, where flaps are deployed as lift-enhancing devices. In this case, the primal and adjoint equations are solved by PUMA around the geometry of the two-element airfoil which is created from the initial airfoil as described in chapter 2. Therefore, if $X'' = \{\vec{x''}, \vec{y''}\}$ is the matrix containing the coordinates of the main body's and flap's nodes, with the flap deployed, and F again is the objective function, then the adjoint method computes the partial derivatives $\partial F/\partial X''$ in every optimization cycle. This configuration involves not only the 11 PARSEC parameters as design variables, but also the 2 flap parameters discussed in subsection 3.1.2. If $X' = \{\vec{x'}, \vec{y'}\}$ denotes the coordinates of the main body's and flap's nodes pre-deployment, $X = \{\vec{x}, \vec{y}\}$ the nodes of the initial one-element airfoil, $\vec{b}_{par}$ the PARSEC design variables and $\vec{b}_{flap}$ the flap design variables, then the sensitivity derivatives $dF/d\vec{b}$ are calculated by the chain rule as follows:

$$\frac{dF}{d\vec{b}_{par}} = \frac{\partial F}{\partial X''}\frac{\partial X''}{\partial X'}\frac{\partial X'}{\partial X}\frac{dX}{d\vec{b}_{par}} \tag{4.11}$$

$$\frac{dF}{d\vec{b}_{flap}} = \frac{\partial F}{\partial X''}\frac{\partial X''}{\partial X'}\frac{dX'}{d\vec{b}_{flap}} \tag{4.12}$$

$$\frac{dF}{d\vec{b}} = \left\{ \begin{array}{c} \frac{dF}{d\vec{b}_{par}} \\ \frac{dF}{d\vec{b}_{flap}} \end{array} \right\} \tag{4.13}$$

In equation 4.11 the derivative $dX/d\vec{b}_{par}$ is exactly the same as dX/db that is calculated in section 4.3. Thus, three additional derivative matrices ($\partial X''/\partial X'$, $\partial X'/\partial X$ and $\partial X'/\partial\vec{b}_{flap}$) must be calculated to apply the chain rule for the takeoff configuration. In subsection 4.4.1 the necessary calculations in order to apply the chain rule of equation 4.11 are described, while in subsection 4.4.2 the computation of the derivatives of equation 4.12 is explained.

4.4.1 Sensitivity Derivatives w.r.t. PARSEC Design Variables

Firstly, the K'xK matrix containing the partial derivative $\partial X'/\partial X$ must be calculated, which represents the derivative of every node's of the main body and flap coordinates w.r.t. every node's of the original airfoil coordinates. This matrix is not square, since, as discussed in chapter 2, most of the nodes of the initial airfoil with the addition of the Bézier curve nodes are utilized in creating the main body and flap. Consequently, the main body's and flap's nodes are more than the initial airfoil's, indicating that K' > K. To make the calculation of the aforementioned matrix clearer, the airfoil, main body and flap nodes are divided into 8 sections, as in figures 4.1 and 4.2.

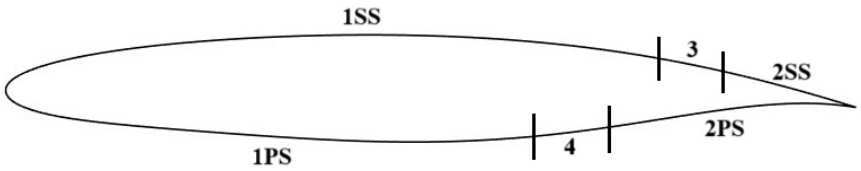

Figure 4.1: *Airfoil node sections.*

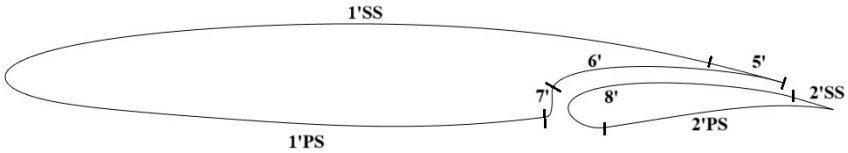

Figure 4.2: *Main body and flap node sections. Note that the flap is slightly translated to the right and downwards, with the aim to make the node sections easier to identify.*

In figure 4.1 sections 3 and 4 refer to the nodes that are not utilized in the main body or flap of the two-element airfoil configuration. The remaining nodes of the initial airfoil, sections 1SS, 1PS, 2SS and 2PS, appear unaltered in the main body and flap, hence 1'≡1 and 2'≡2. Section 8' denotes the Bézier curve that is created for the flap's leading edge (section 2.1), while 6' contains a selection of section 8' nodes as explained in section 2.2. Sections 5' and 7' represent the two additional Bézier curves that are created to merge 6' with 1'. Furthermore, attention is drawn to the fact that the software which generates the geometry writes the airfoil, main body and flap's nodes in the following order: from the TE to the LE through the suction side and back to the TE through the pressure side (important for the order of node sections in the derivative matrices). Taking the aforementioned into account, $\partial X'/\partial X$ can be symbolically represented as in figure 4.3.

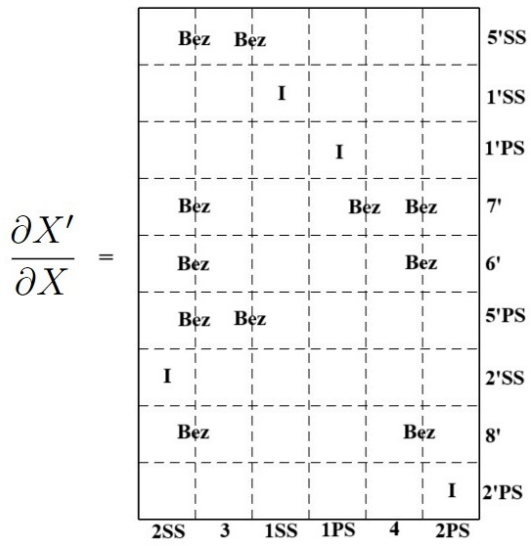

Figure 4.3: *Partial derivative $\partial X'/\partial X$ matrix.*

In the matrix of figure 4.3 the rows represent the nodes of the main body and flap, and the columns the nodes of the initial airfoil. All cells that are left empty contain zeros, the cells with the I symbol represent diagonal identity matrices and the Bez symbol refers to the differentiation of Bézier curve nodes. As stated before, sections 1 and 2 remain identical in the main body and flap, respectively, hence the I symbol in the corresponding cells. For the Bézier curves, the airfoil nodes that affect each one's control points are where the Bez symbol is written. Specifically, the control points of curve 8' are dependent on two nodes on each side of the airfoil, the previous and next nodes of the cutting node on each side. These nodes are implemented in the calculation of the slope and curvature of the airfoil at the cutting points (section 2.1). Curve 6' has the same node dependencies as it is a part of curve 8'. The control points of curve 7' include some of Bézier 8' nodes, thus it has the same dependencies, plus two more nodes on the pressure side between sections 1 and 4. Lastly, curve 5' control points are affected by three nodes in the suction side of the airfoil.

To analytically differentiate the Bézier curve nodal coordinates w.r.t. the airfoil nodal coordinates, the control point coordinates need to be differentiated first, and then the following equation must be applied:

$$\frac{\partial X'(t)}{\partial X} = \sum_{i=0}^{N} B_i^N(t) \frac{\partial X_{CP,i}}{\partial X} \tag{4.14}$$

Equation 4.14 derives from equation 2.1 after differentiating it w.r.t. the airfoil node coordinates. As can be observed from equation 2.2, the Bernstein polynomial is not dependent on the airfoil nodes, therefore only the derivative of the control points is present in the expression. For each of the three Bézier curves, their control

points' coordinates are differentiated w.r.t. the airfoil nodes' coordinates to create the $\partial X_{CP}/\partial X$ matrix. Subsequently, expression 4.14 is applied and the $\partial X'/\partial X$ matrix is computed for each Bézier curve. The reader is referred to appendix A for a detailed description of the way each Bézier curve of the main body and flap is differentiated w.r.t. the airfoil nodal coordinates. Given that $dX/d\vec{b}_{par}$ is already calculated in section 4.3, the chain rule can be applied as follows:

$$\frac{d\vec{x'}}{d\vec{b}_{par}} = \frac{\partial\vec{x'}}{\partial\vec{x}}\frac{d\vec{x}}{d\vec{b}_{par}} + \frac{\partial\vec{x'}}{\partial\vec{y}}\frac{d\vec{y}}{d\vec{b}_{par}} \tag{4.15}$$

$$\frac{d\vec{y'}}{d\vec{b}_{par}} = \frac{\partial\vec{y'}}{\partial\vec{x}}\frac{d\vec{x}}{d\vec{b}_{par}} + \frac{\partial\vec{y'}}{\partial\vec{y}}\frac{d\vec{y}}{d\vec{b}_{par}} + \frac{\partial\vec{y'}}{\partial\vec{b}_{par}} \tag{4.16}$$

It should be noted that equation 4.16 has one extra term in comparison to 4.15. This is due to the fact that some of the y coordinates of the control points are not only dependent on the PARSEC design variables indirectly through the airfoil nodes, but also directly (since they are calculated as new PARSEC nodes). As a result, the partial derivative $\partial\vec{y'}/\partial\vec{b}_{par}$ is added at the end of expression 4.16, for the chain rule to be correct.

In regard to the PARSEC design variables, one more derivative matrix is still to be calculated, the $\partial X''/\partial X'$ derivative of the main body and flap's nodes post-deployment w.r.t. the same nodes' coordinates pre-deployment. The flap deployment includes a translation to the right and downwards, and a rotation, as explained in section 2.4. Equation 2.42 transforms into

$$\begin{bmatrix}\vec{x''}\\ \vec{y''}\end{bmatrix} = \begin{bmatrix}\cos\varphi & -\sin\varphi\\ \sin\varphi & \cos\varphi\end{bmatrix}\begin{bmatrix}\vec{x'}+\Delta x-x_0\\ \vec{y'}+\Delta y-y_0\end{bmatrix} + \begin{bmatrix}x_0\\ y_0\end{bmatrix} \tag{4.17}$$

where ϕ is the rotation angle, Δx and Δy are the translation values, and x_0, y_0 are the coordinates of the rotation axis. From equation 4.17 the partial derivatives $\partial X''/\partial X'$ are calculated as follows:

$$\frac{\partial\vec{x''}}{\partial\vec{x'}} = \cos\phi,\ \frac{\partial\vec{x''}}{\partial\vec{y'}} = -\sin\phi,\ \frac{\partial\vec{y''}}{\partial\vec{x'}} = \sin\phi,\ \frac{\partial\vec{y''}}{\partial\vec{y'}} = \cos\phi \tag{4.18}$$

The derivatives of equation 4.18 are, naturally, only applied to the flap nodes, as the main body is constant during the flap's deployment. Consequently, the $\partial X''/\partial X'$ matrix is symbolically represented in figure 4.4 with identity matrices for the main body nodes and the Rot symbol which denotes the rotation matrix differentiation for the flap nodes.

$$\frac{\partial X''}{\partial X'} =$$

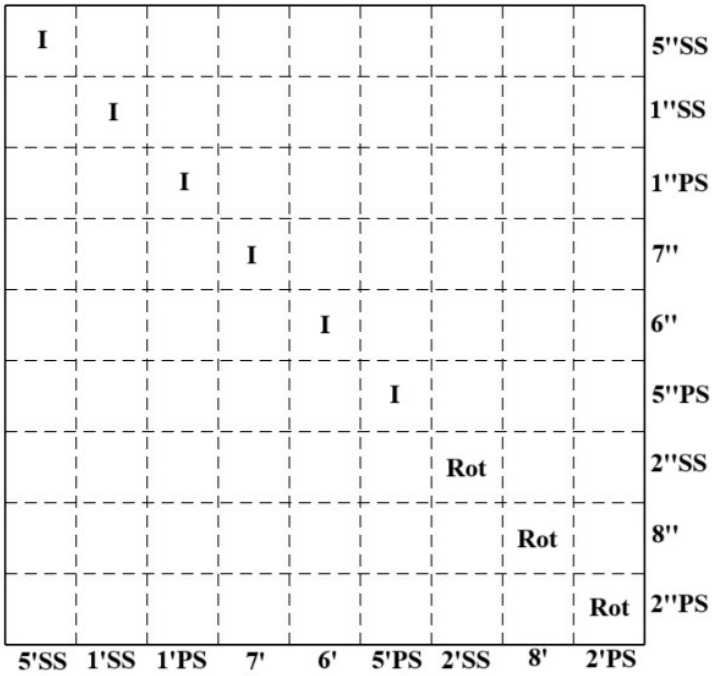

Figure 4.4: *Partial derivative $\partial X''/\partial X'$ matrix.*

The total derivatives of the main body and deployed flap's nodes w.r.t. the PARSEC design variables are calculated as follows:

$$\frac{d\vec{x''}}{d\vec{b}_{par}} = \frac{\partial \vec{x''}}{\partial \vec{x'}} \frac{d\vec{x'}}{d\vec{b}_{par}} + \frac{\partial \vec{x''}}{\partial \vec{y'}} \frac{d\vec{y'}}{d\vec{b}_{par}} \tag{4.19}$$

$$\frac{d\vec{y''}}{d\vec{b}_{par}} = \frac{\partial \vec{y''}}{\partial \vec{x'}} \frac{d\vec{x'}}{d\vec{b}_{par}} + \frac{\partial \vec{y''}}{\partial \vec{y'}} \frac{d\vec{y'}}{d\vec{b}_{par}} \tag{4.20}$$

All the necessary matrices of geometric derivatives have been calculated and equation 4.11 can be transformed into the following:

$$\frac{dF}{d\vec{b}_{par}} = \frac{\partial F}{\partial \vec{x''}} \frac{d\vec{x''}}{d\vec{b}_{par}} + \frac{\partial F}{\partial \vec{y''}} \frac{d\vec{y''}}{d\vec{b}_{par}} \tag{4.21}$$

As previously discussed, PUMA outputs the partial derivatives of the objective function w.r.t. the main body and flap's nodal coordinates, $\partial F/\partial \vec{x''}$ and $\partial F/\partial \vec{y''}$, in every optimization cycle. With the sequence of calculations that is described in the current subsection, derivatives $d\vec{x''}/d\vec{b}_{par}$ and $d\vec{y''}/d\vec{b}_{par}$ are computed, and expression 4.21 is utilized to determine the sensitivity derivatives w.r.t. the PARSEC design variables.

4.4.2 Sensitivity Derivatives w.r.t. Flap Design Variables

The sensitivity derivatives w.r.t. the flap design variables are to be calculated, so that expression 4.13 can be applied. From expression 4.12, only the $dX'/d\vec{b}_{flap}$ matrix is yet to be determined, since the $\partial X''/\partial X'$ derivative is present also in subsection 4.4.1. It is noted that, in expression 4.12, the total derivative of the main body and flap nodes w.r.t. the flap design variables is used for the chain rule, because, as is evident in section 3.1.2, these design variables do not affect the initial airfoil. As a result, sections 1' and 2' of the main body and flap nodes are not dependent on the flap design variables. The matrix containing the $dX'/d\vec{b}_{flap}$ derivative values is illustrated in figure 4.5.

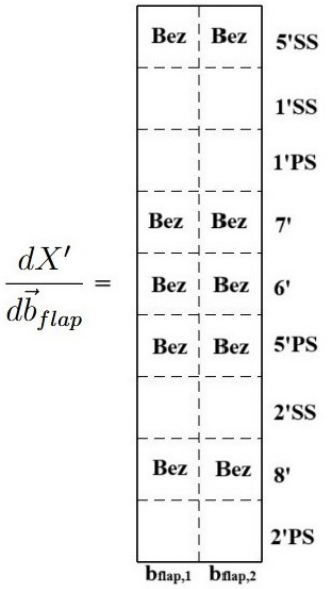

Figure 4.5: *Derivative $dX'/d\vec{b}_{flap}$ matrix.*

As for the matrix of figure 4.3, the Bez symbol in figure 4.5 indicates the analytical differentiation of Bézier curve nodes, in this instance w.r.t. the flap design variables. The derivatives of each Bézier curve's control points are first computed, and afterwards,

$$\frac{dX'(t)}{d\vec{b}_{flap}} = \sum_{i=0}^{N} B_i^N(t) \frac{dX_{CP,i}}{d\vec{b}_{flap}} \tag{4.22}$$

is exercised to calculate the $dX'/d\vec{b}_{flap}$ derivative. The process of analytically differentiating the control point coordinates w.r.t. the flap design variables is described in appendix B.

After doing so for each Bézier curve, the $dX'/d\vec{b}_{flap}$ values are determined and the

following equations are implemented to calculate the sensitivity derivatives:

$$\frac{d\vec{x''}}{d\vec{b}_{flap}} = \frac{\partial\vec{x''}}{\partial\vec{x'}}\frac{d\vec{x'}}{d\vec{b}_{flap}} + \frac{\partial\vec{x''}}{\partial\vec{y'}}\frac{d\vec{y'}}{d\vec{b}_{flap}} \tag{4.23}$$

$$\frac{d\vec{y''}}{d\vec{b}_{flap}} = \frac{\partial\vec{y''}}{\partial\vec{x'}}\frac{d\vec{x'}}{d\vec{b}_{flap}} + \frac{\partial\vec{y''}}{\partial\vec{y'}}\frac{d\vec{y'}}{d\vec{b}_{flap}} \tag{4.24}$$

$$\frac{dF}{d\vec{b}_{flap}} = \frac{\partial F}{\partial\vec{x''}}\frac{d\vec{x''}}{d\vec{b}_{flap}} + \frac{\partial F}{\partial\vec{y''}}\frac{d\vec{y''}}{d\vec{b}_{flap}} \tag{4.25}$$

The $\partial X''/\partial X'$ derivatives that appear in equations 4.23 and 4.24 have been previously calculated as discussed in subsection 4.4.1. The sensitivity derivatives w.r.t. the flap design variables are determined from equation 4.25. The latter derivatives and those calculated from equation 4.21 account for the whole sensitivity derivatives of the takeoff configuration, as described in expression 4.13. In every optimization cycle, after determining the values of the sensitivity derivatives, the steepest descent method, which is described in equation 4.10, is used to update the design variables.

Chapter 5

MAEA Optimization Cases

5.1 General Case Description

This chapter presents the MAEA optimization runs carried out using the EASY software. Through the results, it is proven that the parameterization and geometry creation process described in chapters 2 and 3 can be implemented in an aerodynamic ShpO loop. The airfoil's performance is examined at the three operating points of table 5.1. These three operating points are considered either separately in SOO or together in MOO cases.

Operating Point	Configuration	Flight Conditions
$CR1$ (cruise)	Flap undeployed	5,000 m, 2^o AoA, 0.8 Mach
$CR2$ (cruise)	Flap undeployed	10,000 m, 2^o AoA, 0.8 Mach
$TO1$ (takeoff)	Flap deployed	sea level, 8^o AoA, 0.2 Mach

Table 5.1: *MAEA optimization operating points.*

The airfoil contour is parameterized using the 11 PARSEC parameters presented in figure 5.1, as discussed in subsection 3.1.1. 9 of the 11 PARSEC parameters serve as design variables for the optimization cases, as the y coordinate and y-gap of the trailing edge are kept constant. Since the following cases are optimized with a MAEA, lower and upper bounds must be set for all design variables. These bounds are calculated so as to avoid the formation of unrealistic airfoils. Some of the following optimization cases also implement the flap design variables, which, as discussed in subsection 3.1.2, affect the flap's chord length and shape. The flap design variable bounds are chosen with the aim of the flap chord length not exceeding 35% of the airfoil's, as in common practice this is usually the maximum utilized. For the deployed flap configuration of the airfoil, the flap is deployed as described in

section 2.4 (Δx = 0.3, Δy = -0.02, ϕ = -36^o and the suction side cutting node being the rotation axis). Table 5.2 lists the baseline, minimum and maximum values of all design variables.

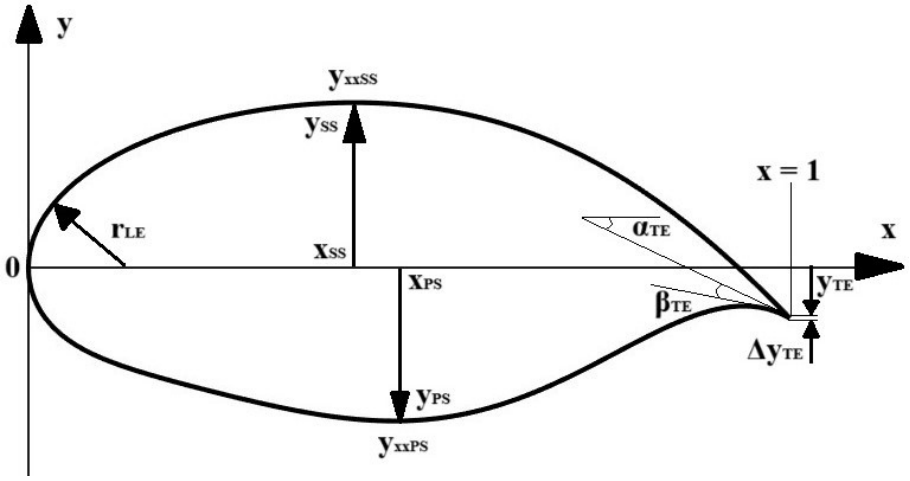

Figure 5.1: *PARSEC method for airfoil parameterization.*

Variable	Baseline	Minimum	Maximum
r_{LE}	0.01	0.075	0.0125
α_{TE}	-0.209439	-0.226	-0.186
β_{TE}	0.04363	0.03	0.06
x_{SS}	0.427949886	0.33	0.52
y_{SS}	0.065114543	0.05	0.08
$y_{xx,SS}$	-0.34989106	-0.5	-0.3
x_{PS}	0.480017747	0.4	0.58
y_{PS}	-0.060535044	-0.072	-0.048
$y_{xx,PS}$	0.597819177	0.5	0.7
$x_{suction,cut}$	0.95	0.925	0.99
D	0.225	0.1	0.25

Table 5.2: *Design variable baseline, minimum and maximum values, used as bounds during the MAEA optimization.*

With the baseline parameterization of table 5.2 the airfoil has the aerodynamic performance metrics listed in table 5.3, for each of the three operating points of table 5.1.

OP	Aerodynamic Performance Metrics		
CR1	$C_L = 0.5685$	$C_D = 0.05310$	$C_M \approx 0$
CR2	$C_L = 0.5325$	$C_D = 0.05417$	$C_M \approx 0$
TO1	$C_L = 3.156$	$C_D = 0.3161$	$C_M \approx 0$

Table 5.3: *Baseline aerodynamic performance metrics in each operating point.*

In addition, all optimization cases are constrained with some or all of the constraints described by the following expressions:

$$0.99A_{base} \leq A \leq 1.01A_{base} \tag{5.1}$$

$$C_{L,cruise} \geq C_{L,cruise,base} \tag{5.2}$$

$$0 \leq C_{M,cruise} \leq C_{M,cruise,base} \tag{5.3}$$

The constraint of expression 5.1 does not allow the area of the airfoil to differ more than 1% from the baseline area. Constraints 5.2 and 5.3 involve the cruise values of the lift and moment coefficients, respectively. Specifically for the area constraint, it is applied because, naturally, when optimizing with the drag as the objective, the process will tend to transform the airfoil into a flat plate, should the parameterization allow this to happen. The optimization cases studied in the following sections, their objectives, constraints and parameterizations are summarized in table 5.4. Prefix E marks cases studied using MAEAs (with the EASY software). The main settings applied to the MAEA are stated again as a reminder: termination criterion of either 500 CFD evaluations for SOO cases or 1000 for MOO cases, (μ,λ) = (20,40), real encoding, 95% crossover probability, 2% mutation probability, elite archive size of 15 for MOO cases, Radial Basis Function Networks activated once 70 evaluations respecting all constraints are archived in the database and, then, on each generation, 3 to 5 individuals are re-evaluated on the CFD tool.

Case	Objectives	Constraints	Design Variables
E1 (5.2)	min C_D at CR1	Area & C_L	PARSEC
E2a (5.3)	min C_D at CR1 & max C_L at TO1	Area	PARSEC
E2b (5.4)	min C_D at CR1 & max C_L at TO1	Area, C_L & C_M	PARSEC
E3 (5.5)	min C_D at CR2 & max C_L at TO1	Area, C_L & C_M	PARSEC
E4 (5.6)	max C_L at TO1	-	Flap
E5 (5.7)	min C_D at CR2 & max C_L at TO1	Area, C_L & C_M	PARSEC & Flap

Table 5.4: *MAEA optimization cases.*

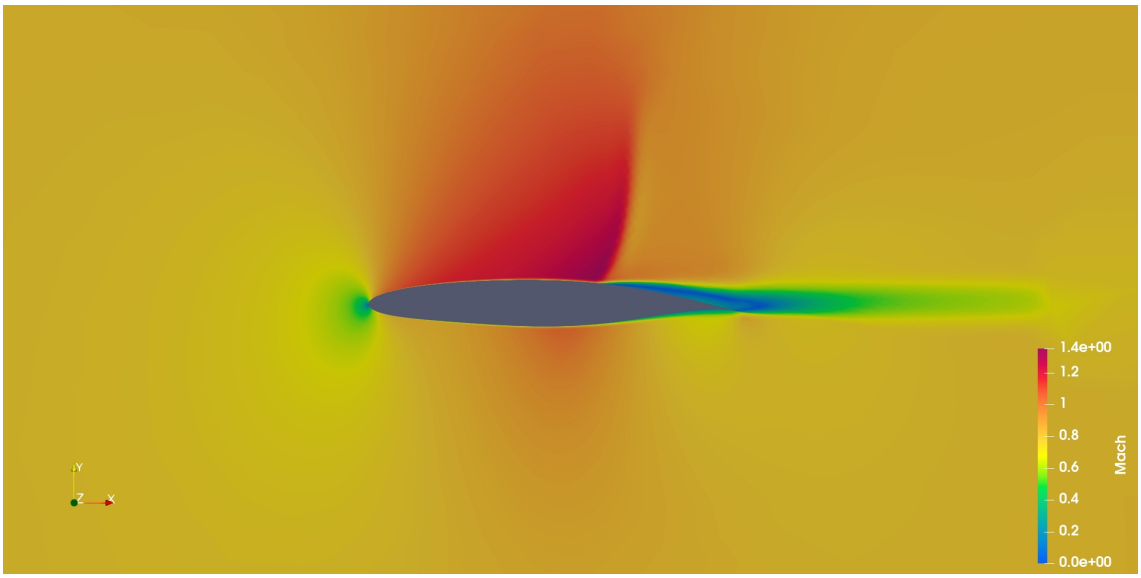

Figure 5.2: *Mach number field around baseline airfoil in cruise configuration.*

Figure 5.3: *Mach number field around baseline airfoil in takeoff configuration.*

Finally, after utilizing the PCOpt/NTUA in-house CFD solver PUMA, the Mach number field for the baseline airfoil in both configurations is plotted in figures 5.2 and 5.3, respectively. In the cruise configuration of the airfoil (figure 5.2) where the freestream Mach number is equal to 0.8, the compressibility effects of high-speed flow are visible, as a shock wave forms on the suction side of the airfoil. This is identified by the sharp transition in color gradient from deep red (supersonic) to orange (subsonic). Downstream of the shock wave, the flow is separated and the wake is identified by the blue and green colors. Furthermore, the stagnation point

of the airfoil is visible at the leading edge, and the flow seems to be accelerating also on the pressure side, due to its curvature, but remains subsonic. Conversely, in the takeoff configuration of the airfoil (figure 5.3) the flow remains subsonic everywhere, and the stagnation points of the airfoil and flap are visible on their pressure sides and not on the leading edges, since the AoA is equal to 8^o. The flow is accelerated slightly on the suction side of each element, the Mach number is roughly zero inside the slot, and due to the dominant viscous effects of low-speed flow the wake of the main body displays turbulence.

5.2 Case E1

A first SOO study aims to minimize the drag coefficient at cruise, and is synoptically described in table 5.5. Since this study is exclusively for cruise, no flaps are involved and the whole airfoil should be designed.

Case	**Type**	**Objectives**		
E1	SOO	C_D at CR1 ✓	C_D at CR2 **X**	C_L at TO1 **X**
Constraints:		Area ✓	$C_{L,cruise}$ ✓	$C_{M,cruise}$ **X**
Design Variables:		PARSEC ✓		Flap **X**

Table 5.5: *Case E1 details.*

The MAEA yielded an optimized solution with a 34% decrease in drag coefficient at cruise. This can be assessed as a very significant decrease in the objective function value, considering that the baseline airfoil is utilized in real-world applications, and the optimization did not affect its area or decrease its lift (1.8% increase in lift). The airfoil, also, remains trimmed as there wasn't a significant increase in its moment coefficient. Therefore, the effectiveness of the optimization method in minimizing the drag of an airfoil parameterized by the PARSEC method has been validated through this case. The optimized and baseline airfoil boundaries are compared in figure 5.4, and the convergence history of the algorithm is displayed in figure 5.5.

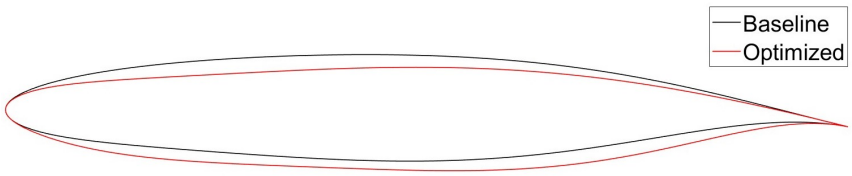

Figure 5.4: *Case E1: Comparison of the baseline and optimized airfoil geometries.*

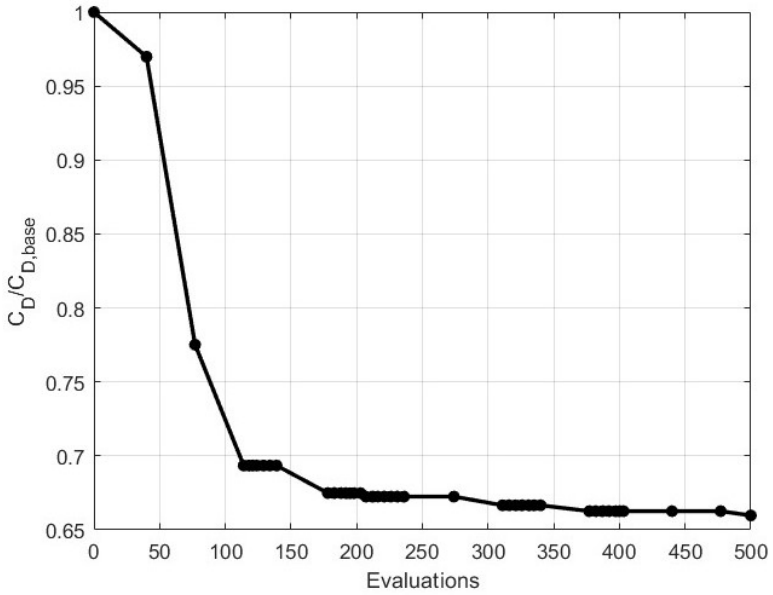

Figure 5.5: *Case E1: MAEA convergence history.*

As observed from figure 5.4, the optimization led both sides of the airfoil to a downward displacement in order to minimize its drag while maintaining an almost constant area value. From the MAEA convergence history of figure 5.5 it seems that after roughly 175 evaluations, the objective function value decreases very slightly. Consequently, the extra 325 expensive evaluations may not be justified for a decrease in drag at cruise under 2%. Moreover, the dots in figure 5.5 represent MAEA generations, highlighting the fact that after roughly 100 evaluations, the metamodel is activated, and thus fewer evaluations are required between generations.

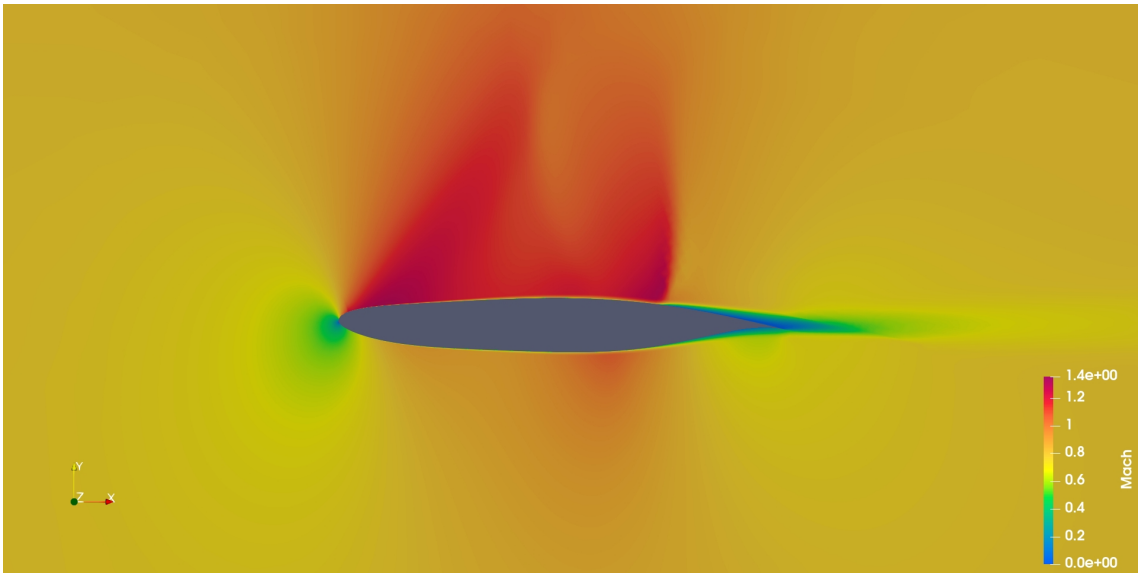

Figure 5.6: *Case E1: Mach number field around optimized airfoil.*

The Mach number field around the optimized airfoil is displayed in figure 5.6. By comparing figure 5.6 with figure 5.2, which displays the Mach field around the baseline airfoil, conclusions can be drawn about the differences in the flow due to the optimization. The two key differences concern the shock wave and the flow separation and wake thickness. The shock wave formed on the baseline airfoil is located more upstream and seems stronger (indicated by the sharp color gradient), signifying that the optimization delayed and weakened the shock in order to reduce wave drag and improve pressure recovery. Moreover, the boundary layer that forms downstream of the shock wave and the wake are thinner around the optimized airfoil, resulting in reduced pressure drag and improved efficiency. In summary, the changes to the flow field displayed in figure 5.6 reflect the objective of this optimization case.

5.3 Case E2a

This case optimizes the objective functions of both the first cruise and the takeoff operating points of the airfoil, as detailed in table 5.6, thus, it is a MOO case. As discussed in subsection 4.1.1, solving MOO cases with a MAEA produces a front with all non-dominated solutions the algorithm computed (or as many as the user has specified). After 1000 CFD evaluations, the front of non-dominated solutions of figure 5.7 was produced.

Case	**Type**	**Objectives**		
E2a	MOO	C_D at CR1 ✓	C_D at CR2 **X**	C_L at TO1 ✓
Constraints:		Area ✓	$C_{L,cruise}$ **X**	$C_{M,cruise}$ **X**
Design Variables:		PARSEC ✓		Flap **X**

Table 5.6: *Case E2a details.*

As can be observed from the front of non-dominated solutions of figure 5.7, 8 non-dominated solutions were calculated by the MAEA, 7 of which dominate the baseline airfoil. The solution with the lowest cruise drag coefficient shows a 35% decrease in drag, while the takeoff lift increased by 0.75%. On the other hand, the solution with the highest lift at takeoff has a 4.2% and 2% increase in takeoff lift and drag at cruise, respectively. A better choice for increasing the airfoil's takeoff lift is, definitely, the solution with the second highest lift coefficient, which increases the lift by 4.1% and decreases the drag at cruise by 28%. The two endpoints' airfoil boundaries are plotted in comparison to the baseline one in figure 5.8. Lastly, the main body and flap boundaries of the same solutions are also plotted in figure 5.9.

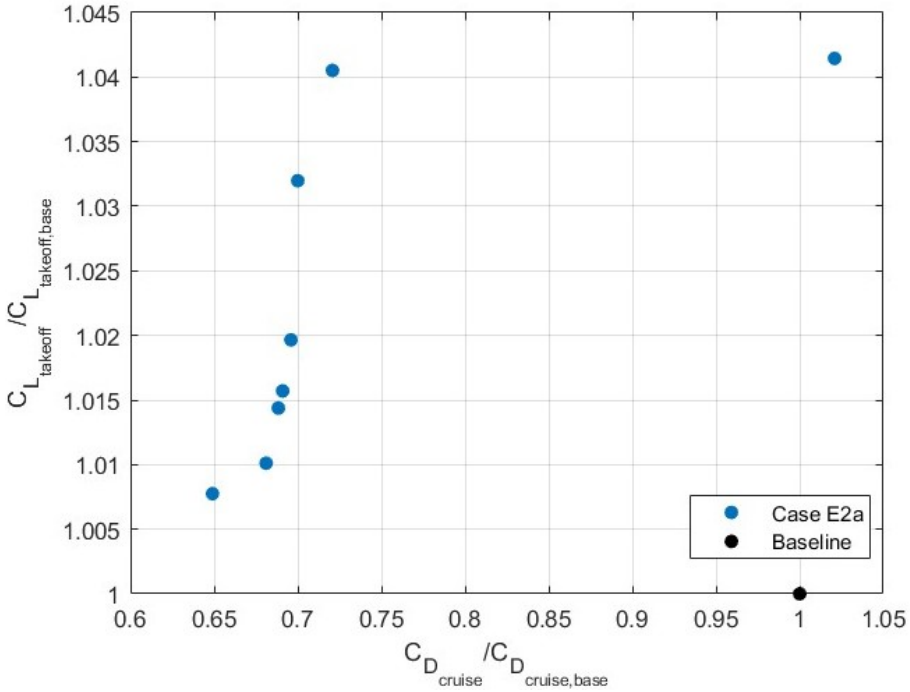

Figure 5.7: *Case E2a: Front of non-dominated solutions.*

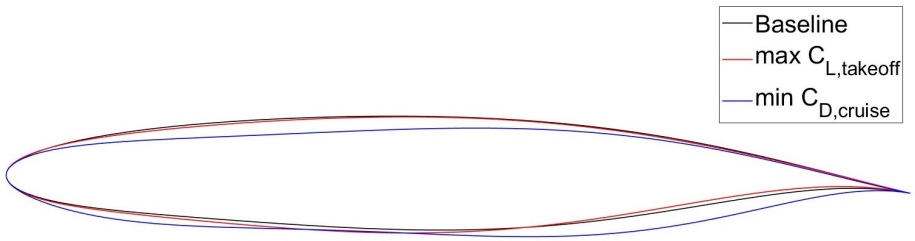

Figure 5.8: *Case E2a: Comparison of the baseline and optimized airfoil geometries at cruise.*

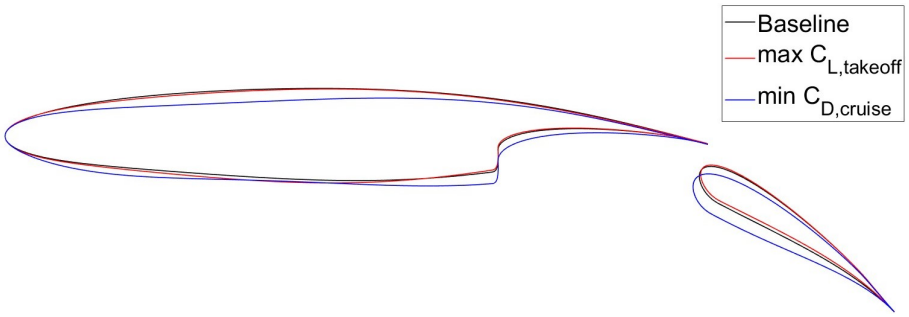

Figure 5.9: *Case E2a: Comparison of the baseline and optimized main body and flap geometries at takeoff.*

5.4 Case E2b

This case is a variant of case E2a (5.3), with the exact same conditions and objective functions, though with extra constraints, as shown in table 5.7. The front of non-dominated solutions computed by the MAEA is shown in figure 5.10.

Case	**Type**	**Objectives**		
E2b	MOO	C_D at CR1 ✓	C_D at CR2 **X**	C_L at TO1 ✓
Constraints:		Area ✓	$C_{L,cruise}$ ✓	$C_{M,cruise}$ ✓
Design Variables:		PARSEC ✓		Flap **X**

Table 5.7: *Case E2b details.*

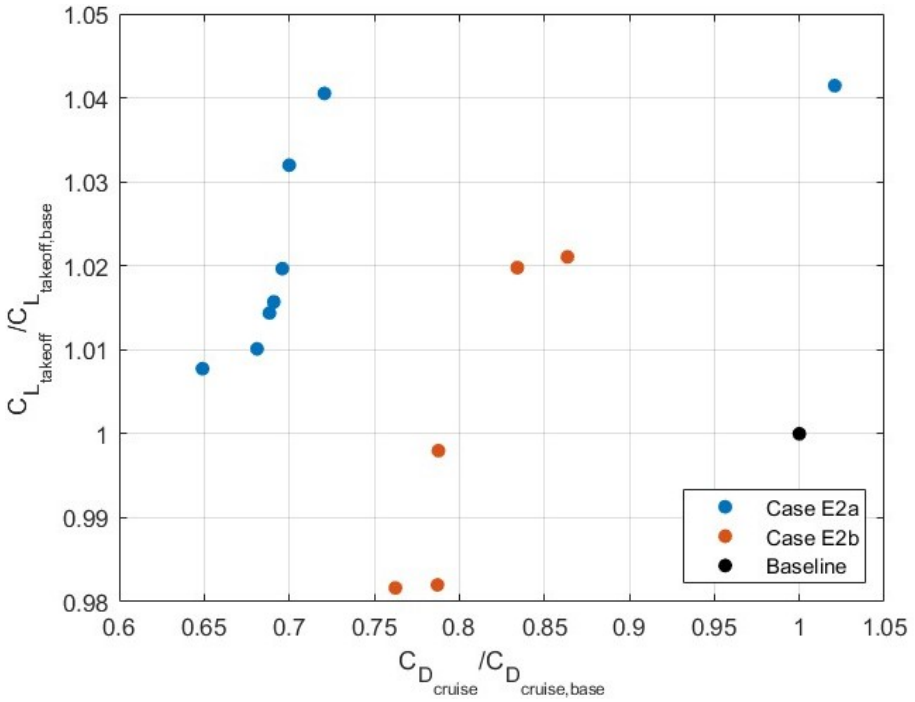

Figure 5.10: *Case E2b: Front of non-dominated solutions compared to the one computed in case E2a.*

In figure 5.10 the fronts from cases E2a and E2b are compared. Naturally, as more constraints are imposed in optimization case E2b, all of its computed non-dominated solutions are dominated by members of case E2a's front. Two of the members of the front of case E2b dominate the baseline airfoil, with the one corresponding to the highest lift showcasing a 2.1% increase in takeoff lift and a 14% decrease in cruise drag. The solution with the lowest drag coefficient has a 24% and 1.8% decrease

in drag at cruise and lift at takeoff, respectively. The contours of the airfoil at cruise and takeoff for the endpoint solutions of case E2b's front are compared to the baseline in figures 5.11 and 5.12, respectively.

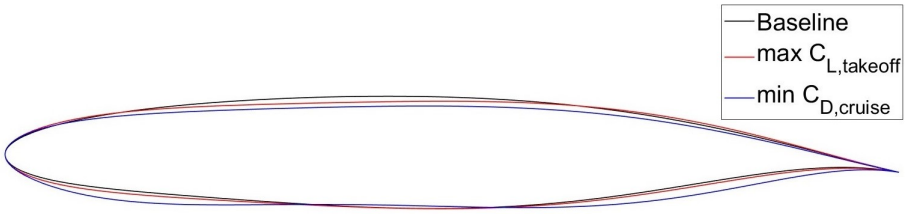

Figure 5.11: *Case E2b: Comparison of the baseline and optimized airfoil geometries at cruise.*

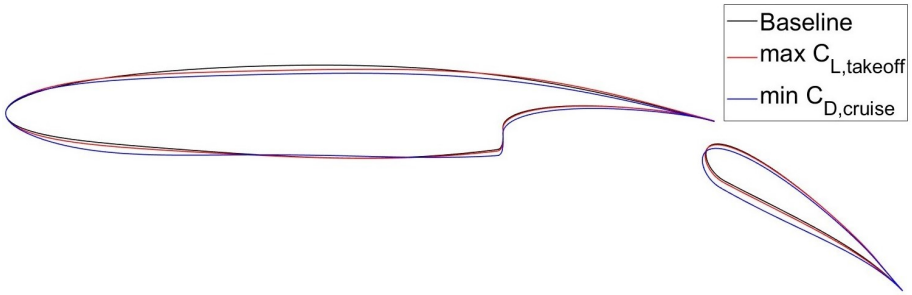

Figure 5.12: *Case E2b: Comparison of the baseline and optimized main body and flap geometries at takeoff.*

5.5 Case E3

This case involves both the cruise and takeoff configurations of the airfoil (with deployed flap in the latter), as displayed in table 5.8. Nevertheless, only the airfoil shape changes, whereas the flap characteristics do not change.

Case	**Type**	**Objectives**		
E3	MOO	C_D at CR1 **X**	C_D at CR2 ✓	C_L at TO1 ✓
Constraints:		Area ✓	$C_{L,cruise}$ ✓	$C_{M,cruise}$ ✓
Design Variables:		PARSEC ✓		Flap **X**

Table 5.8: *Case E3 details.*

However, before the MOO, a SOO run for minimizing the drag coefficient at cruise (CR2) is carried out. The solution of the SOO then serves as initialization (it

is set as a member of the initial population of the MAEA along with the baseline parameterization) for the MOO problem, which affects the behavior of the algorithm, as all the other cases are initialized only by the baseline geometry.

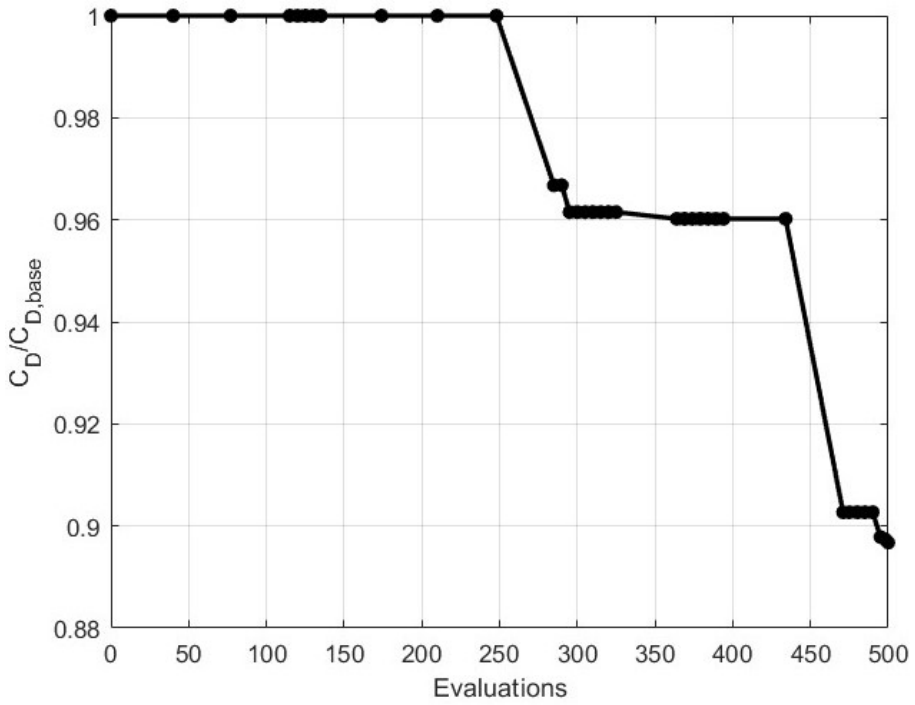

Figure 5.13: *Case E3: MAEA convergence history of SOO run.*

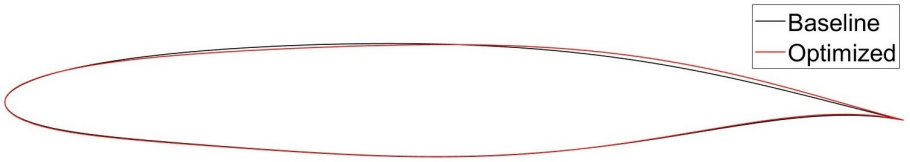

Figure 5.14: *Case E3: Comparison of the baseline and SOO-zed solution airfoil geometries.*

The SOO case computes a solution with a 10.3% decrease in drag coefficient at cruise (CR2), while the lift at cruise is increased by 4.9%. This geometry is compared to the baseline in figure 5.14, and the convergence history of the algorithm is displayed in figure 5.13. In the subsequent phase, this solution is injected into the initial population and the MOO case is carried out. The front of non-dominated solutions computed by the MAEA is displayed in figure 5.15.

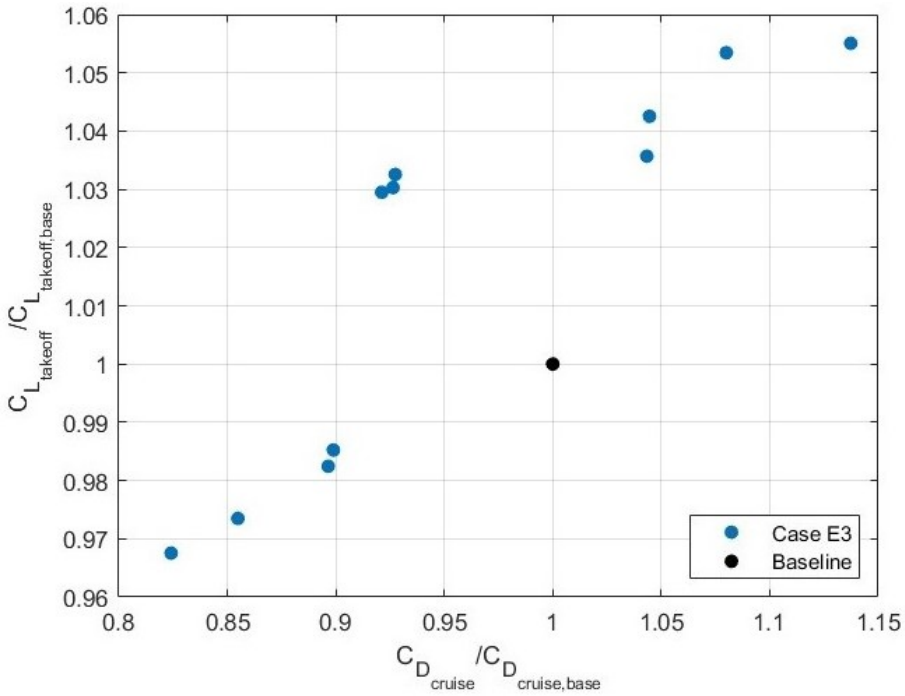

Figure 5.15: *Case E3: Front of non-dominated solutions.*

As illustrated by the front of non-dominated solutions, the optimization computed a wide variety of solutions, from very low drag at cruise to high lift at takeoff, including three solutions that dominate the baseline geometry. The solution with the lowest drag coefficient at cruise has a significant decrease in drag, 17.6%, with a 3.3% decrease in lift at takeoff. On the other hand, the maximum takeoff lift solution increased the airfoil lift at takeoff by 5.5%, while also increasing the drag at cruise by 13.7%. Moreover, the three solutions that dominate the baseline geometry result approximately in a 7.5% decrease in drag at cruise and a 3.1% increase in takeoff lift, thus enhancing both objectives. This wide variety of solutions computed by this optimization method provides options to choose from, according to which objective is perceived as more important (or based on other criteria not considered in the optimization).

Finally, the maximum takeoff lift and minimum drag at cruise geometries are compared to the baseline in figures 5.16 and 5.17, while one of the geometries dominating the baseline is also compared to it in figures 5.18 and 5.19. From these figures, it can be observed that the variations in the boundaries of the endpoint solutions in comparison to the baseline geometry are much more prominent than those in the dominating solution's boundary. Figures 5.17 and 5.19 highlight the fact that, in the current case, only the PARSEC parameters serve as design variables, since only the airfoil contour is altered and the deployed flap remains the same.

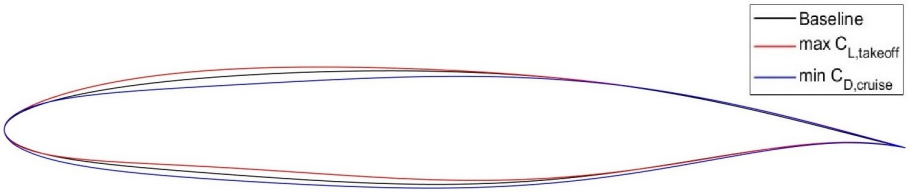

Figure 5.16: *Case E3: Comparison of the baseline and optimized airfoil geometries at cruise.*

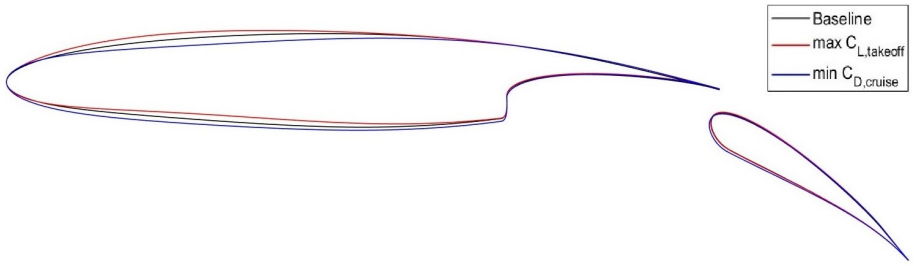

Figure 5.17: *Case E3: Comparison of the baseline and optimized main body and flap geometries at takeoff.*

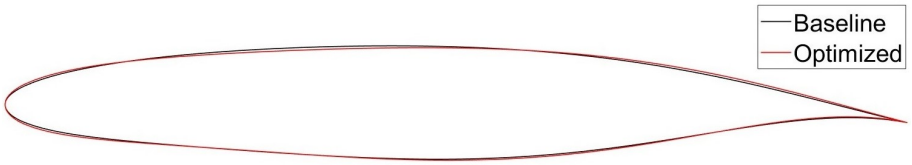

Figure 5.18: *Case E3: Comparison of the airfoil geometries of a solution dominating the baseline, at cruise.*

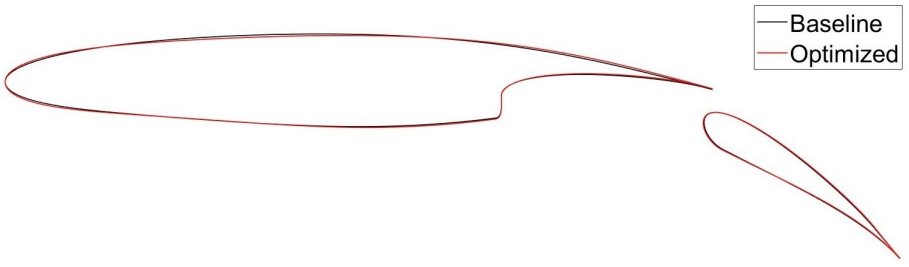

Figure 5.19: *Case E3: Comparison of the main body and flap geometries of a solution dominating the baseline, at takeoff.*

5.6 Case E4

As discussed in subsection 3.1.2, two additional parameters concerning the flap are utilized as design variables in the examined cases. These design variables, which are defined in expressions 3.4 and 3.5, offer an extra degree of freedom when optimizing the airfoil in its deployed flap configuration, since they affect the points at which the airfoil is cut. Therefore, the flap's chord length and shape can be altered without changing the initial airfoil's contour (constant PARSEC design variables). The current case is a SOO case implementing only the two flap design variables, with the objective being the lift coefficient at takeoff, as detailed in table 5.9.

Case	**Type**	**Objectives**		
E4	SOO	C_D at CR1 **X**	C_D at CR2 **X**	C_L at TO1 ✓
Constraints:		Area **X**	$C_{L,cruise}$ **X**	$C_{M,cruise}$ **X**
Design Variables:		PARSEC **X**		Flap ✓

Table 5.9: *Case E4 details.*

The design variable bounds for this case are not of high importance, as the optimization will always minimize the parameter of expression 3.4 and maximize that of expression 3.5, in order to maximize the flap's chord length and, thus, maximize the lift enhancement. No constraints are applied in this case, as the airfoil's area is not affected and the other constraints concern only aerodynamic performance metrics of the airfoil at cruise.

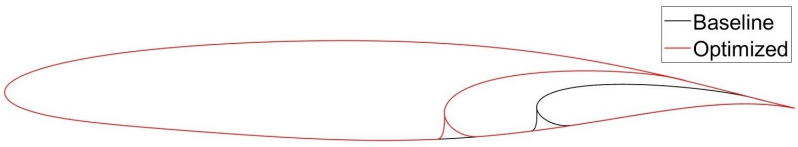

Figure 5.20: *Case E4: Comparison of the baseline and optimized main body and flap geometries.*

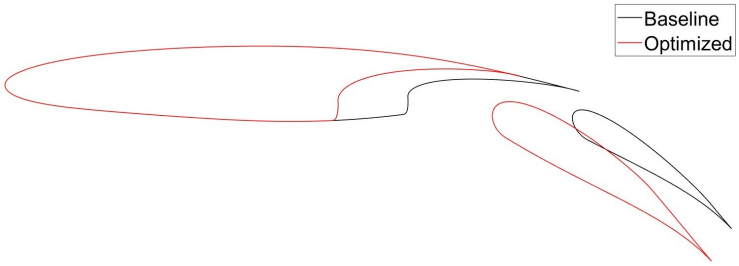

Figure 5.21: *Case E4: Comparison of the baseline and optimized deployed flap airfoils.*

Figure 5.20 compares the baseline and optimized boundaries of the main body and flap. As can be observed from this figure, the airfoil boundary is unaltered and the only differences in the two geometries are associated with the flap. In figure 5.21, where the deployed flap configuration of the airfoil is displayed, it is evident that the flap geometry changed but the deployment angle and translation remain unaltered. The optimized geometry exhibits a 4.9% increase in lift coefficient at takeoff, as can also be observed from figure 5.22 which presents the convergence history of the algorithm, while the drag at cruise would, of course, be the same as the baseline's. However, the drag at takeoff is also increased by 11.6%. Through this optimization case, the ability of the flap to enhance the airfoil lift is validated.

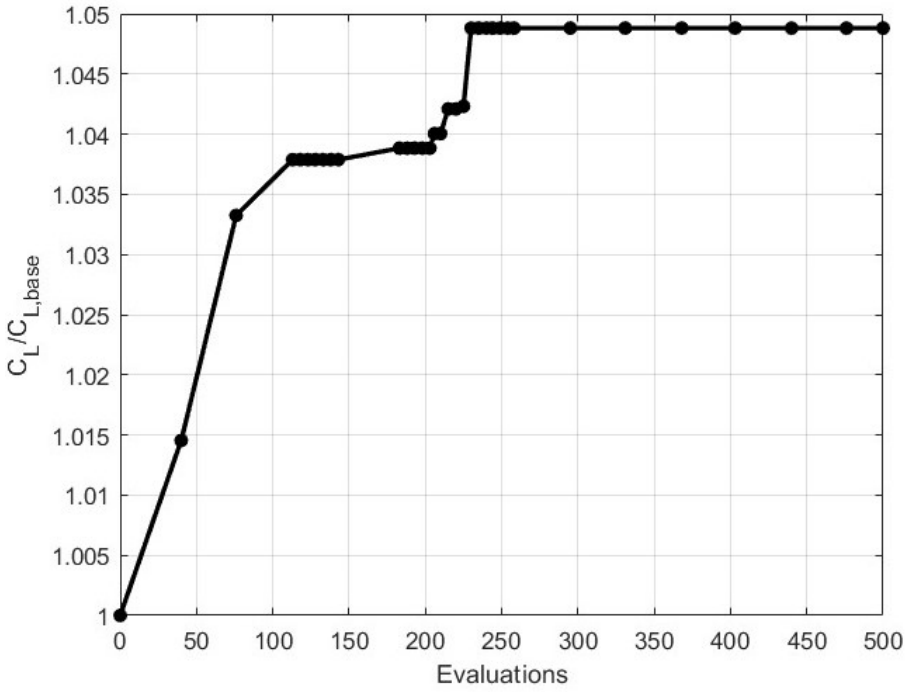

Figure 5.22: *Case E4: MAEA convergence history.*

The Mach number field for the optimized airfoil in its deployed flap configuration is plotted in figure 5.23. This figure can be compared to the baseline one (5.3) with the purpose of identifying the differences that the optimization caused in the flow field. The flow around the main body, especially upstream near the leading edge, is unaltered, since the airfoil boundary is kept constant. On the suction side of the flap, the region where the flow is accelerated is extended, indicating better flow attachment and less separation. The wake of both elements of the optimized airfoil seems, generally, less turbulent, resulting in more effective pressure recovery.

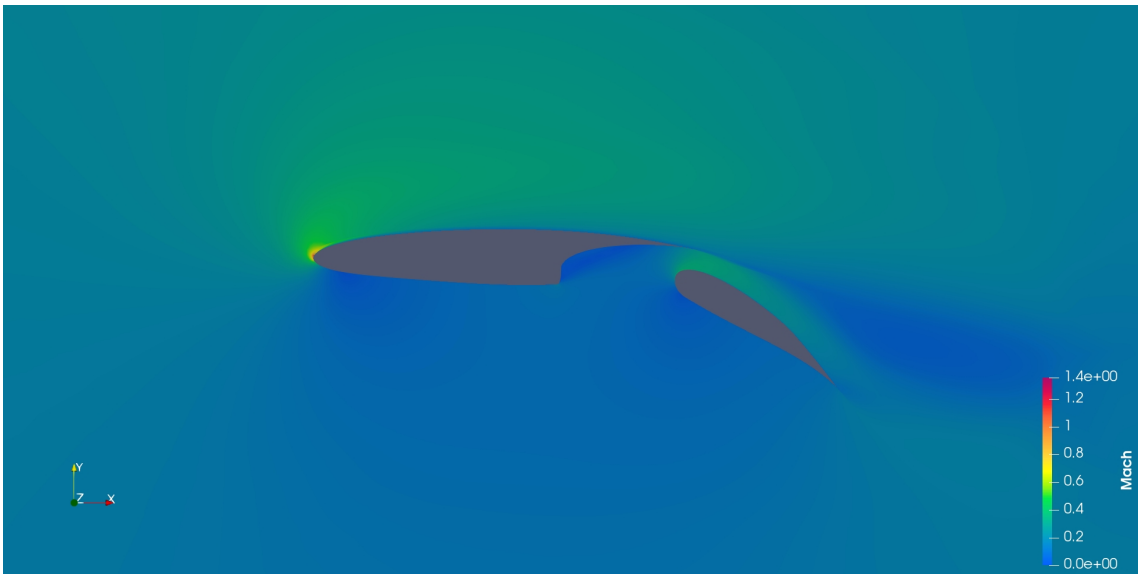

Figure 5.23: *Case E4: Mach number field around optimized airfoil.*

5.7 Case E5

The final optimization case executed with a MAEA in this diploma thesis is, essentially, the exact same as case E3 (5.5), with the addition of the two extra flap design variables. These design variables proved effective in optimizing the deployed flap airfoil's lift at takeoff without altering the airfoil boundary in case E4 (5.6). Therefore, an insightful comparison can be drawn between the cases E3 and E5, highlighting the possible benefits of the two extra flap design variables. The configuration of case E5 is displayed in table 5.10.

Case	**Type**	**Objectives**		
E5	MOO	C_D at CR1 **X**	C_D at CR2 ✓	C_L at TO1 ✓
Constraints:		Area ✓	$C_{L,cruise}$ ✓	$C_{M,cruise}$ ✓
Design Variables:		PARSEC ✓		Flap ✓

Table 5.10: *Case E5 details.*

The front of non-dominated solutions of this case is displayed in figure 5.24. As can be observed from this figure, none of the solutions computed dominate the baseline geometry, since it has the highest lift coefficient. The MAEA seems to have searched for very low cruise drag solutions, while maintaining a takeoff lift close to the baseline's by extending the flap. The solution with the lowest drag coefficient at cruise shows an impressive 32.6% decrease in drag, while the lift coefficient at

takeoff decreased by 4%. The second to last solution (with the second highest lift coefficient) has a very high 25.8% decrease in drag and the lift only decreased by 1.3%. If the main goal of this case is minimizing the drag at cruise while not reducing the takeoff lift much, then many solutions achieving this are computed. However, the MAEA did not find any solution increasing the baseline lift at takeoff. The lowest drag at cruise solution's geometry is compared to the baseline in figures 5.25 and 5.26.

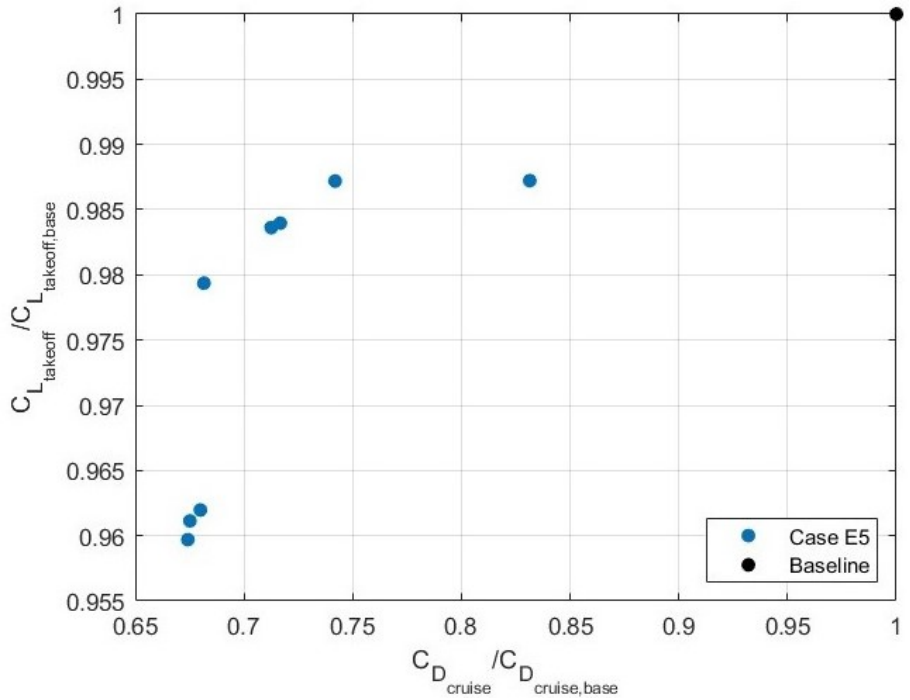

Figure 5.24: *Case E5: Front of non-dominated solutions.*

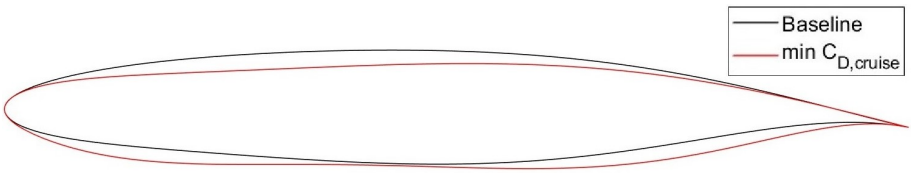

Figure 5.25: *Case E5: Comparison of the baseline and lowest drag airfoil geometries at cruise.*

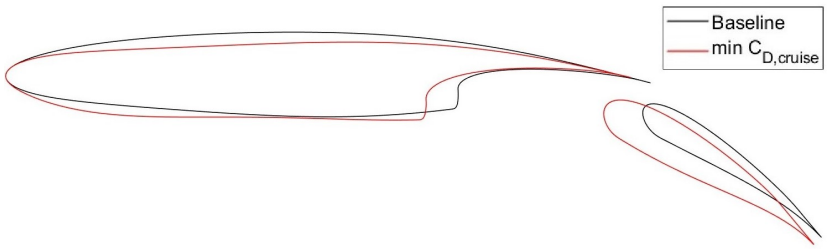

Figure 5.26: *Case E5: Comparison of the baseline and lowest drag main body and flap geometries at takeoff.*

From figure 5.25 it is observed that, in order to minimize the drag at cruise, the MAEA tends to lead the suction side of the airfoil to a downward displacement and flatten the pressure side. Moreover, figure 5.26 displays the flap chord length extension of the optimized solution. The two objectives of this MOO case are antagonistic, namely a decrease in drag at cruise through variations of the airfoil boundary leads to a decrease in the takeoff lift. Thus, since the MAEA has altered the airfoil's boundary in favor of the drag objective, it must increase the flap chord length, with the aim to maintain the same level of takeoff lift. As previously stated, cases E3 and E5 share the same configuration and conditions. The only differences pertain to the initialization and the two extra design variables of case E5. Case E3 is initialized with both the baseline geometry and an optimized solution from a SOO run targeting the drag at cruise objective, while case E5 is only initialized with the baseline geometry (initialization referring to the initial population of the MAEA). The two cases' fronts of non-dominated solutions are compared in figure 5.27.

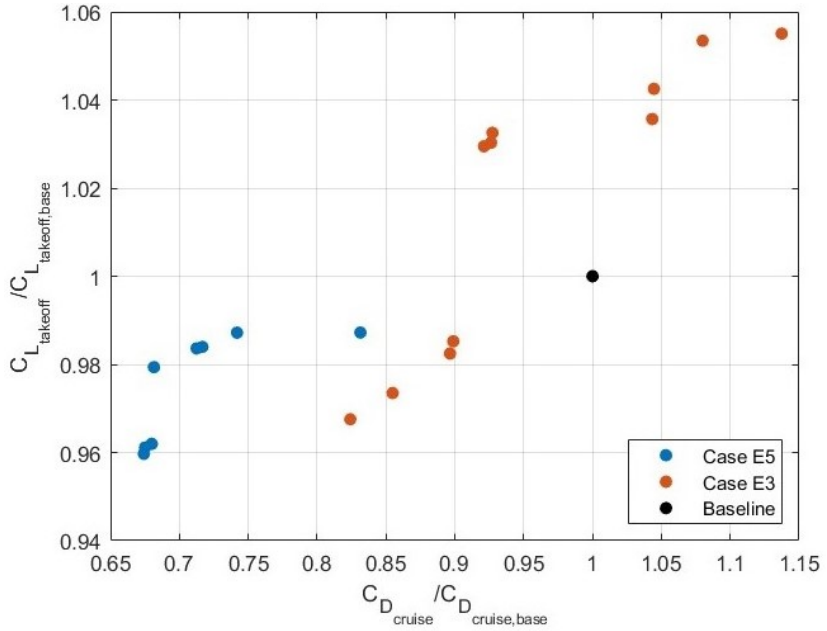

Figure 5.27: *Comparison of fronts of non-dominated solutions calculated in cases E3 and E5.*

Conclusions about the behavior of the MAEA in these two cases can be drawn from figure 5.27. The first 4 solutions of case E3 (counting from the lowest drag solution) are all dominated by members of case E5's front. This is attributed to the fact that, as explained before, the two flap design variables give the MAEA the freedom to explore PARSEC parameterizations with even lower drag at cruise while sustaining acceptable takeoff lift values. However, no other solutions computed in case E3 are dominated by solutions of case E5, as they have increased takeoff lift in comparison to the baseline. The complete front of non-dominated solutions from both cases would consist of all case E5 solutions and case E3 solutions excluding the first four, and is displayed in figure 5.28.

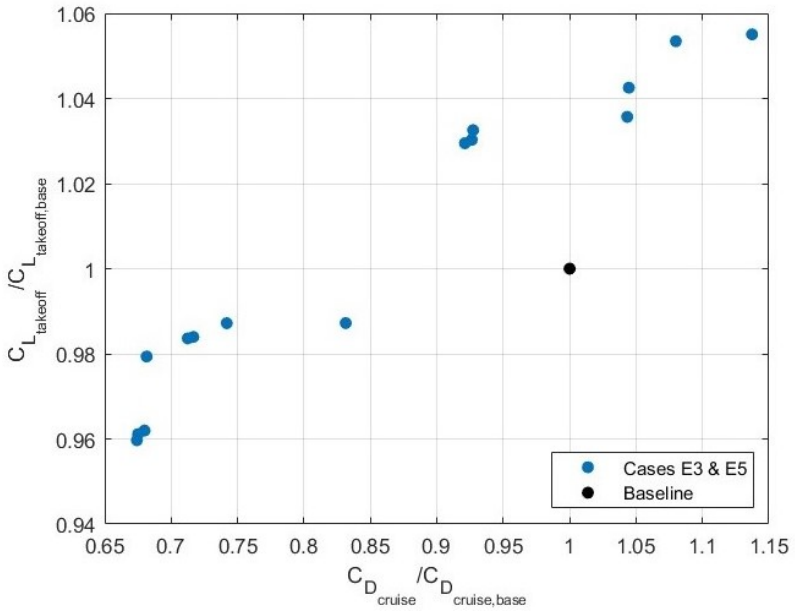

Figure 5.28: *Overall front of non-dominated solutions of cases E3 and E5.*

Finally, with the design variable bounds listed in table 5.2 the flap chord length can reach a maximum of roughly 35% of the airfoil chord. By decreasing the minimum bound for the first flap design variable $x_{suction,cut}$, the flap's chord length can increase even more. The case is executed for two more values of this variable's minimum bound, specifically 0.85 and 0.75, which correspond to approximately 40% and 50% flap chord length, respectively, and the corresponding fronts of non-dominated solutions are compared in figure 5.29. As stated also in case E4, the optimization will always minimize the $x_{suction,cut}$ design variable in order to maximize the flap chord length, with the aim of maximizing the airfoil lift at takeoff.

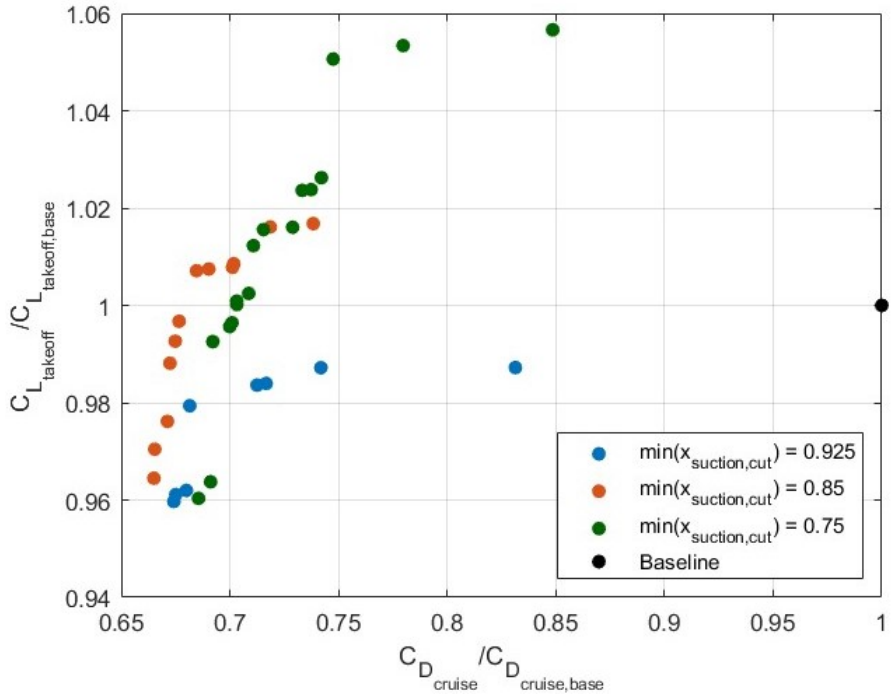

Figure 5.29: *Case 5: Comparison of fronts of non-dominated solutions with varying minimum bound for the $x_{suction,cut}$ design variable.*

According to figure 5.29, the increase in flap chord length allows the MAEA to calculate solutions at a very low cruise drag parameterization, but with a very long flap so that the takeoff lift even increases. There are solutions for the flap at 40% chord length (minimum $x_{suction,cut} = 0.85$) which dominate the baseline geometry. For example, the last solution of this front (counting from the lowest lift solution) has a 26.16% decrease in drag at cruise and a 1.68% increase in takeoff lift. This geometry is compared to the baseline in figures 5.30 and 5.31. Lastly, with the flap at 50% chord length (minimum $x_{suction,cut} = 0.75$) solutions with much higher takeoff lift and significantly decreased drag at cruise are computed. Specifically, the third to last solution of this front shows a 25.25% decrease in drag at cruise, while the takeoff lift is increased by 5.06%. These results, although impressive, may not be realistic in the case of most real world aircraft, since the flap's chord length rarely exceeds 35% of the airfoil's, let alone 50%.

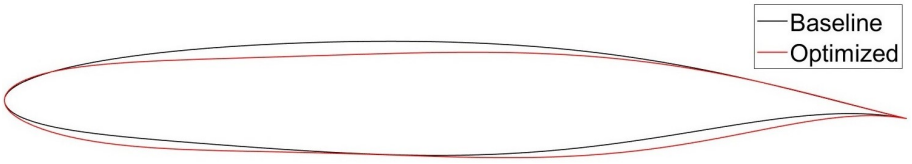

Figure 5.30: *Case E5: Comparison of airfoil geometries at cruise between the baseline geometry and the solution calculated with $x_{suction,cut} = 0.85$ or roughly 40% flap chord length.*

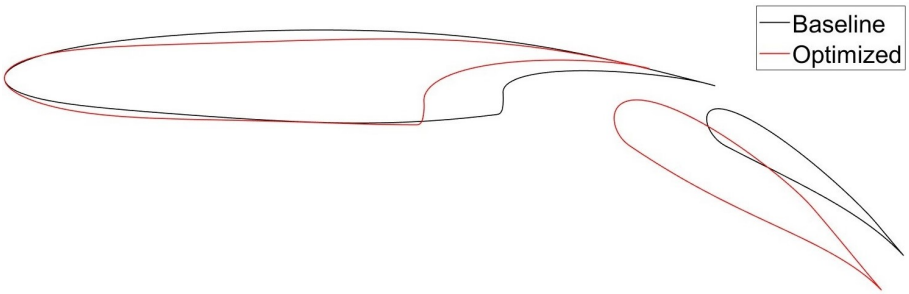

Figure 5.31: *Case E5: Comparison of main body and flap geometries at takeoff between the baseline geometry and the solution calculated with* $x_{suction,cut} = 0.85$ *or roughly 40% flap chord length.*

5.8 MAEA Optimization Conclusions

Conclusions about the behavior of a MAEA in optimizing a two-element airfoil geometry can be drawn from the optimization cases presented in sections 5.2, 5.3, 5.4, 5.5, 5.6 and 5.7. First of all, in all the above cases, the objectives were successfully optimized. Namely, the drag at cruise was minimized by altering the airfoil's contour, and the lift at takeoff was maximized by not only optimizing the airfoil's contour but also the flap parameters in the airfoil's deployed flap configuration. The MAEA method for these optimization cases proved extremely effective in handling the problems' strict constraints and producing fronts of non-dominated solutions in the cases where both objectives were implemented. Although a large number of expensive CFD evaluations were required, especially for the MOO cases, the MAEA explored the whole design space to good effect, while ensuring that all calculated solutions met each problem's requirements.

This is particularly apparent in case E3 (section 5.5). As is observed from this case's front of non-dominated solutions, which is displayed in figure 5.15, the optimization method was able to calculate a large variety of non-dominated solutions, ranging from very low drag at cruise to very high takeoff lift. Three solutions that dominate the baseline airfoil were calculated, as well, by the MAEA in this case. Simultaneously, all these solutions satisfy the conditions set by the constraints of eqs. 5.1, 5.2 and 5.3.

Furthermore, case E5 (section 5.7) expanded case E3 by introducing the two extra design variables, the flap parameters. With the two additional design variables, the MAEA obtained an extra degree of freedom, as the flap's shape could now also be optimized with the aim of maximizing the lift of the airfoil's deployed flap configuration. This allowed the optimization to explore very low drag at cruise parameterizations for the airfoil geometry, while maintaining an acceptable takeoff lift by optimizing the flap's shape, as can be seen in the front of figure 5.27. In total, the optimization produced the overall front of non-dominated solutions displayed in

figure 5.28.

Moreover, in case E5, the effect of the flap design variable bounds was studied. These design variables affect, among other things, the flap's chord length, which is a very important factor for the takeoff lift of an aircraft. By increasing the bounds for the flap design variables, the MAEA is allowed to compute solutions with longer flaps. Consequently, as it can be observed from the front of figure 5.29, solutions which greatly dominate the baseline were computed, and these stand for low drag airfoils with long flaps.

In conclusion, the MAEA optimization method paired with the geometry creation and parameterization process of chapters 2 and 3 was able to minimize the drag at cruise and/or maximize the takeoff lift of a two-element airfoil in each problem. In the MOO cases, various non-dominated solutions were calculated in each run of the algorithm, forming a front of non-dominated solutions. All imposed constraints were handled well, as the MAEA dismissed every solution not satisfying these conditions. The only serious deficiency of this optimization method is the large number of expensive CFD evaluations required.

Chapter 6

Adjoint Optimization Cases

6.1 General Case Description

In this chapter, the cases optimized with the adjoint method are presented. The optimization targets the minimization of the drag coefficient of the airfoil at cruise and the maximization of the lift coefficient of the deployed flap configuration of the airfoil (the flap deployment is described in section 2.4) at takeoff. The cruise and takeoff operating points are described in table 6.1.

Operating Point	Configuration	Flight Conditions
$CR1$ (cruise)	Flap undeployed	10,000 m, 2^o AoA, 0.8 Mach
$TO1$ (takeoff)	Flap deployed	sea level, 8^o AoA, 0.2 Mach

Table 6.1: *Adjoint optimization operating points.*

One or both objectives are selected for each case, signifying a SOO and a MOO run, respectively. The airfoil geometry is parameterized by the non-constant PARSEC parameters (3.1.1) and the two flap design variables (3.1.2). As applied in the MAEA optimization cases (chapter 5), the trailing edge y coordinate and y-gap are kept constant. The design variables' baseline values are displayed in table 6.2 (same as those for the MAEA cases). As a reminder, figure 6.1 is again displayed, where the PARSEC parameters are described.

All adjoint-based optimizations are unconstrained. However, in order to maintain an area value close to the baseline's, a minimum bound of 0.0075 is set for the leading edge radius r_{LE} of the airfoil in the optimization cases where the drag at cruise is the objective. The y coordinate of the airfoil at the maximum thickness of the pressure side y_{PS} is calculated from the corresponding suction side value y_{SS} as

follows:

$$y_{PS} = y_{SS} - (y_{SS,base} - y_{PS,base}) \tag{6.1}$$

Furthermore, with the aim of retaining a realistic deployed flap airfoil configuration, a minimum bound of 0.925 is set for $x_{suction,cut}$ and a maximum bound of 0.25 for D. As explained also in the optimization cases of chapter 5 that make use of the flap design variables, these bounds entail a flap with a chord length equal to roughly 35% of the airfoil's chord, which in most cases is the maximum chord length utilized for flaps.

Design Variable	Baseline Value
r_{LE}	0.01
α_{TE}	-0.209439
β_{TE}	0.04363
x_{SS}	0.427949886
y_{SS}	0.065114543
$y_{xx,SS}$	-0.34989106
x_{PS}	0.480017747
y_{PS}	-0.060535044
$y_{xx,PS}$	0.597819177
$x_{suction,cut}$	0.95
D	0.225

Table 6.2: *Design variable baseline values.*

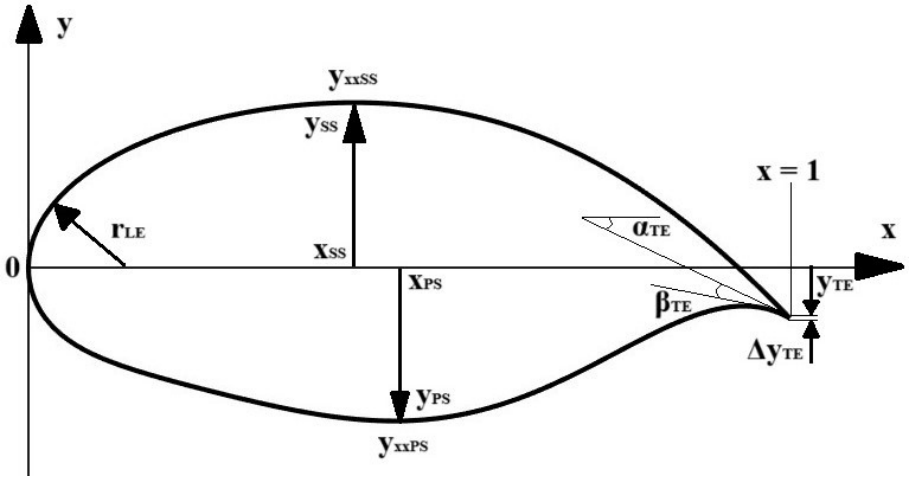

Figure 6.1: *PARSEC method for airfoil parameterization.*

In each of the two operating points of table 6.1, the baseline airfoil produces the aerodynamic performance metrics of table 6.3.

OP	Aerodynamic Performance Metrics		
CR1	$C_L = 0.5325$	$C_D = 0.05417$	$C_M \approx 0$
TO1	$C_L = 3.156$	$C_D = 0.3161$	$C_M \approx 0$

Table 6.3: *Baseline aerodynamic performance metrics in each operating point.*

In each optimization cycle, the primal problem is first solved with the current parameterization and the objective function value is computed. This involves solving the flow around the geometry with the PUMA software developed by the PCOpt/NTUA. At this point, if the convergence criterion of the optimization is met, the algorithm stops. Afterward, the adjoint problem is solved and the derivative of the objective function w.r.t. the geometry's nodes is calculated. This process is described in section 4.2. Nonetheless, with the purpose of updating the design variables for the next cycle, the sensitivity derivatives must be computed. For the cruise operating point, this transformation is explained in section 4.3 and for the takeoff one in 4.4. As stated in those sections, after calculating the sensitivity derivatives, the design variables are updated by implementing the steepest descent method, which is presented in the following equation:

$$\vec{b}^{k+1} = \vec{b}^{k} - \eta \frac{dF}{d\vec{b}}\bigg|_{k} \tag{6.2}$$

As observed by the following cases, this method proves highly effective in optimizing the objective function in a short number of cycles. Finally, the details of the adjoint-based optimization cases studied in this thesis are displayed in table 6.4, where prefix A refers to the adjoint-based optimization.

Case	Objectives	Constraints	Design Variables
A1 (6.2)	min C_D at CR1	-	PARSEC
A2 (6.3)	max C_L at TO1	-	Flap
A3 (6.4)	max C_L at TO1	-	PARSEC & Flap
A4 (6.5)	min C_D at CR1 & max C_L at TO1	-	PARSEC & Flap

Table 6.4: *Adjoint optimization cases.*

6.2 Case A1

In this case, the objective is minimizing the airfoil's drag at cruise conditions, as described in table 6.5. After 10 adjoint-based optimization cycles, the drag coefficient was decreased by 42.1%, while the lift coefficient was also decreased by 6.2%. The

baseline and optimized airfoils are compared in figure 6.2 and the optimization's convergence history is displayed in figure 6.3.

Case	**Type**	**Objectives**	
A1	SOO	C_D at CR1 ✓	C_L at TO1 **X**
Design Variables:		PARSEC ✓	Flap **X**

Table 6.5: *Case A1 details.*

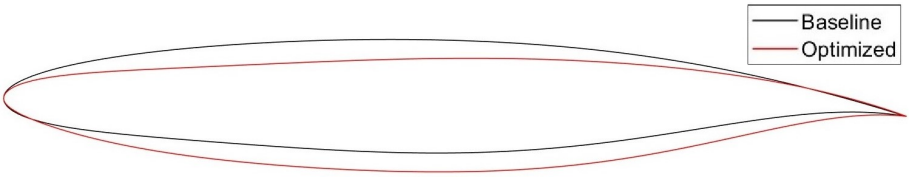

Figure 6.2: *Case A1: Comparison of baseline and optimized airfoils.*

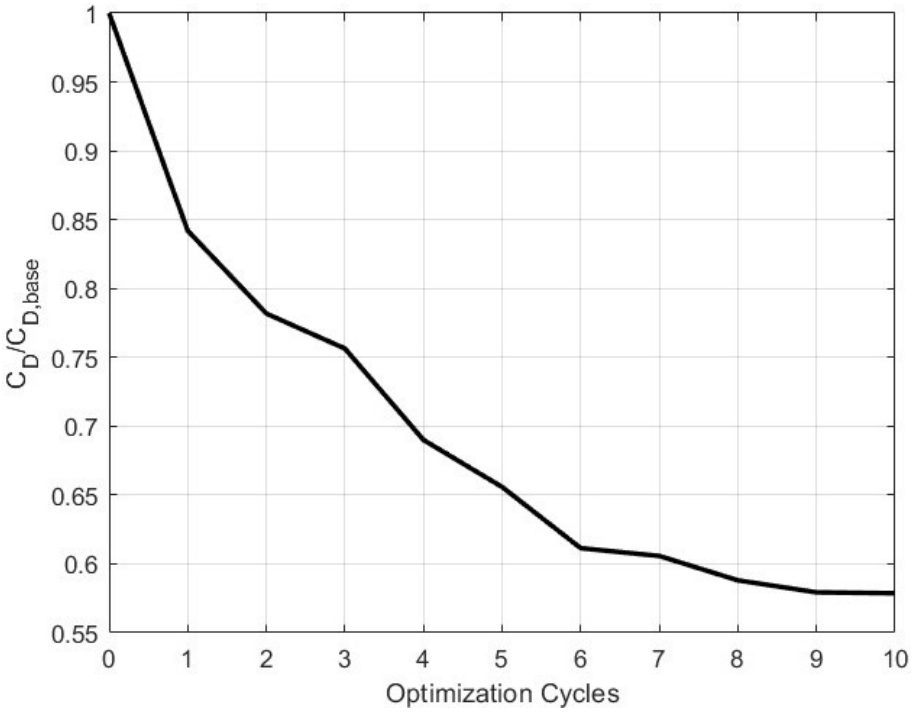

Figure 6.3: *Case A1: Adjoint method convergence history.*

From figure 6.2 it is observed that the optimization tends to displace both sides of the airfoil downwards, while making the suction side slightly flatter and curving the pressure side more. The adjoint method proved very effective and efficient in optimizing the current problem, since in only 10 optimization cycles the drag

decreased by a big percentage (more than 40%). Moreover, as displayed in figure 6.3, the drag coefficient value seems to be converging, signifying that the computed parameter value set is either close to the optimal for this problem or converging at a local minimum.

The Mach number field around the optimized airfoil is displayed in figure 6.4. The baseline flow field is the same as the one displayed in figure 5.2. Similarly to the results of case E1 (section 5.6), the optimization pushes the shock wave downstream and seems to diffuse it (more gradual transition from supersonic to subsonic speeds). The boundary layer and wake are thinner, signifying less flow separation and turbulence. Furthermore, a small shock wave forms also on the pressure side, since it is more curved than the baseline's. All in all, the drag is reduced and the pressure recovery and efficiency are improved.

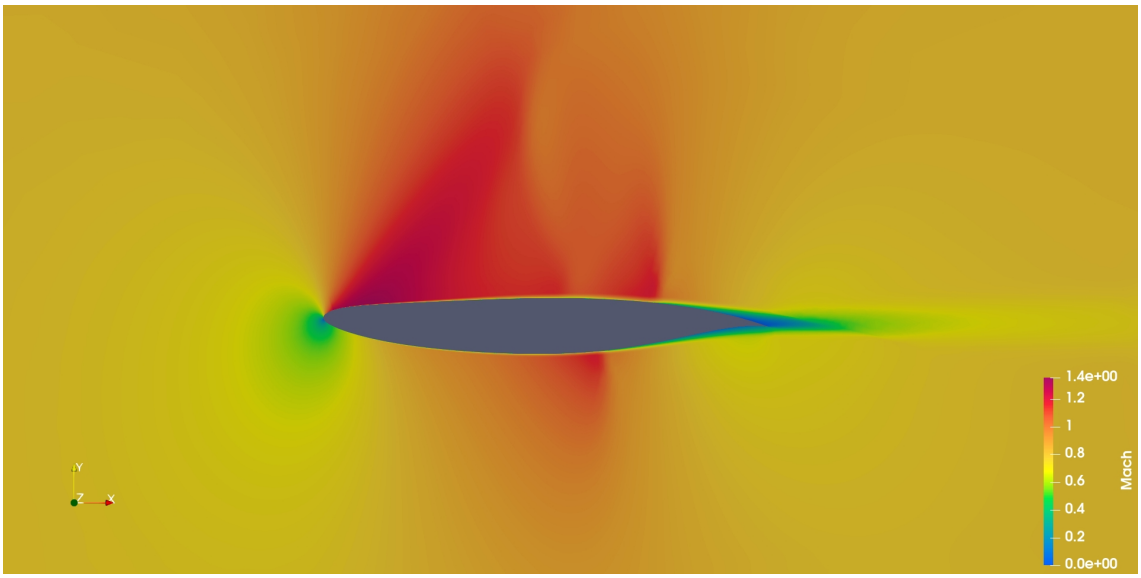

Figure 6.4: *Case A1: Mach number field around optimized airfoil.*

6.3 Case A2

This optimization problem aims to maximize the lift of the deployed flap configuration of the airfoil at takeoff conditions. Its details are displayed in table 6.6.

Case	**Type**	**Objectives**	
A2	SOO	C_D at CR1 **X**	C_L at TO1 ✓
Design Variables:		PARSEC **X**	Flap ✓

Table 6.6: *Case A2 details.*

The airfoil contour is constant, since the PARSEC parameters are not design variables for this case. The two flap parameters are updated in every optimization cycle, hence, they serve as the only design variables of this case. After two optimization cycles, both design variables reached the bounds specified in section 6.1, and the lift coefficient at takeoff increased by 2.44%. The drag coefficient also increased by 6%. The optimized deployed flap configuration of the airfoil is compared to the baseline in figure 6.5 and the convergence history is displayed in figure 6.6. The result proves that the airfoil's lift at takeoff can be increased by increasing the flap's chord length while the airfoil boundary remains constant, as discussed also in the corresponding MAEA optimization case of section 5.6.

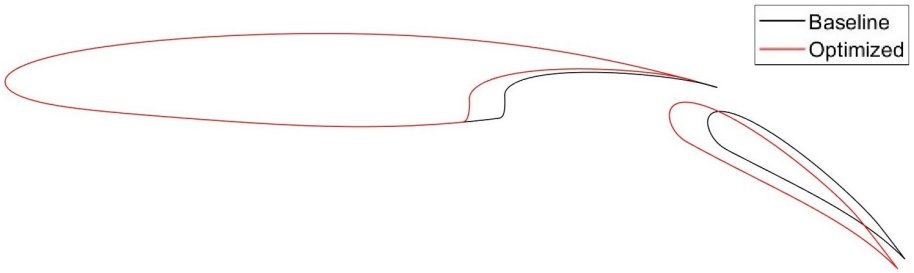

Figure 6.5: *Case A2: Comparison of baseline and optimized two-element airfoils.*

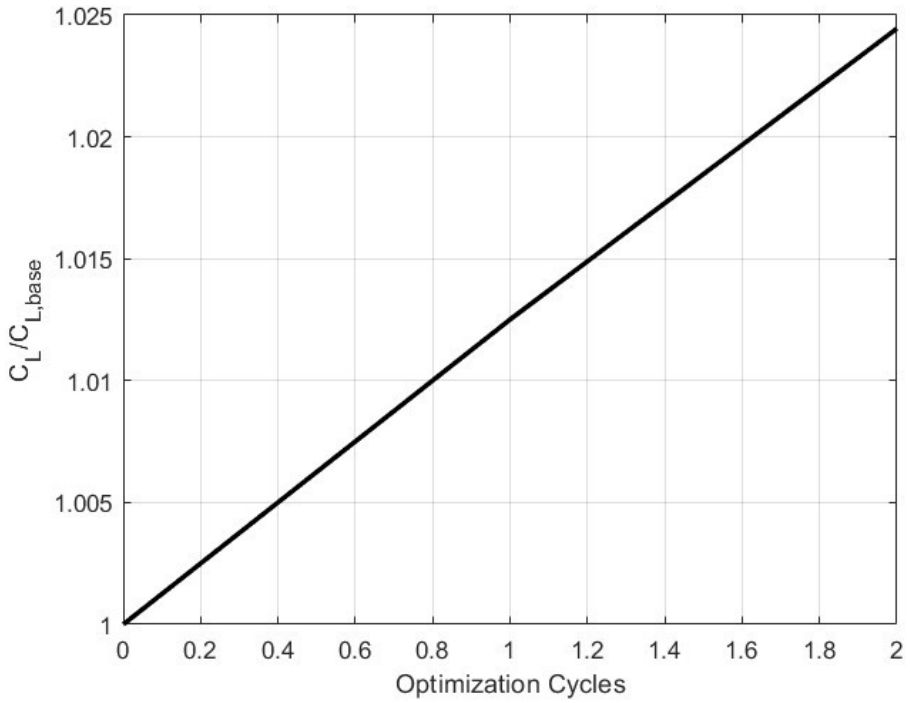

Figure 6.6: *Case A2: Adjoint method convergence history.*

6.4 Case A3

In this case, the objective is, again, the lift coefficient of the airfoil's deployed flap configuration at takeoff. However, contrary to case A2, both the PARSEC and the flap parameters are implemented in the adjoint optimization as design variables, as described in table 6.7.

Case	**Type**	**Objectives**	
A3	SOO	C_D at CR1 **X**	C_L at TO1 ✓
Design Variables:		PARSEC ✓	Flap ✓

Table 6.7: *Case A3 details.*

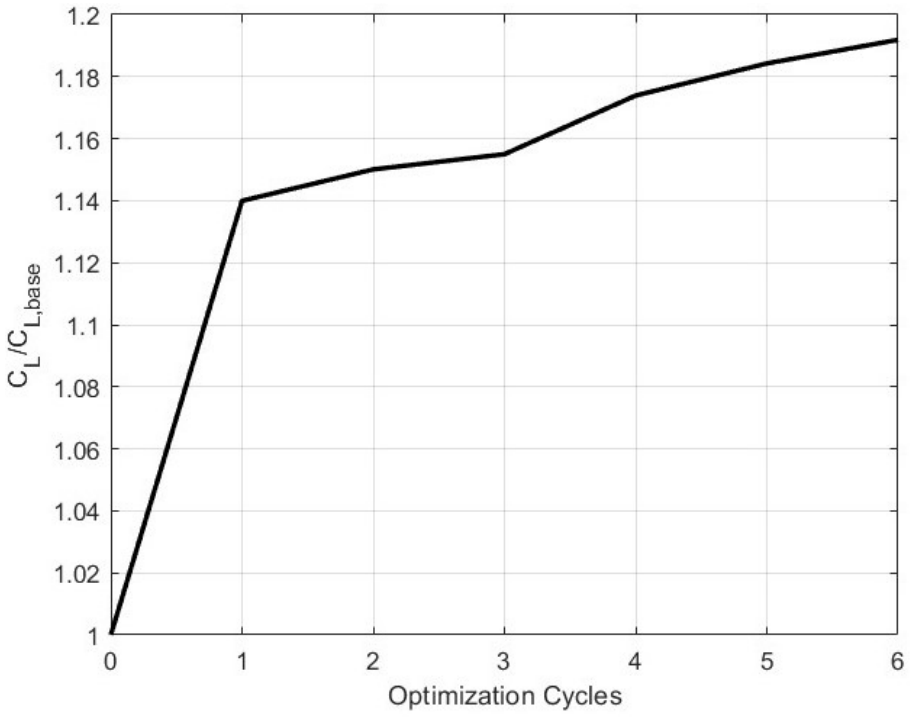

Figure 6.7: *Case A3: Adjoint method convergence history.*

Therefore, in the current problem, the optimization will not only affect the flap but also the airfoil contour, with the aim of maximizing its lift coefficient at takeoff. After 6 cycles, the lift coefficient is increased by 19.2%, and the drag coefficient shows a 2.4% increase. Naturally, the optimization in case A3 produces a much higher increase in takeoff lift coefficient than that of case A2 (19.2% in comparison with 2.44%). That is expected, as more design variables are implemented, and the optimization has much more freedom in affecting the airfoil shape. The convergence

history of the optimization is presented in figure 6.7. The optimized and baseline airfoils in both configurations are compared in figures 6.8 and 6.9.

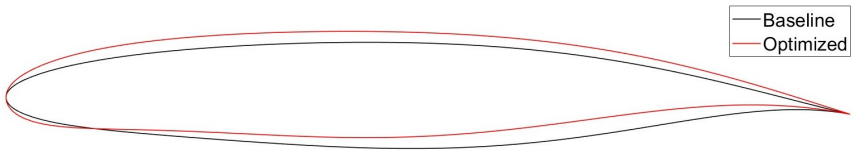

Figure 6.8: *Case A3: Comparison of baseline and optimized airfoils.*

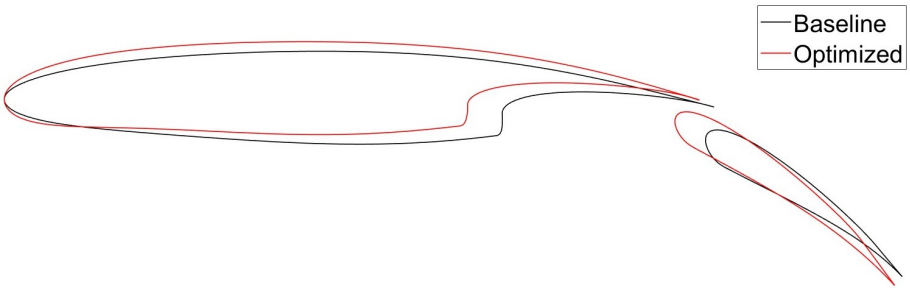

Figure 6.9: *Case A3: Comparison of baseline and optimized two-element airfoils.*

As observed from figures 6.8 and 6.9, the optimization tends to displace both sides of the airfoil upwards, the pressure side is flatter near the LE, and the TE seems sharper. Furthermore, the optimization tends to minimize the gap between the main body and flap, and to increase the thickness of the airfoil. It should be noted that the leading edge radius design variable r_{LE} was not allowed to exceed the value of 0.02, to keep the area of the airfoil close to the baseline.

Figure 6.10: *Case A3: Mach number field around optimized airfoil.*

The Mach number field of the optimized airfoil in the deployed flap configuration is plotted in figure 6.10. In comparison with the baseline Mach field of figure 5.3, not many differences are noticeable. The flow seems to be decelerated on the pressure side and accelerated on the suction side, since the first is flatter and the latter is more curved.

6.5 Case A4

In this case, both the drag coefficient of the airfoil at cruise and the lift coefficient of its deployed flap configuration at takeoff are optimized, as explained in table 6.8.

Case	**Type**	**Objectives**	
A4	MOO	C_D at CR1 ✓	C_L at TO1 ✓
Design Variables:		PARSEC ✓	Flap ✓

Table 6.8: *Case A4 details.*

As described in section 4.2, MOO problems can be optimized with the use of the adjoint method by setting the weighted sum of the objectives as an overall objective function and solving the problem as a SOO case. Naturally, only one solution is calculated in each run. Nevertheless, a front of non-dominated solutions can be produced by solving the SOO problem for multiple weight values. For this case, specifically, the following objective function is implemented:

$$F = w\frac{C_{D,cruise}}{C_{D,cruise,base}} + (1-w)\frac{C_{L,takeoff}}{C_{L,takeoff,base}} \tag{6.3}$$

where w refers to the weight parameter. If w is equal to 1, then this case becomes a SOO case with the drag at cruise as the objective and coincides with case A1, and if w is equal to 0, it is a SOO case with the takeoff lift as the objective, as in case A3. The objective function of each operating point is scaled with its baseline value in equation 6.3, since the two objectives have values of different orders. Therefore, the sensitivity derivatives can be calculated as

$$\frac{dF}{d\vec{b}} = \frac{w}{C_{D,cruise,base}}\frac{d(C_{D,cruise})}{d\vec{b}} + \frac{(1-w)}{C_{L,takeoff,base}}\frac{d(C_{L,takeoff})}{d\vec{b}} \tag{6.4}$$

In every optimization cycle, in order to calculate the sensitivity derivatives of equation 6.4, the primal and adjoint problems are solved for each operating point and their sensitivity derivatives are computed as described in section 4.3 for the cruise

and in section 4.4 for the takeoff OP, respectively. The problem is solved for multiple weight values and the front of figure 6.11 is produced.

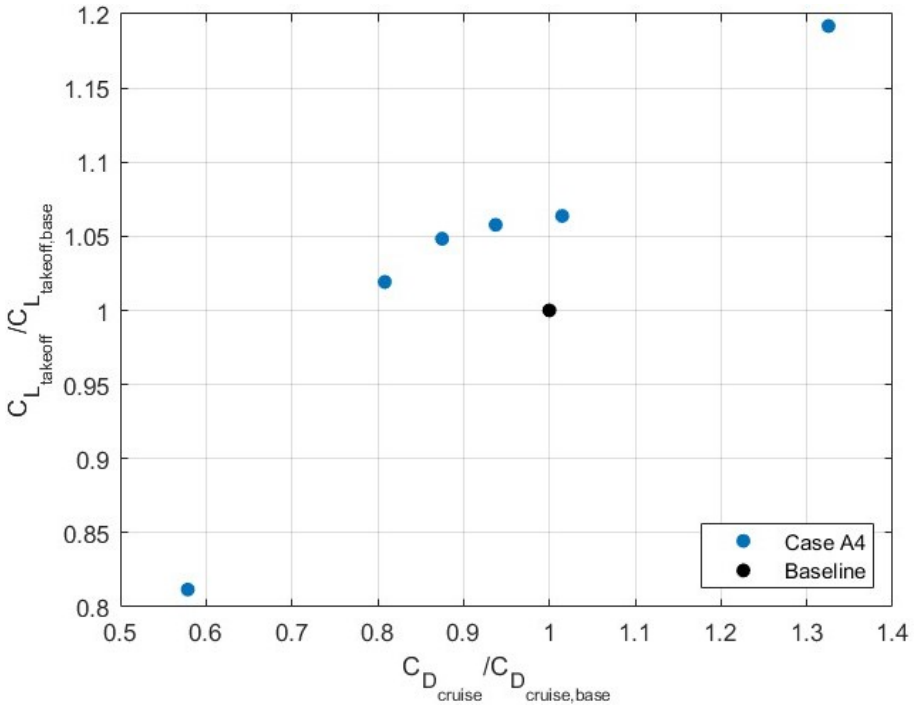

Figure 6.11: *Case A4: Front of non-dominated solutions.*

The endpoint members of the front of figure 6.11 are the solutions calculated from the A1 and A3 SOO cases. As displayed on the front, three solutions dominating the baseline are calculated. Out of the three, the one with the highest lift has a 6.3% decrease in drag at cruise and a 5.8% increase in lift at takeoff. This solution's airfoil contour is compared to the baseline in figure 6.12, and the main body and flap geometries are compared to the baseline in figure 6.13. The adjoint optimization proved effective in calculating solutions dominating the baseline. However, multiple runs are needed to build a front of nondominated solutions.

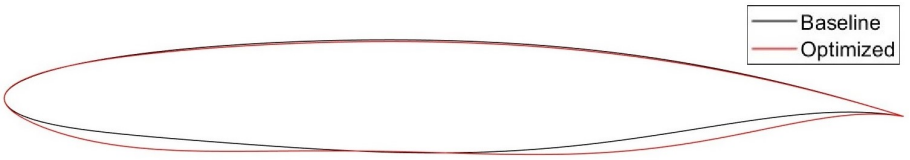

Figure 6.12: *Case A4: Comparison of the baseline and optimized airfoils.*

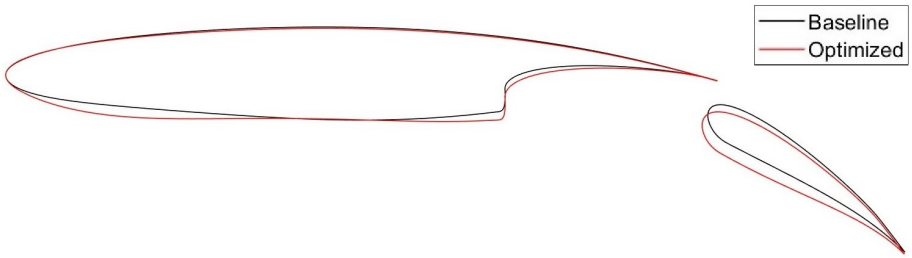

Figure 6.13: *Case A4: Comparison of the baseline and optimized two-element airfoils.*

6.6 Adjoint Optimization Conclusions

The effectiveness of the adjoint optimization method in aerodynamic ShpO cases, such as those of sections 6.2, 6.3, 6.4 and 6.5, is tested in this chapter. The method optimized the airfoil boundary and flap with the aim of minimizing the drag at cruise and/or maximizing the lift at takeoff. Each case's objective was optimized in only a handful of optimization cycles, showcasing the greatest benefit of deterministic methods, namely the ability to quickly converge towards optimal solutions in the design space. Moreover, since the adjoint method is utilized, only 2 CFD evaluations are required in each optimization cycle (one for the primal and one for the adjoint problem), whereas if another gradient-based method was applied, 2b CFD evaluations would be necessary per cycle (where b is equal to the number of design variables). Thus, the optimization cases of this chapter highlight the fact that the adjoint method can be extremely useful in aerodynamic ShpO cases, as it greatly reduces the required CFD evaluations, which are computationally expensive.

Furthermore, through the adjoint-based cases, the process of computing the sensitivity derivatives w.r.t. the design variables (sections 4.3 and 4.4) is validated as each case's objectives are successfully optimized. Specifically, in case A1 (section 6.2) the optimization decreased the drag coefficient at cruise by 42.1% by altering the airfoil's geometry. Similarly, in cases A2 (section 6.3) and A3 (section 6.4) the airfoil's lift at takeoff is increased by 2.4% and 19.2%, respectively, with only the flap being optimized in case A2, while in case A3 both the airfoil's boundary and flap are affected. Finally, in the MOO case A4 (section 6.5), multiple optimization runs are executed and a front of non-dominated solutions is produced (figure 6.11). This front displays a variety of calculated solutions, with three even dominating the baseline parameterization.

In conclusion, the adjoint optimization method proves to be a powerful tool for the aerodynamic ShpO of a two-element airfoil, as indicated by the cases studied in this chapter. It addresses the greatest challenge of aerodynamic ShpO, the need for many computationally demanding CFD simulations, by minimizing the flow solver calls and quickly converging to optimal solutions. Hence, it efficiently produces quality

results in highly complex problems. The only real downsides of this method are the possibility of getting trapped in local optima or overshooting better solutions (both are affected by the step size), which can easily happen in CFD problems where small perturbations to the parameterization can lead to large variations in aerodynamic performance.

Chapter 7

Conclusions

This diploma thesis presented a systematic process of optimizing the shape of an airfoil, in both a typical and a deployed flap configuration, with its main aerodynamic performance metrics as objectives. It also expands the degree of freedom that the optimization is given by implementing some of the flap's geometry parameters as design variables. The proposed process utilizes a method of generating the two-element airfoil geometry that can be applied to any given airfoil and creates realistic main body and flap contours. Furthermore, with the integration of the PARSEC parameterization method as input for the geometry generation, the whole process is easily applicable to ShpO studies with any optimization method (either stochastic or deterministic), as proven by the test cases of this thesis.

Stochastic optimization methods are very useful in aerodynamic ShpO studies since they handle complex design spaces and nonlinear governing equations well. The main disadvantage of these methods is the large number of expensive CFD evaluations required. Therefore, the MAEA method is utilized, which greatly reduces the cost of the optimization. In this diploma thesis, several test cases using MAEAs are examined, with varying objectives, design variables, constraints and conditions, so that observations and comparisons can be made.

Firstly, through case E1 (section 5.2) it is verified that the proposed process in combination with a MAEA can minimize the drag coefficient of an airfoil in cruise configuration, while also not reducing the lift coefficient (with the use of a constraint) and maintaining a trimmed airfoil. Specifically, the drag was reduced by 34% and the lift was increased by 1.8%. This is an important finding, as reducing the drag coefficient of the airfoil during cruise would increase the aircraft's efficiency, thus, increasing its range. Moreover, the area of the airfoil is not affected as its value is constrained in all of the MAEA cases.

Case E4 (section 5.6) introduces the flap design variables, which can be altered with

the aim of maximizing a two-element airfoil's lift coefficient at takeoff. Even though the airfoil shape is kept constant, the lift at takeoff is increased by 4.9% and drag shows an 11.6% increase. During takeoff, the lift coefficient plays a pivotal role as it must have a sufficiently large value at low speeds. Consequently, aircraft deploy trailing edge flaps to increase their lift, and this study shows that this performance metric can be maximized with the ShpO of the flap. The increase in drag is usually not desirable during takeoff, whereas during landing it would help decelerate the aircraft without stalling.

The two aforementioned optimization cases establish the fact that the utilized parameterization can improve a two-element airfoil's lift and drag at both takeoff and cruise. Case E5 (section 5.7) is the most extensive MAEA test case of this thesis, as it implements all design variables and constraints in a MOO case with the purpose of maximizing the lift at takeoff and minimizing the drag at cruise. The front of non-dominated solutions that is computed displays a wide variety of solutions, with many of them dominating the baseline airfoil. It is, therefore, proven that by optimizing the shape of the airfoil and flap, both of the determined aerodynamic performance metrics (lift at takeoff and drag at cruise) can be enhanced greatly. Overall, MAEAs are a very suitable optimization method for the type of studies that this thesis examines, as they effectively search the design space and comply with any constraints that each problem is subject to.

Although technological advances and parallel computing aid stochastic optimization methods, such as MAEAs, by reducing the computational cost, in aerodynamic ShpO studies where CFD evaluations are very demanding, an optimization with these methods requires a significant amount of time until convergence. Thus, deterministic optimization is also utilized, in particular the adjoint method. Initially, in order to apply adjoint-based optimization, the process of generating the geometry for each airfoil configuration is differentiated. This is done as the derivatives of the objective function w.r.t. airfoil coordinates, which are computed from the solution of the adjoint problem in each optimization cycle, must be transformed to derivatives w.r.t. design variables or sensitivity derivatives. Having developed a process of automatically computing sensitivity derivatives, adjoint optimization can be applied for a two-element airfoil with the same objectives as those specified in the MAEA test cases.

Case A1 (section 6.2) is the equivalent of case E1, as it minimizes the drag coefficient of the airfoil at cruise, with the difference being the lack of a constraint for the lift coefficient. The optimized airfoil has a 42.1% and 6.2% decrease in drag and lift coefficients, respectively. The result is computed in 10 optimization cycles which amount to 20 solver calls, in comparison with the 500 CFD evaluations of case E1. The comparison of these two cases showcases the advantage of the adjoint method in reducing computational cost, but also indicates the importance of the ability of MAEAs to easily handle constraints.

In case A3 (section 6.4), both the airfoil boundary and the flap are optimized with

the lift at takeoff as the objective. The optimized airfoil increases the lift by 19.2%, which is the highest increase in takeoff lift out of all cases, and the drag by only 2.4% in 6 optimization cycles. This result signifies that with the implementation of all design variables in the adjoint method, the takeoff lift of a two-element airfoil can be greatly enhanced with very low computational cost.

Finally, case A4 (section 6.5) is the only MOO test case studied with the adjoint method in this thesis. After executing multiple runs of this case with different weight values (since it is solved as a SOO case with the objective function equal to the weighted sum of each objective) a front of non-dominated solutions is computed. However, not many solutions are present in the front, as it is not easy to find non-dominated solutions, due to the fact that even slight modifications to the airfoil contour can result in substantial variations in aerodynamic performance. Still, three solutions dominating the baseline airfoil are computed.

Some of the solutions computed in this thesis' optimization cases are displayed in figure 7.1. Generally, the results of each case are not comparable to those from another, as different sets of constraints, design variables and conditions are implemented. Nevertheless, out of all these solutions, if one had to be adopted (while making the hypothesis that the two objectives are equally important, thus the proposed solution should dominate the baseline), then the member of case E2b's front (figure 5.10), which is highlighted in figure 7.1, with 2% increase in takeoff lift and 17% decrease in drag at cruise should be chosen. It is noted that the fronts of other cases showcase solutions dominating the baseline with better performance metrics than the proposed one from case E2b, as observed in figure 7.1. However, case E2b complies with constraints concerning the lift and moment coefficients of the airfoil at cruise and, hence, it is preferable. Both configurations of the airfoil corresponding to the adopted solution are compared to the baseline ones in figures 7.2 and 7.3.

In conclusion, both optimization methods demonstrated distinct strengths and weaknesses in the aerodynamic ShpO of a two-element airfoil. If only one of the objectives is implemented (SOO) then the adjoint method seems to produce better results with a much lower computational cost. Conversely, in MOO cases, the MAEA method explored the design space more effectively, producing well rounded fronts of non-dominated solutions in each case, with every member complying with all constraints. A natural next step in the continuation of this diploma thesis' findings would be the combination of the two aforementioned optimization methods, aiming to leverage their respective advantages. Indeed, it is common practice in recent years to combine deterministic and stochastic methods (hybrid method). The MAEA could compute multiple possible solutions in every area of the design space and then the adjoint method could refine each solution at a low computational cost, thus, incorporating both methods' strengths. In summary, the process of parameterizing and generating the required geometry, applying CFD to evaluate its aerodynamic performance and optimizing its shape and flap, that is presented in this diploma thesis, is proven to be a powerful tool for any aerodynamic ShpO study regarding two-element airfoils.

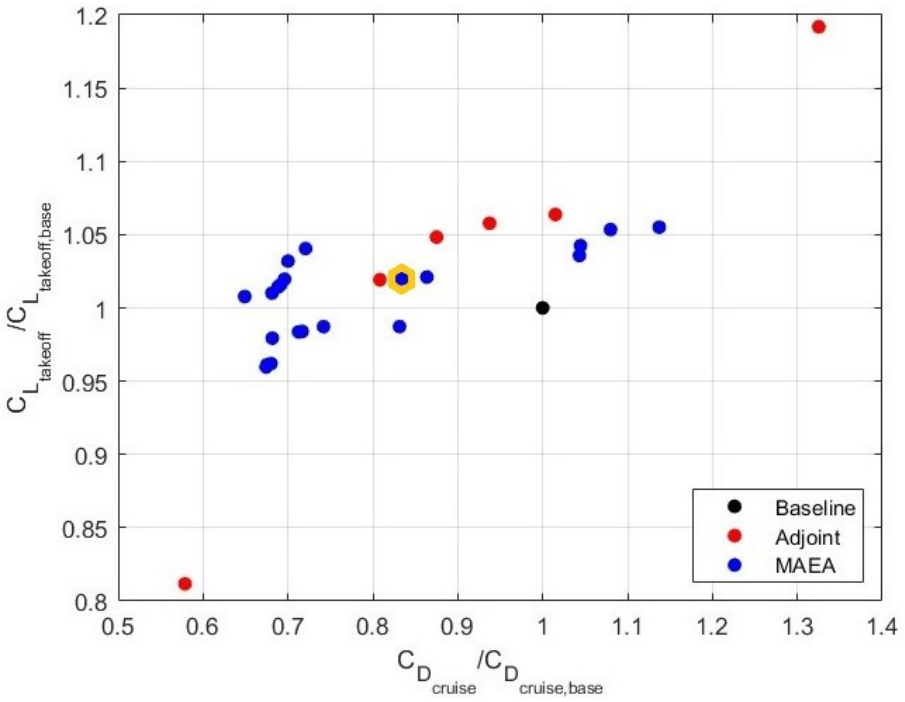

Figure 7.1: *Computed solutions with the use of MAEAs or the adjoint method.*

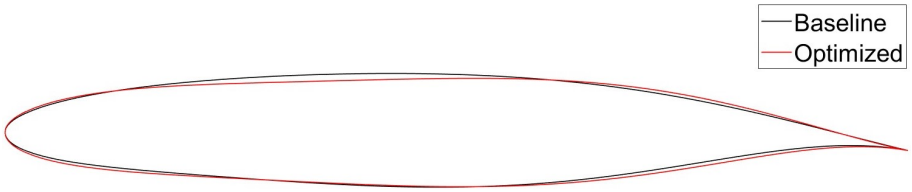

Figure 7.2: *Airfoil corresponding to the proposed solution in comparison with the baseline, in undeployed flap configuration.*

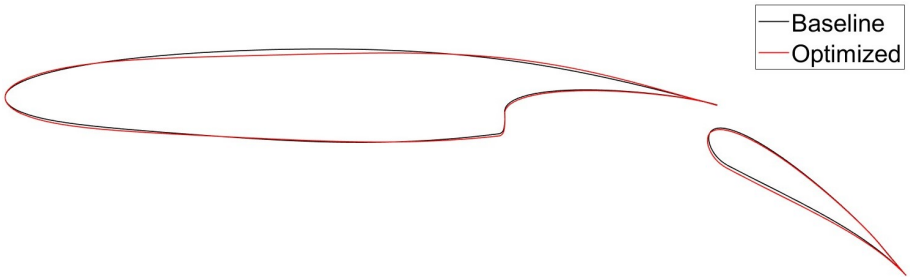

Figure 7.3: *Airfoil corresponding to the proposed solution in comparison with the baseline, in deployed flap configuration.*

Appendices

A Analytical Differentiation of Main Body and Flap's Bezier Curves w.r.t. Airfoil Nodal Coordinates

As explained in section 4.4.1, in order to calculate the sensitivity derivatives of the objective function w.r.t. the PARSEC design variables, the partial derivative of the main body and flap's nodes w.r.t. the airfoil nodes $\partial X'/\partial X$ must be computed and then implemented in the chain rule of equation 4.11. This derivative matrix, which is symbolically represented in figure 4.3, contains parts of identity matrices, but also Bézier nodes which are differentiated as stated in equation 4.14.

Therefore, with the purpose of differentiating the Bézier curve nodes of the main body and flap, their control points' derivatives must first be calculated, and then applied to equation 4.14. The current appendix describes the process of differentiating the control points of the Bézier curves of the created geometries w.r.t. the airfoil nodes in detail. The main body and flap geometries consist of nodes of the initial airfoil and four Bézier curves numbered 5, 6, 7 and 8 as displayed in figure 4.2, with curve 6 being a selection of curve 8 nodes , and, thus, having the exact same derivatives. For Bézier curves 5, 7 and 8 the differentiation process is explained in the following subsections.

A.1 Differentiation of Bézier Curve 8

The first control point of Bézier curve 8 has the following coordinates:

$$x_{CP,0} = x_{suction,cut} \tag{1}$$

$$y_{CP,0} = y_{suction,cut} \tag{2}$$

The x coordinate $x_{CP,0}$ is equal to the first flap design variable, and the y coordinate $y_{CP,0}$ depends on $x_{CP,0}$ and the PARSEC design variables directly ($\partial\vec{y'}/\partial\vec{b}_{par}$ term in equation 4.16), hence, both derivatives w.r.t. the airfoil nodes are equal to zero. The second control point has the following coordinates:

$$x_{CP,1} = x_{suction,cut} - \varepsilon_1 \tag{3}$$

$$y_{CP,1} = \frac{dy}{dx}_{suction} (x_{CP,1} - x_{suction,cut}) + y_{suction,cut} \tag{4}$$

The x coordinate $x_{CP,1}$ is not dependent on airfoil nodes. However, the y coordinate $y_{CP,1}$ implements the airfoil boundary's gradient at the cutting point $dy/dx_{suction}$, which is calculated with the use of the closest nodes to the cutting point, as explained in the following equation:

$$\frac{dy}{dx}_{suction} = \frac{y_{suction,i-1} - y_{suction,i+1}}{h_1 + h_2} \tag{5}$$

where node i is the closest node to the cutting point of the suction side, and h_1 and h_2 are the x coordinate differences calculated by the following equations:

$$h_1 = x_{suction,i-1} - x_{suction,cut} \tag{6}$$

$$h_2 = x_{suction,cut} - x_{suction,i+1} \tag{7}$$

Therefore, $dy/dx_{suction}$ is differentiated as described in the following equations:

$$\frac{\partial(dy/dx_{suction})}{\partial x_{suction,i-1}} = -\frac{y_{suction,i-1} - y_{suction,i+1}}{(h_1 + h_2)^2} \frac{\partial h_1}{\partial x_{suction,i-1}} \tag{8}$$

$$\frac{\partial(dy/dx_{suction})}{\partial x_{suction,i+1}} = -\frac{y_{suction,i-1} - y_{suction,i+1}}{(h_1 + h_2)^2} \frac{\partial h_2}{\partial x_{suction,i+1}} \tag{9}$$

$$\frac{\partial(dy/dx_{suction})}{\partial y_{suction,i-1}} = \frac{1}{h_1 + h_2} \tag{10}$$

$$\frac{\partial(dy/dx_{suction})}{\partial y_{suction,i+1}} = -\frac{1}{h_1 + h_2} \tag{11}$$

Equations 8 through 11 are then applied to calculate the corresponding derivatives of $y_{CP,1}$ from equation 4. The third control point's coordinates are those below:

$$x_{CP,2} = x_{suction,cut} - \varepsilon_2 \tag{12}$$

$$y_{CP,2} = \frac{K_{suction} \frac{N}{N-1} \left((x_{suction,cut} - x_{CP,1})^2 + (y_{suction,cut} - y_{CP,1})^2 \right)^{3/2}}{x_{CP,1} - x_{suction,cut}} + \frac{-x_{suction,cut} \cdot y_{CP,1} + x_{CP,1} \cdot y_{suction,cut} - x_{CP,2} \cdot y_{suction,cut} + x_{CP,2} \cdot y_{CP,1}}{x_{CP,1} - x_{suction,cut}} \tag{13}$$

The x coordinate of this control point is not dependent on the airfoil's nodes, but the y coordinate includes both the gradient $dy/dx_{suction}$ and the curvature $K_{suction}$ of the

airfoil's boundary at the cutting point on the suction side, and, thus, is dependent on the aforementioned nodes of the airfoil boundary. The curvature and second derivative of the airfoil boundary at the suction side cutting poins are calculated as

$$K_{suction} = \frac{|d^2y/dx^2_{suction}|}{(1 + dy/dx_{suction}{}^2)^{3/2}} \tag{14}$$

$$\frac{d^2y}{dx^2}_{suction} = \frac{2}{h_1 + h_2}\left(\frac{h_2 y_{suction,i-1} - (h_1 + h_2)y_{suction,cut} + h_1 y_{suction,i+1}}{h_1 h_2}\right) \tag{15}$$

The second derivative of equation 15 is differentiated as follows:

$$\frac{\partial\,(d^2y/dx^2_{suction})}{\partial x_{suction,i-1}} = \frac{2}{(h_1^2h_2 + h_1h_2^2)^2}\left[\left(-\frac{\partial h_1}{\partial x_{suction,i-1}}y_{suction,cut} + \frac{\partial h_1}{\partial x_{suction,i-1}}\cdot y_{suction,i+1}\right)(h_1^2h_2 + h_1h_2^2) - (h_2y_{suction,i-1} - (h_1 + h_2)y_{suction,cut} + h_1y_{suction,i+1})\cdot \left(2h_1h_2\cdot\frac{\partial h_1}{\partial x_{suction,i-1}} + h_2^2\cdot\frac{\partial h_1}{\partial x_{suction,i-1}}\right)\right] \tag{16}$$

$$\frac{\partial\,(d^2y/dx^2_{suction})}{\partial x_{suction,i+1}} = \frac{2}{(h_1^2h_2 + h_1h_2^2)^2}\left[\left(-\frac{\partial h_2}{\partial x_{suction,i+1}}y_{suction,cut} + \frac{\partial h_2}{\partial x_{suction,i+1}}\cdot y_{suction,i-1}\right)(h_1^2h_2 + h_1h_2^2) - (h_2y_{suction,i-1} - (h_1 + h_2)y_{suction,cut} + h_1y_{suction,i+1})\cdot \left(h_1^2\cdot\frac{\partial h_2}{\partial x_{suction,i+1}} + 2h_1h_2\cdot\frac{\partial h_2}{\partial x_{suction,i+1}}\right)\right] \tag{17}$$

$$\frac{\partial(d^2y/dx^2_{suction})}{\partial y_{suction,i-1}} = \frac{2}{h_1(h_1 + h_2)} \tag{18}$$

$$\frac{\partial(d^2y/dx^2_{suction})}{\partial y_{suction,i+1}} = \frac{2}{h_2(h_1 + h_2)} \tag{19}$$

Implementing equations 16 through 19 and equation 14, the curvature can be differentiated as stated below:

$$\frac{\partial K_{suction}}{\partial X} = \frac{1}{(1 + dy/dx_{suction}{}^2)^3}\left[sign\left(\frac{d^2y}{dx^2}_{suction}\right)\frac{\partial(d^2y/dx^2_{suction})}{\partial X}\cdot \left(1 + \frac{dy}{dx}_{suction}{}^2\right)^{3/2} - 3\left|\frac{d^2y}{dx^2}_{suction}\right|\left(1 + \frac{dy}{dx}_{suction}{}^2\right)^{1/2}\frac{dy}{dx}_{suction}\frac{\partial(dy/dx_{suction})}{\partial X}\right] \tag{20}$$

In equation 20, X denotes the coordinates of the airfoil boundary's nodes which affect the curvature at the cutting point. The derivative of the third control point's y coordinate is calculated, applying the derivatives of the first and second derivatives and curvature of the airfoil boundary, by differentiating equation 77 w.r.t. the nodes it is dependent on. The last (seventh) control point's coordinates are the following:

$$x_{CP,N} = x_{pressure,cut} \tag{21}$$

$$y_{CP,N} = y_{pressure,cut} \tag{22}$$

The x coordinate of equation 21 is equal to the cutting point's on the pressure side of the airfoil, and is calculated by the difference of the flap design variables, as described in equation 3.5. Both coordinates of the last control point are, hence, not dependent on any airfoil nodes. The second to last control point has the following coordinates:

$$x_{CP,N-1} = x_{pressure,cut} - \varepsilon_1 \tag{23}$$

$$y_{CP,N-1} = \frac{dy}{dx}_{pressure}(x_{CP,N-1} - x_{pressure,cut}) + y_{pressure,cut} \tag{24}$$

In equation 24 $dy/dx_{pressure}$ denotes the gradient of the airfoil boundary at the cutting point of the pressure side, and is dependent on the next and previous nodes of the closest node to the cutting point. Corresponding to the process followed for the suction side, the gradient is differentiated as follows:

$$\frac{dy}{dx}_{pressure} = \frac{y_{pressure,j+1} - y_{pressure,j-1}}{h_1 + h_2} \tag{25}$$

$$h_1 = x_{pressure,j+1} - x_{pressure,cut} \tag{26}$$

$$h_2 = x_{pressure,cut} - x_{pressure,j-1} \tag{27}$$

$$\frac{\partial(dy/dx_{pressure})}{\partial x_{pressure,j+1}} = -\frac{y_{pressure,j+1} - y_{pressure,j-1}}{(h_1 + h_2)^2}\frac{\partial h_1}{\partial x_{pressure,j+1}} \tag{28}$$

$$\frac{\partial(dy/dx_{pressure})}{\partial x_{pressure,j-1}} = -\frac{y_{pressure,j+1} - y_{pressure,j-1}}{(h_1 + h_2)^2}\frac{\partial h_2}{\partial x_{pressure,j-1}} \tag{29}$$

$$\frac{\partial(dy/dx_{pressure})}{\partial y_{pressure,j+1}} = \frac{1}{h_1 + h_2} \tag{30}$$

$$\frac{\partial(dy/dx_{pressure})}{\partial y_{pressure,j-1}} = -\frac{1}{h_1 + h_2} \tag{31}$$

The j symbol represents the airfoil node closest to the cutting point of the pressure side. Equations 25 to 31 are implemented and $y_{CP,N-1}$ is differentiated from equation

24. The coordinates of the third to last control point are calculated as follows:

$$x_{CP,N-2} = x_{pressure,cut} - \varepsilon_2 \tag{32}$$

$$\begin{aligned} y_{CP,N-2} = & \frac{K_{pressure}\frac{N}{N-1}\left((x_{pressure,cut} - x_{CP,N-1})^2 + (y_{pressure,cut} - y_{CP,N-1})^2\right)^{3/2}}{x_{CP,1} - x_{pressure,cut}} \\ & + \frac{-x_{pressure,cut} \cdot y_{CP,N-1} + x_{CP,N-1} \cdot y_{pressure,cut}}{x_{CP,N-1} - x_{pressure,cut}} \\ & + \frac{-x_{CP,N-2} \cdot y_{pressure,cut} + x_{CP,N-2} \cdot y_{CP,N-1}}{x_{CP,N-1} - x_{pressure,cut}} \end{aligned} \tag{33}$$

The x coordinate is not dependent on any airfoil nodes, and the y coordinate contains the curvature and gradient of the airfoil's boundary which are dependent on the closest nodes to the cutting point. As was applied for the suction side, for the differentiation of equation 33 the following expressions are utilized:

$$K_{pressure} = \frac{|d^2y/dx^2_{pressure}|}{(1 + dy/dx_{pressure}{}^2)^{3/2}} \tag{34}$$

$$\frac{d^2y}{dx^2}_{pressure} = \frac{2}{h_1 + h_2}\left(\frac{h_2 y_{pressure,j+1} - (h_1 + h_2)y_{pressure,cut} + h_1 y_{pressure,j-1}}{h_1 h_2}\right) \tag{35}$$

$$\begin{aligned} \frac{\partial\left(d^2y/dx^2_{pressure}\right)}{\partial x_{pressure,j+1}} = & \frac{2}{(h_1^2 h_2 + h_1 h_2^2)^2}\Bigg[\Bigg(-\frac{\partial h_1}{\partial x_{pressure,j+1}} y_{pressure,cut} + \frac{\partial h_1}{\partial x_{pressure,j+1}} \cdot \\ & y_{pressure,j-1}\Bigg)(h_1^2 h_2 + h_1 h_2^2) - (h_2 y_{pressure,j+1} - (h_1 + h_2)y_{pressure,cut} + h_1 y_{pressure,j-1}) \cdot \\ & \left(2h_1 h_2 \cdot \frac{\partial h_1}{\partial x_{pressure,j+1}} + h_2^2 \cdot \frac{\partial h_1}{\partial x_{pressure,j+1}}\right)\Bigg] \end{aligned} \tag{36}$$

$$\begin{aligned} \frac{\partial\left(d^2y/dx^2_{pressure}\right)}{\partial x_{pressure,j-1}} = & \frac{2}{(h_1^2 h_2 + h_1 h_2^2)^2}\Bigg[\Bigg(-\frac{\partial h_2}{\partial x_{pressure,j-1}} y_{pressure,cut} + \frac{\partial h_2}{\partial x_{pressure,j-1}} \cdot \\ & y_{pressure,j+1}\Bigg)(h_1^2 h_2 + h_1 h_2^2) - (h_2 y_{pressure,j+1} - (h_1 + h_2)y_{pressure,cut} + h_1 y_{pressure,j-1}) \cdot \\ & \left(h_1^2 \cdot \frac{\partial h_2}{\partial x_{pressure,j-1}} + 2h_1 h_2 \cdot \frac{\partial h_2}{\partial x_{pressure,j-1}}\right)\Bigg] \end{aligned} \tag{37}$$

$$\frac{\partial(d^2y/dx^2_{pressure})}{\partial y_{pressure,j+1}} = \frac{2}{h_1(h_1+h_2)} \tag{38}$$

$$\frac{\partial(d^2y/dx^2_{pressure})}{\partial y_{pressure,j-1}} = \frac{2}{h_2(h_1+h_2)} \tag{39}$$

$$\frac{\partial K_{pressure}}{\partial X} = \frac{1}{(1+dy/dx_{pressure}{}^2)^3}\left[sign\left(\frac{d^2y}{dx^2}_{pressure}\right)\frac{\partial(d^2y/dx^2_{pressure})}{\partial X}\cdot\right.$$
$$\left.\left(1+\frac{dy}{dx}{}^2_{pressure}\right)^{3/2} - 3\left|\frac{d^2y}{dx^2}_{pressure}\right|\left(1+\frac{dy}{dx}{}^2_{pressure}\right)^{1/2}\frac{dy}{dx}_{pressure}\frac{\partial(dy/dx_{pressure})}{\partial X}\right] \tag{40}$$

Implementing equations 34 through 40 the derivatives of $y_{CP,N-2}$ are computed. The coordinates of the fourth control point are the following:

$$x_{CP,3} = x_{CP,N-2} - \varepsilon_3 \tag{41}$$

$$y_{CP,3} = \frac{y_{CP,2} + y_{CP,N-2}}{2} + \varepsilon_4 \tag{42}$$

Therefore, the derivatives of this control point's coordinates w.r.t. the airfoil nodes' coordinates are calculated by the following equations:

$$\frac{\partial x_{CP,3}}{\partial X} = \frac{\partial x_{CP,N-2}}{\partial X} \tag{43}$$

$$\frac{\partial y_{CP,3}}{\partial X} = 0.5\left(\frac{\partial y_{CP,2}}{\partial X} + \frac{\partial y_{CP,N-2}}{\partial X}\right) \tag{44}$$

Having calculated all of Bézier curve's 8 control point derivatives w.r.t. the airfoil's nodes, equation 4.14 is applied and the derivatives of the nodes of Bézier 8 are computed. The same derivatives apply also for the nodes of Bézier 6.

A.2 Differentiation of Bézier Curve 5

The first control point of Bézier curve 5 has the following x coordinate:

$$x_{CP,0} = x_{suction,cut} - \varepsilon_5 \tag{45}$$

The y coordinate $y_{CP,0}$ is calculated as a PARSEC node on the suction side of the airfoil with $x = x_{CP,0}$. These two coordinates are dependent on the first flap design

variable and directly on the PARSEC design variables, and, thus, their derivatives w.r.t. the airfoil's nodes are zero. The second and third control point coordinates are the following:

$$x_{CP,1} = x_{CP,0} + \varepsilon_7 \tag{46}$$

$$y_{CP,1} = \frac{dy}{dx}_{suction} (x_{CP,1} - x_{CP,0}) + y_{CP,0} \tag{47}$$

$$x_{CP,2} = x_{CP,0} + \varepsilon_8 \tag{48}$$

$$\begin{aligned} y_{CP,2} = & \frac{K_{suction} \frac{N}{N-1} \left((x_{CP,0} - x_{CP,1})^2 + (y_{CP,0} - y_{CP,1})^2 \right)^{3/2}}{x_{CP,1} - x_{CP,0}} \\ & + \frac{-x_{CP,0} \cdot y_{CP,1} + x_{CP,1} \cdot y_{CP,0} - x_{CP,2} \cdot y_{CP,0} + x_{CP,2} \cdot y_{CP,1}}{x_{CP,1} - x_{CP,0}} \end{aligned} \tag{49}$$

In full accordance with the process implemented for Bézier 8 (A.1), equations 5 through 11 are applied to calculate the derivatives of $y_{CP,1}$, and equations 14 to 20 are used for $y_{CP,2}$. It is noted that in these equations node i now refers to the airfoil node on the suction side closest to $x_{CP,0}$, and $x/y_{suction,cut}$ are replaced by $x/y_{CP,0}$. The derivatives of $x_{CP,1}$ and $x_{CP,2}$ are zero. The last control point's coordinates are the following:

$$x_{CP,N} = x_{suction,cut} \tag{50}$$

$$y_{CP,N} = y_{suction,cut} \tag{51}$$

These coordinates, as explained before, are not dependent on any airfoil nodes and, as a result, their derivatives are zero. The second to last control point coordinates are the following:

$$x_{CP,N-1} = x_{suction,i-1} \tag{52}$$

$$y_{CP,N-1} = y_{suction,i-1} \tag{53}$$

The i symbol denotes the airfoil's boundary node closest to the cutting point on the suction side. Consequently, their derivatives are calculated as follows:

$$\frac{\partial x_{CP,N-1}}{\partial x_{suction,i-1}} = 1 \tag{54}$$

$$\frac{\partial y_{CP,N-1}}{\partial y_{suction,i-1}} = 1 \tag{55}$$

Finally, the fourth control point has the following coordinates:

$$x_{CP,3} = x_{CP,N-1} \tag{56}$$

$$y_{CP,3} = \frac{y_{CP,2} + y_{CP,N-1}}{2} \tag{57}$$

which are differentiated as follows:

$$\frac{\partial x_{CP,3}}{\partial X} = \frac{\partial x_{CP,N-1}}{\partial X} \tag{58}$$

$$\frac{\partial y_{CP,3}}{\partial X} = 0.5\left(\frac{\partial y_{CP,2}}{\partial X} + \frac{\partial y_{CP,N-1}}{\partial X}\right) \tag{59}$$

A.3 Differentiation of Bézier Curve 7

If t_{min} represents the index of Bézier curve's 8 node with the minimum x coordinate, then the first two control point coordinates of Bézier 7 are calculated as follows:

$$x_{CP7,0} = \sum_{i=0}^{N} B_i^N(t_{\min}) x_{CP8,i} = x_{8,tmin} \tag{60}$$

$$y_{CP7,0} = \sum_{i=0}^{N} B_i^N(t_{\min}) y_{CP8,i} = y_{8,tmin} \tag{61}$$

$$x_{CP7,1} = \sum_{i=0}^{N} B_i^N(t_{\min}+1) x_{CP8,i} = x_{8,tmin+1} \tag{62}$$

$$y_{CP7,1} = \sum_{i=0}^{N} B_i^N(t_{\min}+1) y_{CP8,i} = y_{8,tmin+1} \tag{63}$$

It is noted that $x/y_{CP7,\ldots}$ refers to the control point coordinates of Bézier curve 7, so as not to be confused with $x/y_{CP8,i}$ which denote Bézier 8 control points. The derivatives of the nodes of Bézier curve 8 w.r.t. the airfoil nodes are computed in section A.1, and, thus, the derivatives of the first two control points of Bézier 7 can be calculated as follows:

$$\frac{\partial x_{CP7,0}}{\partial X} = \frac{\partial x_{8,tmin}}{\partial X} \tag{64}$$

$$\frac{\partial y_{CP7,0}}{\partial X} = \frac{\partial y_{8,tmin}}{\partial X} \tag{65}$$

$$\frac{\partial x_{CP7,1}}{\partial X} = \frac{\partial x_{8,tmin+1}}{\partial X} \tag{66}$$

$$\frac{\partial y_{CP7,1}}{\partial X} = \frac{\partial y_{8,tmin+1}}{\partial X} \tag{67}$$

The last control point of Bézier curve 7 has the following x coordinate:

$$x_{CP7,N} = x_{8,tmin} - \varepsilon_6 \tag{68}$$

and its y coordinate $y_{CP7,N}$ is calculated as a PARSEC node on the pressure side of the airfoil, as described in the following equation:

$$y_{CP7,N} = \sum_{n=1}^{6} {a_n}^{PS} {x_{CP7,N}}^{n-1/2} = \sum_{n=1}^{6} {a_n}^{PS} (x_{8,tmin} - \varepsilon_6)^{n-1/2} \tag{69}$$

The derivatives of the last control point coordinates are the following:

$$\frac{\partial x_{CP7,N}}{\partial X} = \frac{\partial x_{8,tmin}}{\partial X} \tag{70}$$

$$\frac{\partial y_{CP7,N}}{\partial X} = \sum_{n=1}^{6} {a_n}^{PS} \left(\frac{\partial x_{8,tmin}}{\partial X} \right)^{n-1/2} \tag{71}$$

The second and third to last control point coordinates are calculated as follows:

$$x_{CP,N-1} = x_{CP,N} + \varepsilon_9 \tag{72}$$

$$y_{CP,N-1} = \frac{dy}{dx}_{pressure} (x_{CP,N-1} - x_{CP,N}) + y_{CP,N} \tag{73}$$

$$x_{CP,N-2} = x_{CP,N} + \varepsilon_{10} \tag{74}$$

$$\begin{aligned} y_{CP,N-2} = & \frac{K_{pressure} \frac{N}{N-1} \left((x_{CP,N} - x_{CP,N-1})^2 + (y_{CP,N} - y_{CP,N-1})^2 \right)^{3/2}}{x_{CP,1} - x_{CP,N}} \\ & + \frac{-x_{CP,N} \cdot y_{CP,N-1} + x_{CP,N-1} \cdot y_{CP,N}}{x_{CP,N-1} - x_{CP,N}} \\ & + \frac{-x_{CP,N-2} \cdot y_{CP,N} + x_{CP,N-2} \cdot y_{CP,N-1}}{x_{CP,N-1} - x_{CP,N}} \end{aligned} \tag{75}$$

Fully consistent with the method applied for the pressure side control points of Bézier 8 (A.1), equations 25 to 31 are used to differentiate the second to last control point coordinates, and equations 34 to 40 for the third to last control point. In these equations, the j symbol now refers to the airfoil boundary node closest to $x = x_{CP,N}$, and $x/y_{pressure,cut}$ are replaced by $x/y_{CP,N}$. Lastly, the third control point has the

following coordinates:

$$x_{CP,2} = \frac{x_{CP,1} + x_{CP,N-2}}{2} \tag{76}$$

$$y_{CP,2} = \frac{y_{CP,1} + y_{CP,N-2}}{2} \tag{77}$$

which are differentiated as follows:

$$\frac{\partial x_{CP,2}}{\partial X} = 0.5\left(\frac{\partial x_{CP,1}}{\partial X} + \frac{\partial x_{CP,N_2}}{\partial X}\right) \tag{78}$$

$$\frac{\partial y_{CP,2}}{\partial X} = 0.5\left(\frac{\partial y_{CP,1}}{\partial X} + \frac{\partial y_{CP,N_2}}{\partial X}\right) \tag{79}$$

B Analytical Differentiation of Main Body and Flap's Bezier Curves w.r.t. Flap Design Variables

In section 4.4.2, the process of transforming the derivatives of the objective function w.r.t. the main body and flap's node coordinates to derivatives w.r.t. the flap design variables (3.1.2) is described. The derivative matrix $dX/d\vec{b}_{flap}$ of figure 4.5 must be computed, so as to apply the chain rule of equation 4.12. For the calculation of these derivatives, corresponding to what is stated in appendix A, the control point coordinates of the three Bézier curves must be differentiated w.r.t. the flap design variables and then applied to equation 4.22. In the current appendix, the process of differentiating the Bézier curve control points is described in detail.

B.1 Differentiation of Bézier Curve 8

The first control point's coordinates are the following:

$$x_{CP,0} = x_{suction,cut} \tag{80}$$

$$y_{CP,0} = y_{suction,cut} = \sum_{n=1}^{6} a_n {}^{SS}x_{suction,cut}{}^{n-1/2} \tag{81}$$

The x coordinate of the cutting point of the suction side of the airfoil is the first flap design variable. Therefore, the first control point's coordinates are differentiated as

follows:

$$\frac{\partial x_{CP,0}}{\partial \vec{b}_{flap,1}} = 1 \tag{82}$$

$$\frac{\partial y_{CP,0}}{\partial \vec{b}_{flap,1}} = \sum_{n=1}^{6} {a_n}^{SS}(n-1/2){x_{suction,cut}}^{n-3/2} \tag{83}$$

The derivatives of the above coordinates w.r.t. the second flap design variable are zero. The second control point has the following coordinates:

$$x_{CP,1} = x_{CP,0} - \varepsilon_1 \tag{84}$$

$$y_{CP,1} = \frac{dy}{dx}_{suction}(x_{CP,1} - x_{CP,0}) + y_{CP,0} = -\varepsilon_1 \cdot \frac{dy}{dx}_{suction} + y_{CP,0} \tag{85}$$

The gradient of the airfoil boundary on the suction side at the cutting point is equal to:

$$\frac{dy}{dx}_{suction} = \frac{y_{suction,i-1} - y_{suction,i+1}}{h_1 + h_2} \tag{86}$$

where h_1 and h_2 are equal to:

$$h_1 = x_{suction,i-1} - x_{suction,cut} \tag{87}$$

$$h_2 = x_{suction,cut} - x_{suction,i+1} \tag{88}$$

where i refers to the airfoil node closest to the cutting point of the suction side. Thus, expression 86 becomes:

$$\frac{dy}{dx}_{suction} = \frac{y_{suction,i-1} - y_{suction,i+1}}{x_{suction,i-1} - x_{suction,i+1}} \tag{89}$$

As observed from expression 89, the gradient of the airfoil is not dependent on the flap design variables, hence, its derivative w.r.t. the flap design variables is zero. The second control point's coordinates are differentiated as follows:

$$\frac{\partial x_{CP,1}}{\partial \vec{b}_{flap}} = \frac{\partial x_{CP,0}}{\partial \vec{b}_{flap}} \tag{90}$$

$$\frac{\partial y_{CP,1}}{\partial \vec{b}_{flap}} = \frac{\partial y_{CP,0}}{\partial \vec{b}_{flap}} \tag{91}$$

The third control point has the following coordinates:

$$x_{CP,2} = x_{CP,0} - \varepsilon_2 \tag{92}$$

$$y_{CP,2} = \frac{K_{suction}\frac{N}{N-1}\left((x_{CP,0}-x_{CP,1})^2+(y_{CP,0}-y_{CP,1})^2\right)^{3/2}}{x_{CP,1}-x_{CP,0}} + \frac{-x_{CP,0}\cdot y_{CP,1}+x_{CP,1}\cdot y_{CP,0}-x_{CP,2}\cdot y_{CP,0}+x_{CP,2}\cdot y_{CP,1}}{x_{CP,1}-x_{CP,0}} \tag{93}$$

Implementing equations 84 and 85, expression 129 becomes:

$$y_{CP,2} = \frac{-1}{\varepsilon_1}\left[K_{suction}\frac{N}{N-1}\left({\varepsilon_1}^2\left(1+\frac{dy}{dx}_{suction}^2\right)\right)^{3/2} - x_{CP,0}\cdot y_{CP,1}+x_{CP,1}\cdot y_{CP,0}-x_{CP,2}\cdot y_{CP,0}+x_{CP,2}\cdot y_{CP,1}\right] \tag{94}$$

The curvature of the airfoil's boundary on the suction side at the cutting point $K_{suction}$ is calculated as follows:

$$K_{suction} = \frac{|d^2y/dx^2_{suction}|}{(1+dy/dx_{suction}{}^2)^{3/2}} \tag{95}$$

where $d^2y/dx^2_{suction}$ is the second gradient at the cutting point and is calculated as below:

$$\frac{d^2y}{dx^2}_{suction} = \frac{2}{h_1+h_2}\left(\frac{h_2 y_{suction,i-1}-(h_1+h_2)y_{suction,cut}+h_1 y_{suction,i+1}}{h_1 h_2}\right) \tag{96}$$

The second gradient of equation 96 is differentiated as follows:

$$\frac{\partial\left(d^2y/dx^2_{suction}\right)}{\partial\vec{b}_{flap,1}} = \frac{2}{(h_1^2h_2+h_1h_2^2)^2}\left[\left(\frac{\partial h_2}{\partial\vec{b}_{flap,1}}y_{suction,i-1}-(h_1+h_2)\frac{\partial y_{CP,0}}{\partial b_{flap,1}}+\frac{\partial h_1}{\partial\vec{b}_{flap,1}}y_{suction,i+1}\right)(h_1^2h_2+h_1h_2^2)-\left(h_2y_{suction,i-1}-(h_1+h_2)y_{CP,0}+h_1y_{suction,i+1}\right)\cdot\left(2h_1\frac{\partial h_1}{\partial\vec{b}_{flap,1}}h_2+h_1^2\frac{\partial h_2}{\partial\vec{b}_{flap,1}}+\frac{\partial h_1}{\partial\vec{b}_{flap,1}}h_2^2+2h_1h_2\frac{\partial h_2}{\partial\vec{b}_{flap,1}}\right)\right] \tag{97}$$

The curvature of expression 95 is differentiated by the following equation:

$$\frac{\partial K_{suction}}{\partial \vec{b}_{flap,1}} = \frac{sign(d^2y/dx^2_{suction})\frac{\partial(d^2y/dx^2_{suction})}{\partial \vec{b}_{flap,1}}(1+dy/dx_{suction}{}^2)^{3/2}}{(1+dy/dx_{suction}{}^2)^3} \tag{98}$$

From equations 92 and 94, and with the implementation of equation 98, the derivatives of the third control point's coordinates are calculated. The last control point has the following coordinates:

$$x_{CP,N} = x_{pressure,cut} = \vec{b}_{flap,1} - \vec{b}_{flap,2} \tag{99}$$

$$y_{CP,N} = y_{pressure,cut} = \sum_{n=1}^{6} a_n{}^{PS}(\vec{b}_{flap,1} - \vec{b}_{flap,2})^{n-1/2} \tag{100}$$

These coordinates are differentiated as below:

$$\frac{\partial x_{CP,N}}{\partial \vec{b}_{flap,1}} = 1 = -\frac{\partial x_{CP,N}}{\partial \vec{b}_{flap,2}} \tag{101}$$

$$\frac{\partial y_{CP,N}}{\partial \vec{b}_{flap,1}} = \sum_{n=1}^{6} a_n{}^{PS}(n-1/2)(\vec{b}_{flap,1} - \vec{b}_{flap,2})^{n-3/2} = -\frac{\partial y_{CP,N}}{\partial \vec{b}_{flap,2}} \tag{102}$$

The second to last control point's coordinates are the following:

$$x_{CP,N-1} = x_{CP,N} - \varepsilon_1 \tag{103}$$

$$y_{CP,N-1} = \frac{dy}{dx}_{pressure}(x_{CP,N-1} - x_{CP,N}) + y_{CP,N} = -\varepsilon_1 \cdot \frac{dy}{dx}_{pressure} + y_{CP,N} \tag{104}$$

The gradient at the cutting point of the pressure side is computed from the following expression:

$$\frac{dy}{dx}_{pressure} = \frac{y_{pressure,j+1} - y_{pressure,j-1}}{h_1 + h_2} \tag{105}$$

where h_1 and h_2 are equal to:

$$h_1 = x_{pressure,j+1} - x_{pressure,cut} \tag{106}$$

$$h_2 = x_{pressure,cut} - x_{pressure,j-1} \tag{107}$$

where j denotes the airfoil node closest to the cutting point of the pressure side. Equation 105 now becomes:

$$\frac{dy}{dx}_{pressure} = \frac{y_{pressure,j+1} - y_{pressure,j-1}}{x_{pressure,j+1} - x_{pressure,j-1}} \tag{108}$$

Equation 108 signifies that the gradient of the airfoil at the cutting point is not dependent on the flap design variables. The derivatives of the second to last control point are calculated as follows:

$$\frac{\partial x_{CP,N-1}}{\partial \vec{b}_{flap}} = \frac{\partial x_{CP,N}}{\partial \vec{b}_{flap}} \tag{109}$$

$$\frac{\partial y_{CP,N-1}}{\partial \vec{b}_{flap}} = \frac{\partial y_{CP,N}}{\partial \vec{b}_{flap}} \tag{110}$$

The coordinates of the third to last control point are calculated as follows:

$$x_{CP,N-2} = x_{CP,N} - \varepsilon_2 \tag{111}$$

$$\begin{aligned} y_{CP,N-2} = & \frac{K_{pressure}\frac{N}{N-1}\left((x_{CP,N} - x_{CP,N-1})^2 + (y_{CP,N} - y_{CP,N-1})^2\right)^{3/2}}{x_{CP,1} - x_{CP,N}} \\ & + \frac{-x_{CP,N} \cdot y_{CP,N-1} + x_{CP,N-1} \cdot y_{CP,N} - x_{CP,N-2} \cdot y_{CP,N} + x_{CP,N-2} \cdot y_{CP,N-1}}{x_{CP,N-1} - x_{CP,N}} \end{aligned} \tag{112}$$

After applying equations 103 and 104, expression 112 becomes:

$$\begin{aligned} y_{CP,N-2} = & \frac{-1}{\varepsilon_1}\left[K_{pressure}\frac{N}{N-1}\left({\varepsilon_1}^2\left(1 + \frac{dy}{dx}_{pressure}^2\right)\right)^{3/2}\right. \\ & \left. -x_{CP,N} \cdot y_{CP,N-1} + x_{CP,N-1} \cdot y_{CP,N} - x_{CP,N-2} \cdot y_{CP,N} + x_{CP,N-2} \cdot y_{CP,N-1}\right] \end{aligned} \tag{113}$$

The curvature of the airfoil's boundary at the cutting point of the pressure side is calculated as follows:

$$K_{pressure} = \frac{|d^2y/dx^2_{pressure}|}{(1 + dy/dx_{pressure}{}^2)^{3/2}} \tag{114}$$

and the second derivative of the airfoil boundary is equal to:

$$\frac{d^2y}{dx^2}_{pressure} = \frac{2}{h_1+h_2}\left(\frac{h_2 y_{pressure,j+1} - (h_1+h_2)y_{CP,N} + h_1 y_{pressure,j-1}}{h_1 h_2}\right) \tag{115}$$

The derivative of equation 115 is the following:

$$\begin{aligned}\frac{\partial\left(d^2y/dx^2_{pressure}\right)}{\partial\vec{b}_{flap}} = \frac{2}{(h_1^2h_2+h_1h_2^2)^2}\Bigg[\Bigg(\frac{\partial h_2}{\partial\vec{b}_{flap}}y_{pressure,j+1} - (h_1+h_2)\frac{\partial y_{CP,N}}{\partial b_{flap}} + \\ \frac{\partial h_1}{\partial\vec{b}_{flap}}y_{pressure,j-1}\Bigg)(h_1^2h_2+h_1h_2^2) - \big(h_2 y_{pressure,j+1} - (h_1+h_2)y_{CP,N} + \\ h_1 y_{pressure,j-1}\big)\left(2h_1\frac{\partial h_1}{\partial\vec{b}_{flap}}h_2 + h_1^2\frac{\partial h_2}{\partial\vec{b}_{flap}} + \frac{\partial h_1}{\partial\vec{b}_{flap}}h_2^2 + 2h_1h_2\frac{\partial h_2}{\partial\vec{b}_{flap}}\right)\Bigg]\end{aligned} \tag{116}$$

The curvature is differentiated as follows:

$$\frac{\partial K_{pressure}}{\partial\vec{b}_{flap}} = \frac{sign(d^2y/dx^2_{pressure})\frac{\partial(d^2y/dx^2_{pressure})}{\partial\vec{b}_{flap}}(1+dy/dx_{pressure}{}^2)^{3/2}}{(1+dy/dx_{pressure}{}^2)^3} \tag{117}$$

The derivative of 117 is implemented and the third to last control point of the airfoil is differentiated by equations 111 and 113. Finally, the fourth control point has the following coordinates:

$$x_{CP,3} = x_{CP,N-2} - \varepsilon_3 \tag{118}$$

$$y_{CP,3} = \frac{1}{2}(y_{CP,2} + y_{CP,N-2}) + \varepsilon_4 \tag{119}$$

which are differentiated as follows:

$$\frac{\partial x_{CP,3}}{\partial\vec{b}_{flap}} = \frac{\partial x_{CP,N-2}}{\partial\vec{b}_{flap}} \tag{120}$$

$$\frac{\partial y_{CP,3}}{\partial\vec{b}_{flap}} = \frac{1}{2}\left(\frac{\partial y_{CP,2}}{\partial\vec{b}_{flap}} + \frac{\partial y_{CP,N-2}}{\partial\vec{b}_{flap}}\right) \tag{121}$$

B.2 Differentiation of Bézier Curve 5

The first control point's coordinates are the following:

$$x_{CP,0} = x_{suction,cut} - \varepsilon_5 = \vec{b}_{flap,1} - \varepsilon_5 \tag{122}$$

$$y_{CP,0} = \sum_{n=1}^{6} {a_n}^{SS}(x_{suction,cut} - \varepsilon_5)^{n-1/2} = \sum_{n=1}^{6} {a_n}^{SS}(\vec{b}_{flap,1} - \varepsilon_5)^{n-1/2} \tag{123}$$

These coordinates are differentiated as below:

$$\frac{\partial x_{CP,0}}{\partial \vec{b}_{flap,1}} = 1 \tag{124}$$

$$\frac{\partial y_{CP,0}}{\partial \vec{b}_{flap,1}} = \sum_{n=1}^{6} {a_n}^{SS}(n - 1/2)(\vec{b}_{flap,1} - \varepsilon_5)^{n-3/2} \tag{125}$$

The second and third control points' coordinates are the following:

$$x_{CP,1} = x_{CP,0} + \varepsilon_6 \tag{126}$$

$$y_{CP,1} = \frac{dy}{dx}_{suction}(x_{CP,1} - x_{CP,0}) + y_{CP,0} \tag{127}$$

$$x_{CP,2} = x_{CP,0} + \varepsilon_7 \tag{128}$$

$$\begin{aligned} y_{CP,2} = & \frac{K_{suction}\frac{N}{N-1}\left((x_{CP,0} - x_{CP,1})^2 + (y_{CP,0} - y_{CP,1})^2\right)^{3/2}}{x_{CP,1} - x_{CP,0}} \\ & + \frac{-x_{CP,0} \cdot y_{CP,1} + x_{CP,1} \cdot y_{CP,0} - x_{CP,2} \cdot y_{CP,0} + x_{CP,2} \cdot y_{CP,1}}{x_{CP,1} - x_{CP,0}} \end{aligned} \tag{129}$$

The process of differentiating the coordinates of equations 126 to 129 is the same as the one applied for the suction side control points of Bézier curve 8. Expressions 86 to 91 are utilized for the second control point, and 94 through 98 for the third one. In the aforementioned expressions copied from Bézier 8, the i symbol now represents the node of the suction side of the airfoil closest to $x_{CP,0}$. The last control point has the following coordinates:

$$x_{CP,N} = x_{suction,cut} = \vec{b}_{flap,1} \tag{130}$$

$$y_{CP,N} = \sum_{n=1}^{6} {a_n}^{SS} {x_{suction,cut}}^{n-1/2} = \sum_{n=1}^{6} {a_n}^{SS} \vec{b}_{flap,1}^{n-1/2} \tag{131}$$

which are differentiated as below:

$$\frac{\partial x_{CP,N}}{\partial \vec{b}_{flap,1}} = 1 \tag{132}$$

$$\frac{\partial y_{CP,N}}{\partial \vec{b}_{flap,1}} = \sum_{n=1}^{6} {a_n}^{SS}(n-1/2)\vec{b}_{flap,1}^{n-3/2} \tag{133}$$

The second to last control point has the coordinates of the following equations, which are not dependent on the flap design variables, since they are equal to the coordinates of a node of the airfoil boundary.

$$x_{CP,N-1} = x_{suction,i-1} \tag{134}$$

$$y_{CP,N-1} = y_{suction,i-1} \tag{135}$$

Lastly, the fourth control point has the following coordinates:

$$x_{CP,3} = x_{CP,N-1} \tag{136}$$

$$y_{CP,3} = \frac{y_{CP,2} + y_{CP,N-1}}{2} \tag{137}$$

which are differentiated as follows:

$$\frac{\partial x_{CP,3}}{\partial \vec{b}_{flap}} = \frac{\partial x_{CP,N-1}}{\partial \vec{b}_{flap}} \tag{138}$$

$$\frac{\partial y_{CP,3}}{\partial \vec{b}_{flap}} = 0.5\left(\frac{\partial y_{CP,2}}{\partial \vec{b}_{flap}} + \frac{\partial y_{CP,N-1}}{\partial \vec{b}_{flap}}\right) \tag{139}$$

B.3 Differentiation of Bézier Curve 7

The first two control points of Bézier curve 7 are the node of Bézier curve 8 with the minimum x coordinate value and the next one. Therefore, if t_{min} denotes the index of Bézier curve's 8 node with minimum x, then the first two control point's coordinates of Bézier 7 are written as follows:

$$x_{CP7,0} = \sum_{i=0}^{N} B_i^N(t_{\min}) x_{CP8,i} = x_{8,tmin} \tag{140}$$

$$y_{CP7,0} = \sum_{i=0}^{N} B_i^N(t_{\min}) y_{CP8,i} = y_{8,tmin} \tag{141}$$

$$x_{CP7,1} = \sum_{i=0}^{N} B_i^N(t_{\min}+1) x_{CP8,i} = x_{8,tmin+1} \tag{142}$$

$$y_{CP7,1} = \sum_{i=0}^{N} B_i^N(t_{\min}+1) y_{CP8,i} = y_{8,tmin+1} \tag{143}$$

The coordinates of Bézier curve's 8 nodes are differentiated w.r.t. the flap design variables in section B.1, hence, the first two control points' derivatives of Bézier 7 can be calculated as follows:

$$\frac{\partial x_{CP7,0}}{\partial \vec{b}_{flap}} = \frac{\partial x_{8,tmin}}{\partial \vec{b}_{flap}} \tag{144}$$

$$\frac{\partial y_{CP7,0}}{\partial \vec{b}_{flap}} = \frac{\partial y_{8,tmin}}{\partial \vec{b}_{flap}} \tag{145}$$

$$\frac{\partial x_{CP7,1}}{\partial \vec{b}_{flap}} = \frac{\partial x_{8,tmin+1}}{\partial \vec{b}_{flap}} \tag{146}$$

$$\frac{\partial y_{CP7,1}}{\partial \vec{b}_{flap}} = \frac{\partial y_{8,tmin+1}}{\partial \vec{b}_{flap}} \tag{147}$$

The last control point's coordinates for Bézier curve 7 are calculated as below:

$$x_{CP7,N} = x_{8,tmin} - \varepsilon_8 \tag{148}$$

$$y_{CP7,N} = \sum_{n=1}^{6} {a_n}^{PS} {x_{CP7,N}}^{n-1/2} = \sum_{n=1}^{6} {a_n}^{PS} (x_{8,tmin} - \varepsilon_8)^{n-1/2} \tag{149}$$

and they are differentiated as follows:

$$\frac{\partial x_{CP7,N}}{\partial \vec{b}_{flap}} = \frac{\partial x_{8,tmin}}{\partial \vec{b}_{flap}} \tag{150}$$

$$\frac{\partial y_{CP7,N}}{\partial \vec{b}_{flap}} = \sum_{n=1}^{6} {a_n}^{PS} \left(\frac{\partial x_{8,tmin}}{\partial \vec{b}_{flap}} \right)^{n-1/2} \tag{151}$$

The second and third to last control point coordinates are the following:

$$x_{CP,N-1} = x_{CP,N} + \varepsilon_9 \tag{152}$$

$$y_{CP,N-1} = \frac{dy}{dx}_{pressure} (x_{CP,N-1} - x_{CP,N}) + y_{CP,N} \tag{153}$$

$$x_{CP,N-2} = x_{CP,N} + \varepsilon_{10} \tag{154}$$

$$y_{CP,N-2} = \frac{K_{pressure}\frac{N}{N-1}\left((x_{CP,N} - x_{CP,N-1})^2 + (y_{CP,N} - y_{CP,N-1})^2\right)^{3/2}}{x_{CP,1} - x_{CP,N}} + \frac{-x_{CP,N} \cdot y_{CP,N-1} + x_{CP,N-1} \cdot y_{CP,N}}{x_{CP,N-1} - x_{CP,N}} + \frac{-x_{CP,N-2} \cdot y_{CP,N} + x_{CP,N-2} \cdot y_{CP,N-1}}{x_{CP,N-1} - x_{CP,N}} \tag{155}$$

In order to differentiate these coordinates, steps 105 to 110 are followed for the second to last control point, and 113 to 117 for the third to last. Finally, the third control point has the following coordinates:

$$x_{CP,2} = \frac{x_{CP,1} + x_{CP,N-2}}{2} \tag{156}$$

$$y_{CP,2} = \frac{y_{CP,1} + y_{CP,N-2}}{2} \tag{157}$$

which are differentiated as follows:

$$\frac{\partial x_{CP,2}}{\partial \vec{b}_{flap}} = 0.5\left(\frac{\partial x_{CP,1}}{\partial \vec{b}_{flap}} + \frac{\partial x_{CP,N_2}}{\partial \vec{b}_{flap}}\right) \tag{158}$$

$$\frac{\partial y_{CP,2}}{\partial \vec{b}_{flap}} = 0.5\left(\frac{\partial y_{CP,1}}{\partial \vec{b}_{flap}} + \frac{\partial y_{CP,N_2}}{\partial \vec{b}_{flap}}\right) \tag{159}$$

Bibliography

[1] CFD land - mesh types in CFD: A comprehensive guide (2025), https://cfdland.com/mesh-types-in-cfd-a-comprehensive-guide/, accessed: 2025-05-02

[2] Bäck, T., Fogel, D.B., Michalewicz, Z.: Handbook of Evolutionary Computation (1st ed.). CRC Press (1997). https://doi.org/10.1201/9780367802486

[3] Belda, M., Hyhlík, T.: Interactive airfoil optimization using parsec parametrization and adjoint method. Applied Sciences **14**(8) (2024). https://doi.org/10.3390/app14083495, https://www.mdpi.com/2076-3417/14/8/3495

[4] Choi, J.W., Curry, R.E., Elkaim, G.H.: Continuous curvature path generation based on bézier curves for autonomous vehicles. IAENG International Journal of Applied Mathematics **40**(1), 61–73 (2010)

[5] Coello Coello, C.A.: Theoretical and numerical constraint-handling techniques used with evolutionary algorithms: a survey of the state of the art. Computer Methods in Applied Mechanics and Engineering **191**(11), 1245–1287 (2002). https://doi.org/https://doi.org/10.1016/S0045-7825(01)00323-1, https://www.sciencedirect.com/science/article/pii/S0045782501003231

[6] Deb, K.: Multi-Objective Optimization Using Evolutionary Algorithms. Wiley (2001)

[7] Dwight, R.P.: Efficient sensitivity analysis for aerodynamic optimization using an adjoint formulation. AIAA Journal **44**(11), 2513–2519 (2006). https://doi.org/10.2514/1.17455

[8] Federal Aviation Administration: Pilot's Handbook of Aeronautical Knowledge. U.S. Department of Transportation (2023), https://www.faa.gov/regulations_policies/handbooks_manuals/aviation/phak, fAA-H-8083-25C

[9] Giles, M.B., Pierce, N.A.: An introduction to the adjoint approach to design. Flow, Turbulence and Combustion **65**, 393–415 (2000). https://doi.org/10.1023/A:1011430410075

[10] Jameson, A.: Aerodynamic Design via Control Theory, Lecture Notes in Computer Science, vol. 145. Springer (1988)

[11] Kampolis, I.C., Giannakoglou, K.C.: Distributed Evolutionary Algorithms with Hierarchical Evaluation. Engineering Optimization **41**(11), 1037–1049 (2009)

[12] Kapsoulis, D.H., Tsiakas, K.T., Trompoukis, X.S., Asouti, V.G., Giannakoglou, K.C.: Evolutionary multi-objective optimization assisted by metamodels, kernel PCA and multi-criteria decision making techniques with applications in aerodynamics. Applied Soft Computing **64**, 1–13 (2018)

[13] Karakasis, M., Giannakoglou, K.C.: On the Use of Metamodel-Assisted Multi-Objective Evolutionary Algorithms. Engineering Optimization **38**(8), 941–957 (2006)

[14] Kenway, G., Martins, J.R.R.A.: Multipoint high-fidelity aerostructural optimization of a transport aircraft configuration. Journal of Aircraft **51**(1), 144–160 (2014). https://doi.org/10.2514/1.C032150

[15] Kontou, M.G.: The Continuous Adjoint Method with Consistent Discretization Schemes for Transitional Flows and the Use of Deep Neural Networks in Shape Optimization in Fluid Mechanics. PhD thesis, National Technical University of Athens, Athens (2023)

[16] Lee, K.D., Eyi, S.: Aerodynamic shape optimization based on high-level physics. In: Proceedings of the 20th International Congress of the Aeronautical Sciences (ICAS). University of Illinois, Urbana, Illinois, U.S.A. (1996), iCAS-96-2.7.3

[17] Lian, Y., Oyama, A., Liou, M.S.: Progress in design optimization using evolutionary algorithms for aerodynamic problems. Progress in Aerospace Sciences **46**(5), 199–223 (2010). https://doi.org/https://doi.org/10.1016/j.paerosci.2009.08.003, https://www.sciencedirect.com/science/article/pii/S0376042109000323

[18] Martins, J.R.: Aerodynamic design optimization: Challenges and perspectives. Computers & Fluids **239**, 105391 (2022). https://doi.org/https://doi.org/10.1016/j.compfluid.2022.105391, https://www.sciencedirect.com/science/article/pii/S0045793022000615

[19] Salunke, N.P., Ahamad, R.J., Channiwala, S.: Airfoil parameterization techniques: A review. American Journal of Mechanical Engineering **2**(4), 99–102 (2014)

[20] Sasaki, D., Obayashi, S., Nakahashi, K.: Navier-stokes optimization of supersonic wings with four objectives using evolutionary algorithm. Journal of Aircraft **39**(4), 621–629 (2002). https://doi.org/10.2514/2.2974

[21] Secco, N., Kenway, G., He, P., Mader, C., Martins, J.: Efficient mesh generation and deformation for aerodynamic shape optimization. AIAA Journal **59**, 2020 (10 2020). https://doi.org/10.2514/1.J059491

[22] Shunshun, W., Zheng, G.: Design, optimization and application of two-element airfoils for tactical uav. Advances in Mechanical Engineering **14**(11), 1–14 (2022), https://doi.org/10.1177/16878132221137027

[23] Skinner, S., Zare-Behtash, H.: State-of-the-art in aerodynamic shape optimisation methods. Applied Soft Computing **62**, 933–962 (2018). https://doi.org/https://doi.org/10.1016/j.asoc.2017.09.030, https://www.sciencedirect.com/science/article/pii/S1568494617305690

[24] Sobieczky, H.: Parametric airfoils and wings. Notes on Numerical Fluid Mechanics **68**, 71–88 (1998)

[25] Veldman, A. E. P. & Rinzema, K.: Playing with nonuniform grids. Journal of Engineering Mathematics **26**(1), 119–130 (1992)

[26] Yondo, R., Bobrowski, K., Andres, E., Valero, E.: A review of surrogate modeling techniques for aerodynamic analysis and optimization: Current limitations and future challenges in industry. Computational Methods in Applied Sciences pp. 19–33 (01 2019). https://doi.org/10.1007/978-3-319-89988-6-2

[27] Zhou, Z.H., Zhang, J.Q., Jin, Y.: Combining global and local surrogate models to accelerate evolutionary optimization. IEEE Transactions on Systems, Man, and Cybernetics, Part C (Applications and Reviews) **41**(6), 982–994 (2011)

[28] Κ.Χ. Γιαννάκογλου: Μέθοδοι Βελτιστοποίησης στην Αεροδυναμική. ΕΜΠ Σχολή Μηχανολόγων Μηχανικών (2004)

[29] Κ.Χ. Γιαννάκογλου: Συνεκτικές Ροές στις Στροβιλομηχανές. ΕΜΠ Τμήμα Μηχανολόγων Μηχανικών, Τομέας Ρευστών, Εργαστήριο Θερμικών Στροβιλομηχανών (2004)

[30] Κ.Χ. Γιαννάκογλου και Ι. Αναγνωστόπουλος και Γ. Μπεργελές: Αριθμητική Ανάλυση για Μηχανικούς. ΕΜΠ Τμήμα Μηχανολόγων Μηχανικών (2003)

Εθνικό Μετσόβιο Πολυτεχνείο
Σχολή Μηχανολόγων Μηχανικών
Τομέας Ρευστών
Μονάδα Παράλληλης Υπολογιστικής Ρευστοδυναμικής
& Βελτιστοποίησης

Παραμετροποίηση Αεροτομών δύο Στοιχείων και Ένταξη στην Αεροδυναμική Βελτιστοποίηση Μορφής

Διπλωματική Εργασία
(Εκτεταμένη Περίληψη στην Ελληνική Γλώσσα)

Γεώργιος Γρηγόριος Κλαυδιανός

Επιβλέποντες:
Κυριάκος Χ. Γιαννάκογλου, Καθηγητής ΕΜΠ
Δρ. Β. Ασούτη, Εντεταλμένη Διδάσκουσα ΕΜΠ

Αθήνα, 2025

Περιεχόμενα

Κεφάλαιο 1

Εισαγωγή

Η αεροδυναμική βελτιστοποίηση μορφής (ΒΜ) αποτελεί τη διαδικασία τροποποίησης της γεωμετρίας ενός αεροδυναμικού σώματος με σκοπό τη βελτίωση αεροδυναμικών δεικτών απόδοσης, όπως οι συντελεστές άνωσης, αντίστασης ή ροπής και η κατανομή πίεσης. Αυτό επιτυγχάνεται συνήθως συνδυάζοντας την υπολογιστική ρευστομηχανική (ΥΡΔ) με αλγόριθμους βελτιστοποίησης, προκειμένου να προσδιοριστεί η πλέον κατάλληλη λύση. Μέσω της βελτιστοποίησης, ένα πρόβλημα το οποίο μπορεί να περιλαμβάνει μεγάλο αριθμό μεταβλητών σχεδιασμού, προκαθορισμένους στόχους και περιορισμούς, επιλύεται με σκοπό την εύρεση μιας λύσης η οποία υπερτερεί επαρκώς, ως προς τους αεροδυναμικούς δείκτες, έναντι της αρχικής διαμόρφωσης. Το ερευνητικό πεδίο αυτό αφορά ένα ευρύ φάσμα εφαρμογών, όπως είναι η αεροδιαστημική, η αυτοκινητοβιομηχανία, οι ανεμογεννήτριες κ.ά. [8, 10].

Η διπλωματική αυτή εργασία επικεντρώνεται στην ανάπτυξη μίας συστηματικής διαδικασίας βελτιστοποίησης της γεωμετρίας μίας αεροτομής δύο στοιχείων σε δύο διακριτές διαμορφώσεις, μία τυπική και μία με εκτεταμένη υπεραντωτική διάταξη στην ακμή εκφυγής (flap). Για τον σκοπό αυτόν, ενσωματώνονται δύο διαφορετικές μέθοδοι βελτιστοποίησης, οι εξελικτικοί αλγόριθμοι υποβοηθούμενοι από μεταμοντέλα (MAEA) και η συνεχής συζυγής (continuous adjoint) μέθοδος. Οι δοκιμαστικές μελέτες που εξετάζονται στοχεύουν στη βελτίωση των κυριότερων αεροδυναμικών δεικτών απόδοσης μίας αεροτομής, συγκεκριμένα της αντίστασης κατά την οριζόντια πτήση και της άνωσης κατά την απογείωση. Μολονότι η προαναφερθείσα διαδικασία δοκιμάζεται σε μία συγκεκριμένη αεροτομή, μπορεί εύκολα να εφαρμοστεί σε κάθε είδους μελετώμενη γεωμετρία αεροτομής. Η δυνατότητα της αναπτυχθείσας συστηματικής προσέγγισης της παραμετροποίησης, δημιουργίας της γεωμετρίας και αξιολόγησης με ΥΡΔ να ενσωματωθεί σε βρόχο ΒΜ, επικυρώνεται μέσω των δοκιμαστικών μελετών της διπλωματικής εργασίας.

Κεφάλαιο 2

Δημιουργία και Παραμετροποίηση Αεροτομής δύο Στοιχείων

2.1 Δημιουργία Γεωμετρίας

Για τη δημιουργία της γεωμετρίας μίας αεροτομής δύο στοιχείων, δηλαδή κύριο σώμα και υπεραντωτική διάταξη τύπου Fowler στην ακμή εκφυγής (flap) [2], αναπτύσσεται ένα λογισμικό, το οποίο δέχεται ως είσοδο τις κομβικές συντεταγμένες της εξεταζόμενης αεροτομής. Στις μελέτες της διπλωματικής εργασίας χρησιμοποιείται μία αεροτομή από εφαρμογή της ΜΠΥΡ&Β/ΕΜΠ, η οποία παρουσιάζεται στο σχήμα 2.1.

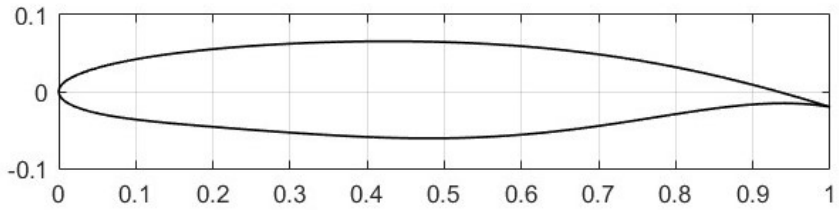

Σχήμα 2.1: *Εξεταζόμενη αεροτομή.*

Η διαδικασία δημιουργίας της προαναφερθείσας γεωμετρίας περιγράφεται συνοπτικά ως εξής:

1. Η γεωμετρία του flap παράγεται διατηρώντας κάποιους από τους κόμβους της αεροτομής κοντά στην ακμή εκφυγής και σχεδιάζοντας μία καμπύλη Bézier για την περιοχή της ακμής πρόσπτωσης του.

2. Το κύριο σώμα της αεροτομής δύο στοιχείων δημιουργείται με χρήση κάποιων από τους υπόλοπους κόμβους της αεροτομής, τους περισσότερους από τους κόμβους της Bézier του flap και δύο επιπρόσθετες καμπύλες Bézier για να σχηματιστεί η ακμή πρόσπτωσης στην πλευρά υποπίεσης και ένα ράδιο στην πλευρά υπερπίεσης.

3. Για τη διαμόρφωση με εκτεταμένο flap, το περίγραμμα του μετατοπίζεται και περιστρέφεται καταλλήλως.

Η διαδικασία αυτή εξασφαλίζει ότι όταν το flap δεν είναι εκτεταμένο, εφάπτεται απολύτως στην περιοχή σχισμής (slot) του κύριου σώματος χωρίς σημεία τομής. Οι καμπύλες Bézier που σχεδιάζονται με τα σημεία ελέγχου τους για το flap και το κύριο σώμα απεικονίζονται στα σχήματα 2.2 και 2.3, αντίστοιχα, ενώ η προκύπτουσα γεωμετρία αεροτομής δύο στοιχείων παρουσιάζεται στο σχήμα 2.4.

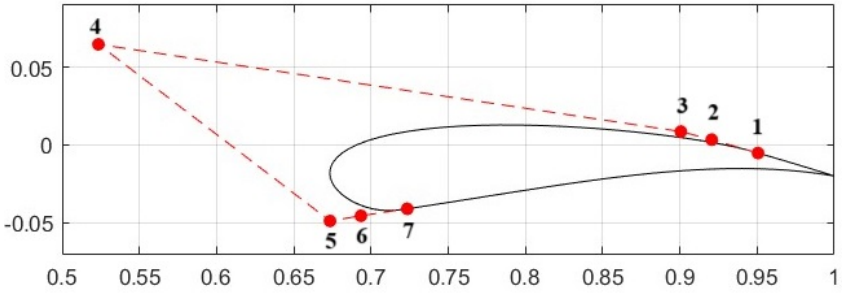

Σχήμα 2.2: *Καμπύλη Bézier ακμής πρόσπτωσης του flap.*

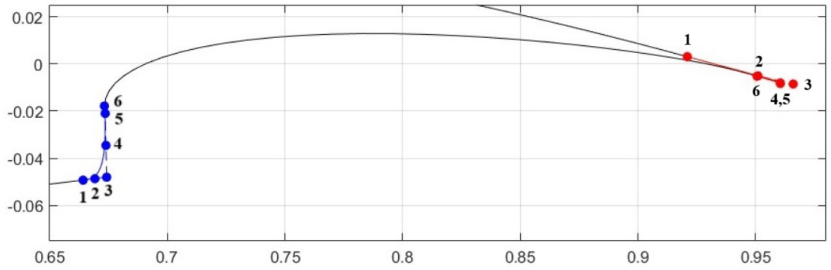

Σχήμα 2.3: *Καμπύλες Bézier κυρίου σώματος.*

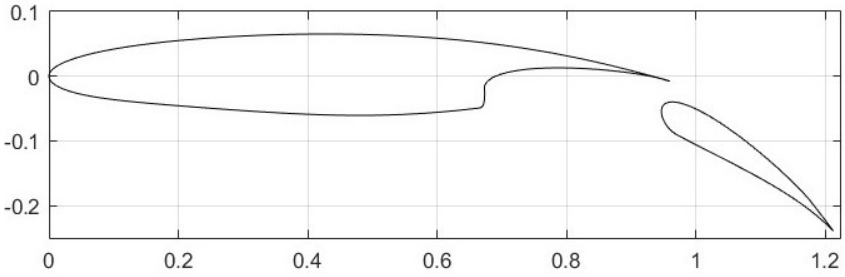

Σχήμα 2.4: *Αεροτομή δύο στοιχείων με εκτεταμένο flap.*

2.2 Παραμετροποίηση Αεροτομής και Υπεραντωτικής Διάταξης

Όπως προαναφέρθηκε, η διαδικασία δημιουργίας της γεωμετρίας αεροτομής δύο στοιχείων δέχεται ως είσοδο τις συντεταγμένες της εξεταζόμενης αεροτομής. Καθώς η διαδικασία αυτή προορίζεται να χρησιμοποιηθεί για ΒΜ της αεροτομής, πρέπει να εφαρμοστεί μία ρητή αριθμητική μέθοδος ανανέωσης των κομβικών συντεταγμένων της αεροτομής σε κάθε κύκλο βελτιστοποίησης. Επομένως, η αεροτομή πρέπει να παραμετροποιηθεί με μία μέθοδο που χρησιμοποιεί έναν μικρό αριθμό παραμέτρων για να ορίσει το περίγραμμα της, αλλά ταυτόχρονα είναι αποτελεσματική στον έλεγχο των σημαντικών αεροδυναμικών χαρακτηριστικών και δημιουργεί ρεαλιστικά σχήματα αεροτομών. Η μέθοδος που επιλέγεται ονομάζεται PARSEC και κάνει χρήση των 11 παραμέτρων του σχήματος 2.5, οι οποίες αποτελούν γεωμετρικά στοιχεία της αεροτομής, για να δημιουργήσει την αεροτομή [11, 9]. Μέσω των 11 παραμέτρων υπολογίζονται 6 σταθερές για κάθε πλευρά της αεροτομής (a_n) και ορίζεται ένα πολυώνυμο για την y συντεταγμένη των κόμβων της αεροτομής συναρτήσει των x, ως εξής

$$y = \sum_{n=1}^{6} a_n x^{n-1/2} \tag{2.1}$$

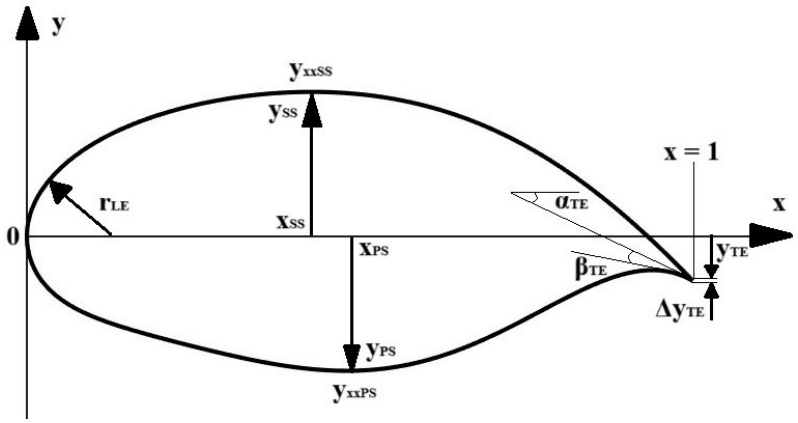

Σχήμα 2.5: *Μέθοδος PARSEC για παραμετροποίηση αεροτομών.*

Επιπρόσθετα, για να υπάρχει η δυνατότητα τροποποίησης όχι μόνο της μορφής της αεροτομής αλλά και του δημιουργούμενου flap, αξιοποιούνται δύο ακόμη παράμετροι, οι οποίες ταυτίζονται με τις x συντεταγμένες των σημείων όπου χωρίζεται η αεροτομή σε κύριο σώμα και flap. Με τις δύο επιπρόσθετες παραμέτρους η ΒΜ μπορεί να μεταβάλει μεταξύ άλλων το μήκος χορδής του flap και το κενό στην περιοχή του slot, επηρεάζοντας σημαντικά τους αεροδυναμικούς δείκτες απόδοσης.

Κεφάλαιο 3

Εξελικτικοί Αλγόριθμοι και Αιτιοκρατική Βελτιστοποίηση

3.1 Εξελικτικοί Αλγόριθμοι

Οι εξελικτικοί αλγόριθμοι (ΕΑ) αποτελούν μια κατηγορία στοχαστικών μεθόδων βελτιστοποίησης, εμπνευσμένων από τις αρχές της φυσικής επιλογής και της γενετικής. Η πληθυσμιακή τους δομή τούς επιτρέπει να εξερευνούν αποδοτικά πολύπλοκους και υψηλής διάστασης χώρους σχεδιασμού, καθιστώντας τους ιδιαίτερα κατάλληλους για προβλήματα που είναι μη γραμμικά, πολυτροπικά ή δεν διαθέτουν πληροφορία για παραγώγους. Δεδομένου ότι οι ΕΑ δεν βασίζονται σε παραγώγους, μπορούν να χειριστούν μη συνεχείς ή θορυβώδεις συναρτήσεις στόχου. Οι μηχανισμοί της επιλογής, της μετάλλαξης και της διασταύρωσης προσομοιώνουν τις φυσικές εξελικτικές διεργασίες, προάγοντας τόσο την εξερεύνηση όσο και την εκμετάλλευση του χώρου σχεδιασμού [13, 1].

Για την αντιμετώπιση του υψηλού υπολογιστικού κόστους των προσομοιώσεων ΥΡΔ κατά την αεροδυναμική ΒΜ, οι σύγχρονες μελέτες έχουν επικεντρωθεί στους εξελικτικούς αλγόριθμους υποβοηθούμενους από μεταμοντέλα (ΜΑΕΑ). Αυτοί ενσωματώνουν προσεγγιστικά μοντέλα αξιολόγησης (surrogates), δηλαδή αριθμητικές προσεγγίσεις εκπαιδευμένες σε περιορισμένο αριθμό προσομοιώσεων υψηλής ακρίβειας, για την εκτίμηση των συναρτήσεων στόχου. Με τη χρήση αυτών των μοντέλων για την καθοδήγηση της αναζήτησης, οι ΜΑΕΑ μπορούν να μειώσουν σημαντικά τον αριθμό των δαπανηρών αξιολογήσεων ΥΡΔ που απαιτούνται. Κοινές τεχνικές περιλαμβάνουν το kriging, τις συναρτήσεις βάσης ακτίνας (radial basis functions) και την πολυωνυμική παλινδρόμηση (polynomial regression), καθεμία εκ των οποίων προσφέρει έναν συμβι-

βασμό μεταξύ ακρίβειας και υπολογιστικής απόδοσης. Η διαδικασία βελτιστοποίησης εναλλάσσεται μεταξύ της εξερεύνησης του χώρου σχεδιασμού με χρήση του προσεγγιστικού μοντέλου και της βελτίωσης του μοντέλου με νέα δεδομένα από προσομοιώσεις ΥΡΔ. Αυτή η ισορροπία επιτρέπει στους MAEA να διατηρούν τις ικανότητες εξερεύνησης των εξελικτικών αλγορίθμων, βελτιώνοντας παράλληλα την απόδοση, κάτι ιδιαίτερα χρήσιμο σε αεροδυναμικές εφαρμογές [12].

3.2 Συζυγής Μέθοδος Βελτιστοποίησης

Η συζυγής μέθοδος αποτελεί ένα ισχυρό και αποδοτικό εργαλείο για τον σχεδιασμό στον τομέα της υπολογιστικής ρευστοδυναμικής. Το σημαντικότερο πλεονέκτημα της βελτιστοποίησης με βάση τη συζυγή μέθοδο είναι η δυνατότητα υπολογισμού των παραγώγων της συνάρτησης στόχου ως προς μεγάλο αριθμό μεταβλητών σχεδιασμού, με υπολογιστικό κόστος που είναι ανεξάρτητο από τον αριθμό αυτών των μεταβλητών. Η επίλυση του συζυγούς προβλήματος παράγει την απαραίτητη πληροφορία ευαισθησίας της συνάρτησης στόχου για την αιτιοκρατική βελτιστοποίηση. Αντίθετα με τις μεθόδους πεπερασμένων διαφορών, οι οποίες απαιτούν ξεχωριστές αξιολογήσεις για κάθε μεταβλητή σχεδιασμού, η συζυγής βελτιστοποίηση είναι ιδιαίτερα ελκυστική για προβλήματα υψηλής διάστασης, καθώς απαιτεί μόνο έναν επιπλέον υπολογισμό (ΥΡΔ) ανά συνάρτηση στόχου ή περιορισμό (ανά κύκλο βελτιστοποίησης).

Η συζυγής μέθοδος αναπτύσσεται, γενικά, σε δύο βασικά στάδια: πρώτον, την επίλυση του πρωτεύοντος προβλήματος που περιγράφει τη φυσική συμπεριφορά του συστήματος, όπως οι εξισώσεις Navier–Stokes στη ρευστοδυναμική, και δεύτερον, την επίλυση των αντίστοιχων συζυγών εξισώσεων που προκύπτουν από τη Λαγκρανζιανή του προβλήματος βελτιστοποίησης. Οι συζυγείς εξισώσεις επιλύονται για τον υπολογισμό των παραγώγων της συνάρτησης στόχου ως προς τις παραμέτρους σχεδιασμού. Απαραίτητη για αλγορίθμους βελτιστοποίησης όπως η gradient descent ή οι μέθοδοι τύπου quasi-Newton που εφαρμόζονται σε επαναληπτικές διαδικασίες σχεδιασμού, αυτή η τεχνική διπλής επίλυσης επιτρέπει εξαιρετικά αποδοτικό υπολογισμό παραγώγων [4, 3].

Σε κάθε κύκλο βελτιστοποίησης υπολογίζεται από τον οικείο επιλύτη PUMA η παράγωγος της αντικειμενικής συνάρτησης ως προς τις κομβικές συντεταγμένες της αεροτομής. Ωστόσο, για να ανανεωθούν οι μεταβλητές σχεδιασμού πρέπει οι παράγωγοι ευαισθησίας να εκφραστούν ως προς αυτές τις μεταβλητές. Όπως αναφέρεται παραπάνω, η αεροτομή μελετάται σε μία τυπική διαμόρφωση και στη διαμόρφωση με εκτεταμένο το flap. Έαν F συμβολίζει την αντικειμενική συνάρτηση, $\vec{b}_{par}$ το διάνυσμα των μεταβλητών σχεδιασμού PARSEC, $\vec{b}_{flap}$ το διάνυσμα των μεταβλητών σχεδιασμού του flap, X τις συντεταγμένες της αεροτομής, X' τις συντεταγμένες του κυρίου σώματος και του flap, και X'' τις συντεταγμένες του κυρίου σώματος και του εκτεταμένου flap, τότε οι παράγωγοι της αντικειμενικής συνάρτησης ως προς τις συντεταγμένες της αεροτομής μετατρέπονται σε παραγώγους ως προς τις μεταβλητές σχεδιασμού σε κάθε

διαμόρφωση με χρήση του κανόνα της αλυσίδας ως εξής

$$\frac{dF_{CR}}{d\vec{b}_{par}} = \frac{\partial F_{CR}}{\partial X}\frac{dX}{d\vec{b}_{par}} \tag{3.1}$$

$$\frac{dF_{TO}}{d\vec{b}_{par}} = \frac{\partial F_{TO}}{\partial X''}\frac{\partial X''}{\partial X'}\frac{\partial X'}{\partial X}\frac{dX}{d\vec{b}_{par}} \tag{3.2}$$

$$\frac{dF_{TO}}{d\vec{b}_{flap}} = \frac{\partial F_{TO}}{\partial X''}\frac{\partial X''}{\partial X'}\frac{dX'}{d\vec{b}_{flap}} \tag{3.3}$$

$$\frac{dF_{TO}}{d\vec{b}} = \left\{ \begin{array}{c} \dfrac{dF_{TO}}{d\vec{b}_{par}} \\ \dfrac{dF_{TO}}{d\vec{b}_{flap}} \end{array} \right\} \tag{3.4}$$

Η εξίσωση 3.1 αναφέρεται στην διαμόρφωση της αεροτομής με μη εκτεταμένο flap, η οποία μελετάται σε συνθήκες οριζόντιας πτήσης, εξ ου και ο δείκτης CR (cruise), ενώ οι εξισώσεις 3.2, 3.3 και 3.4 αφορούν τη διαμόρφωση με το εκτεταμένο flap που εξετάζεται σε συνθήκες απογείωσης (takeoff). Οι παράγωγοι $\partial F_{CR}/\partial X$ και $\partial F_{TO}/\partial X''$ υπολογίζονται από τον επιλύτη, ενώ όλες οι υπόλοιπες παράγωγοι που εμφανίζονται στις παραπάνω σχέσεις υπολογίζονται με παραγώγιση της διαδικασίας δημιουργίας της γεωμετρίας. Αφού υπολογιστούν οι παράγωγοι ευαισθησίας, εφαρμόζεται η μέθοδος απότομης καθόδου (steepest descent) για να ανανεωθούν οι τιμές των μεταβλητών σχεδιασμού ως εξής

$$\vec{b}^{k+1} = \vec{b}^{k} - \eta \frac{dF}{d\vec{b}}\bigg|_{k} \tag{3.5}$$

Κεφάλαιο 4

Δοκιμαστικές Μελέτες Βελτιστοποίησης

4.1 Εφαρμογές MAEA

Για τις δοκιμαστικές μελέτες ΒΜ της αεροτομής δύο στοιχείων με εφαρμογή MAEA χρησιμοποιήθηκε το λογισμικό EASY της ΜΠΥΡ&Β/ΕΜΠ [6, 5, 7]. Η αεροδυναμική απόδοση της αεροτομής εξετάζεται στα τρία σημεία λειτουργίας του πίνακα 4.1. Τα τρία αυτά σημεία λειτουργίας αξιολογούνται είτε ξεχωριστά σε μελέτες ενός στόχου (SOO) είτε σε συνδυασμό σε μελέτες δύο στόχων (MOO).

Σημείο Λειτουργίας	**Διαμόρφωση**	**Συνθήκες Πτήσης**
$CR1$ (οριζόντια πτήση)	Flap μη εκτεταμένο	5,000 m, 2^o AoA, 0.8 Mach
$CR2$ (οριζόντια πτήση)	Flap μη εκτεταμένο	10,000 m, 2^o AoA, 0.8 Mach
$TO1$ (απογείωση)	Flap εκτεταμένο	επίπεδο θάλασσας, 8^o AoA, 0.2 Mach

Πίνακας 4.1: *Σημεία λειτουργίας βελτιστοποίησης MAEA.*

Από τις 11 παραμέτρους PARSEC οι 9 λειτουργούν ως μεταβλητές σχεδιασμού για τη βελτιστοποίηση, καθώς η y συντεταγμένη και το κενό κατά y της ακμής εκφυγής έχουν σταθερή τιμή. Οι βασικές τιμές και τα όρια των μεταβλητών για τη βελτιστοποίηση, που υπολογίζονται με σκοπό να αποφευχθεί η δημιουργία μη ρεαλιστικών αεροτομών, αναγράφονται στον πίνακα 4.2. Κάποιες από τις μελέτες συμπεριλαμβάνουν και τις παραμέτρους του flap ως μεταβλητές σχεδιασμού. Τα όρια των δύο αυτών μεταβλητών υπολογίζονται ώστε το μήκος χορδής του flap να μην ξεπερνά το 35% του μήκους χορδής της αεροτομής, διότι συνήθως αυτή είναι η μέγιστη τιμή που εφαρμόζεται. Επιπρόσθετα, στις μελέτες που εξετάζονται επιβάλλονται κάποιοι ή όλοι από τους εξής

περιορισμούς: η επιφάνεια της αεροτομής πρέπει να είναι μεταξύ του 99% και του 101% της βασικής τιμής, ο συντελεστής άνωσης κατά την οριζόντια πτήση πρέπει να είναι μεγαλύτερος ή ίσος της βασικής τιμής και ο συντελεστής ροπής κατά την οριζόντια πτήση μεγαλύτερος ή ίσος του μηδενός και μικρότερος ή ίσος της βασικής τιμής. Οι λεπτομέρειες των μελετών βελτιστοποίησης με χρήση MAEA αναγράφονται στον πίνακα 4.3, όπου το γράμμα Ε συμβολίζει τη μέθοδο MAEA, ελ. την ελαχιστοποίηση του αναγραφόμενου μεγέθους και μεγ. τη μεγιστοποίηση. Τα αποτελέσματα για καθεμία από τις μελέτες παρουσιάζονται συνοπτικά στον πίνακα 4.4.

Μεταβλητή	**Βασική τιμή**	**Κάτω όριο**	**Άνω όριο**
r_{LE}	0.01	0.075	0.0125
α_{TE}	-0.209439	-0.226	-0.186
β_{TE}	0.04363	0.03	0.06
x_{SS}	0.427949886	0.33	0.52
y_{SS}	0.065114543	0.05	0.08
$y_{xx,SS}$	-0.34989106	-0.5	-0.3
x_{PS}	0.480017747	0.4	0.58
y_{PS}	-0.060535044	-0.072	-0.048
$y_{xx,PS}$	0.597819177	0.5	0.7
$x_{suction,cut}$	0.95	0.925	0.99
D	0.225	0.1	0.25

Πίνακας 4.2: *Βασικές τιμές και κατώτατα και ανώτερα όρια των μεταβλητών σχεδιασμού για τις μελέτες βελτιστοποίησης με MAEA.*

Μελέτη	**Στόχοι**	**Περιορισμοί**	**Μεταβλητές Σχεδιασμού**
E1	ελ. C_D at CR1	Επιφάνεια & C_L	PARSEC
E2α	ελ. C_D at CR1 & μεγ. C_L at TO1	Επιφάνεια	PARSEC
E2β	ελ. C_D at CR1 & μεγ. C_L at TO1	Επιφάνεια, C_L & C_M	PARSEC
E3	ελ. C_D at CR2 & μεγ. C_L at TO1	Επιφάνεια, C_L & C_M	PARSEC
E4	μεγ. C_L at TO1	-	Flap
E5	ελ. C_D at CR1 & μεγ. C_L at TO1	Επιφάνεια, C_L & C_M	PARSEC & Flap

Πίνακας 4.3: *Μελέτες βελτιστοποίησης με MAEA.*

Μελέτη	**Αποτελέσματα**
E1	$C_{D,CR}$ -34%, $C_{L,CR}$ +1.8%
E2α	8 λύσεις, ελάχιστο $C_{D,CR}$ -35%, μέγιστο $C_{L,TO}$ +4.2%
E2β	5 λύσεις, ελάχιστο $C_{D,CR}$ -24%, μέγιστο $C_{L,TO}$ +2.1%
E3	11 λύσεις, ελάχιστο $C_{D,CR}$ -17.6%, μέγιστο $C_{L,TO}$ +5.5%
E4	$C_{D,TO}$ +11.6%, $C_{L,TO}$ +4.9%
E5	8 λύσεις, ελάχιστο $C_{D,CR}$ -33%, μέγιστο $C_{L,TO}$ -1%

Πίνακας 4.4: *Αποτελέσματα μελετών βελτιστοποίησης με MAEA.*

4.2 Εφαρμογές Συζυγούς Μεθόδου

Τα σημεία λειτουργίας της αεροτομής δύο στοιχείων που διερευνήθηκαν με τη συζυγή μέθοδο μέσω του PUMA παρουσιάζονται στον πίνακα 4.5. Ως μεταβλητές σχεδιασμού αξιοποιούνται οι ίδιες με αυτές των μελετών με MAEA, οι βασικές τιμές των οποίων αναγράφονται στον πίνακα 4.2. Περιορισμοί δεν επιβάλλονται άμεσα στις εφαρμογές της συζυγούς μεθόδου. Ωστόσο, με σκοπό να διατηρείται η επιφάνεια της αεροτομής περίπου ίδια σε κάθε νέα λύση, περιορίζεται η τιμή της μεταβλητής σχεδιασμού r_{LE} και η διαφορά των μεταβλητών y_{SS} και y_{PS} κρατιέται σταθερή. Επίσης, εφαρμόζονται τα όρια που προαναφέρθηκαν για τις παραμέτρους του flap. Οι λεπτομέρειες και τα αποτελέσματα των μελετών που πραγματοποιήθηκαν με τη συζυγή μέθοδο παρουσιάζονται στους πίνακες 4.6 και 4.7, αντίστοιχα. Το γράμμα Α στον πίνακα 4.6 συμβολίζει τη συζυγή (adjoint) μέθοδο.

Σημείο Λειτουργίας	**Διαμόρφωση**	**Συνθήκες Πτήσης**
$CR1$ (οριζόντια πτήση)	Flap μη εκτεταμένο	10,000 m, 2^o AoA, 0.8 Mach
$TO1$ (απογείωση)	Flap εκτεταμένο	επίπεδο θάλασσας, 8^o AoA, 0.2 Mach

Πίνακας 4.5: *Σημεία λειτουργίας βελτιστοποίησης με τη συζυγή μέθοδο.*

Μελέτη	**Στόχοι**	**Περιορισμοί**	**Μεταβλητές Σχεδιασμού**
A1	ελ. C_D at CR1	-	PARSEC
A2	μεγ. C_L at TO1	-	Flap
A3	μεγ. C_L at TO1	-	PARSEC & Flap
A4	ελ. C_D at CR1 & μεγ. C_L at TO1	-	PARSEC & Flap

Πίνακας 4.6: *Μελέτες βελτιστοποίησης με τη συζυγή μέθοδο.*

Μελέτη	**Αποτελέσματα**
A1	$C_{D,CR}$ -42%, $C_{L,CR}$ -6.2%
A2	$C_{D,TO}$ +6%, $C_{L,TO}$ +2.4%
A3	$C_{D,TO}$ +2.4%, $C_{L,TO}$ +19%
A4	6 λύσεις, ελάχιστο $C_{D,CR}$ -42%, μέγιστο $C_{L,TO}$ +13%

Πίνακας 4.7: *Αποτελέσματα μελετών βελτιστοποίησης με τη συζυγή μέθοδο.*

Βιβλιογραφία

[1] Bäck, T., Fogel, D.B., Michalewicz, Z.: Handbook of Evolutionary Computation (1st ed.). CRC Press (1997). https://doi.org/10.1201/9780367802486

[2] Federal Aviation Administration: Pilot's Handbook of Aeronautical Knowledge. U.S. Department of Transportation (2023), https://www.faa.gov/regulations_policies/handbooks_manuals/aviation/phak, fAA-H-8083-25C

[3] Giles, M.B., Pierce, N.A.: An introduction to the adjoint approach to design. Flow, Turbulence and Combustion **65**, 393–415 (2000). https://doi.org/10.1023/A:1011430410075

[4] Jameson, A.: Aerodynamic Design via Control Theory, Lecture Notes in Computer Science, vol. 145. Springer (1988)

[5] Kampolis, I.C., Giannakoglou, K.C.: Distributed Evolutionary Algorithms with Hierarchical Evaluation. Engineering Optimization **41**(11), 1037–1049 (2009)

[6] Kapsoulis, D.H., Tsiakas, K.T., Trompoukis, X.S., Asouti, V.G., Giannakoglou, K.C.: Evolutionary multi-objective optimization assisted by metamodels, kernel PCA and multi-criteria decision making techniques with applications in aerodynamics. Applied Soft Computing **64**, 1–13 (2018)

[7] Karakasis, M., Giannakoglou, K.C.: On the Use of Metamodel-Assisted Multi-Objective Evolutionary Algorithms. Engineering Optimization **38**(8), 941–957 (2006)

[8] Martins, J.R.: Aerodynamic design optimization: Challenges and perspectives. Computers & Fluids **239**, 105391 (2022). https://doi.org/https://doi.org/10.1016/j.compfluid.2022.105391, https://www.sciencedirect.com/science/article/pii/S0045793022000615

[9] Salunke, N.P., Ahamad, R.J., Channiwala, S.: Airfoil parameterization techniques: A review. American Journal of Mechanical Engineering **2**(4), 99–102 (2014)

[10] Skinner, S., Zare-Behtash, H.: State-of-the-art in aerodynamic shape optimisation methods. Applied Soft Computing **62**, 933–962 (2018). https://doi.org/https://doi.org/10.1016/j.asoc.2017.09.030, https://www.sciencedirect.com/science/article/pii/S1568494617305690

[11] Sobieczky, H.: Parametric airfoils and wings. Notes on Numerical Fluid Mechanics **68**, 71–88 (1998)

[12] Zhou, Z.H., Zhang, J.Q., Jin, Y.: Combining global and local surrogate models to accelerate evolutionary optimization. IEEE Transactions on Systems, Man, and Cybernetics, Part C (Applications and Reviews) **41**(6), 982–994 (2011)

[13] Κ.Χ. Γιαννάκογλου: Μέθοδοι Βελτιστοποίησης στην Αεροδυναμική. ΕΜΠ Σχολή Μηχανολόγων Μηχανικών (2004)